MAGNETICALLY ACTUATED PEEL TEST FOR THIN FILM INTERFACIAL FRACTURE AND FATIGUE CHARACTERIZATION

A PhD Dissertation
Presented to
The Academic Faculty

by

Gregory T. Ostrowicki

In Partial Fulfillment
of the Requirements for the Degree
Doctor of Philosophy in the
George W. Woodruff School of Mechanical Engineering

Georgia Institute of Technology
October 2012

MAGNETICALLY ACTUATED PEEL TEST FOR THIN FILM INTERFACIAL FRACTURE AND FATIGUE CHARACTERIZATION

Approved by:

Dr. Suresh K. Sitaraman, Advisor
School of Mechanical Engineering
Georgia Institute of Technology

Dr. Paul A. Kohl
School of Chemical & Biomolecular Engineering
Georgia Institute of Technology

Dr. Richard W. Neu
School of Mechanical Engineering
Georgia Institute of Technology

Dr. Rao R. Tummala
School of Electrical & Computer Engineering
Georgia Institute of Technology

Dr. Peter J. Hesketh
School of Mechanical Engineering
Georgia Institute of Technology

Date Approved: October 24, 2012

To my parents

ACKNOWLEDGEMENTS

There are so many people to thank for having invested their time, energy, and love into supporting my graduate school journey. My time at Georgia Tech has been a period of tremendous growth, thanks to all my teachers, colleagues, and friends. Throughout all the challenges of pursuing a Ph.D., I am gratefully left with countless rewarding experiences.

I would like to express my sincerest gratitude to my advisor, Dr. Suresh Sitaraman. He has been a consummate teacher, mentor, and friend throughout my time at Georgia Tech. I will forever look to his example as a role model in both my professional and personal life.

I would like to thank Dr. Rick Neu and Michael Hirsch for use of their equipment in calibration measurements; Dr. Paul Kohl and Dr. Nathan Fritz for their invaluable help and assistance in polymer processing; Dr. Peter Hesketh for help and use of equipment in magnetic material processing; Dr. Tummala and the PRC staff for assistance and use of their equipment; Gary Spinner and the entire cleanroom staff for help with microfabrication; Nick Ginga, Xi Liu, and Raphael Okereke for countless discussions and assistance with processing; Kevin Klein, Dr. Jiantao Zheng, Jamie Ahmad, and Dr. Karan Kacker for taking me under their wings when I was a new graduate student.

I would like to thank my parents, who have been a guiding force throughout my life, and for whom I am so lucky to be their son. I would also like to thank my brother, sister, and my entire extended family for all their love and support.

Most of all, I would like to thank my dear Ashley. She is the reason behind my happiest times in Atlanta as well as my best research work at Georgia Tech. I remain in awe of her strength, beauty, and capacity for love.

I would like to acknowledge the National Science Foundation for supporting this work under Grant No. CMMI-0800037.

TABLE OF CONTENTS

LIST OF TABLES

LIST OF FIGURES

SUMMARY

Delamination along thin film interfaces is a prevalent failure mechanism in microelectronic, photonic, MEMS, and other engineering applications. Current interfacial fracture test techniques specific to thin films are limited by either sophisticated mechanical fixturing, physical contact near the crack tip, non-representative test specimens, or complicated stress fields. Moreover, these techniques are generally not suitable for investigating fatigue crack propagation under cyclical loading.

A fixtureless and noncontact experimental test technique is thus proposed and implemented to study interfacial fracture for thin film systems. The proposed test incorporates permanent magnets surface mounted onto micro-fabricated released thin film structures. An applied external magnetic field induces noncontact monotonic or fatigue loading to initiate delamination along the interface between the thin film and underlying substrate. Characterization of the film deflection, peel angle, and delamination propagation is accomplished through *in situ* optical techniques. Analytical and finite-element models are used to extract fracture parameters from the experimental data using thin-film peel mechanics. The developed interfacial fracture test has been demonstrated for Cu thin films on a SiO_2/Si substrate.

CHAPTER 1

INTRODUCTION

The invention of the integrated circuit (IC) by Jack Kilby in 1958 ushered in an era of technological revolution that continues to propel the fields of science and engineering today. For the first time, all the essential components of an electronic circuit had been integrated onto a single semiconductor, and formed the basis on which all modern electronic devices operate. Improvements of the IC over time, for which the number of transistors on a single chip has increased from just a handful to over a billion, is attributable to advances in the science of miniaturization. Computing machines that once occupied an entire room can now rest on a fingertip, and contain orders of magnitude more processing power and capabilities.

The drive for the development of micromachining technologies was thus born from the electronics industry in pursuit of smaller, faster, more integrated, and energy efficient microprocessors. Lithographic processes can transfer patterns with features as small as a few microns using a masking process to a few nanometers using a focused electron-beam. A vast variety of film materials can be deposited with nearly atomic precision using physical vapor deposition (PVD) such as evaporation and sputtering as well as chemical vapor deposition (CVD). Further developments in subtractive wet and dry etching, micromolds, and microassembly techniques add to the versatility of possible microfabrication processes.

These fabrication technologies proved to have great potential beyond the standard IC application and have been adapted to create micro/nano-scale sensors, actuators, and transducers (see Figure 1.1). Such devices are generally classified as microelectromechanical systems (MEMS) or nanoelectromechanical systems (NEMS) depending on their scale. For example, current MEMS sensing devices include:

accelerometers, gyros, pressure and air flow sensors, chemical sensors, and spectrometers. MEMS actuators have been developed for microfluidics applications such as pumps, valves, and nozzles. Other actuators power micromirror arrays used for digital displays, or are part of larger micromotor designs.

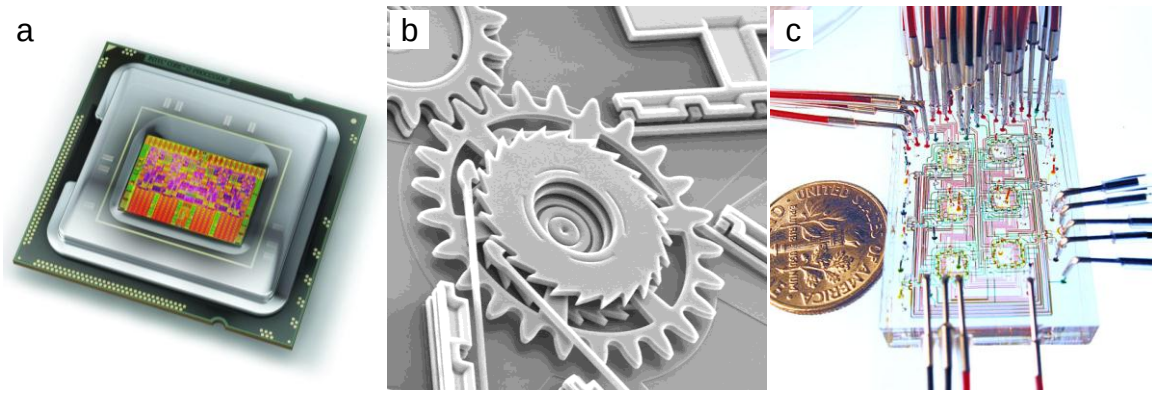

Figure 1.1. (a) Illustration of Intel Core i7 microprocessor. (b) Micromachined gears and ratcheting mechanism [*Sandia National Laboratories*]. (c) Microfluidic lab-on-a-chip [*Stanford University*].

The interest in medical applications for MEMS has also grown significantly in recent years, with much promise for improved diagnosis and the treatment of illness. For example, biological sensors capable of detecting cancer markers at unprecedentedly minute levels have been developed utilizing nanoscale structures. These types of sensors are now being integrated with other MEMS and IC technologies to realize the lab-on-a-chip (LOC) concept, where a single device can perform the processing, sensing, and analysis of serum and other chemicals more rapidly and accurately than through conventional means.

The success of these amazing MEMS and IC devices depend on a critical part of the design and manufacturing process known as "packaging". The active components are fragile and isolated, and therefore must be both protected from the environment as well as connected to the rest of the system. In effect, the package bridges the gap between the micro/nano interactions at the core of the device and the tools of the macroscale world. The multifaceted functions of the package present many technological challenges which

often require unique materials and processes, and can add to the overall complexity of the device.

Fabrication of these advanced micro/nano-devices is predominantly a serial process; layers upon layers of thin films are deposited and patterned as needed. These thin film stacks can have nanoscale dimensions and often couple together drastically dissimilar materials. For example, high end microprocessors can have over twenty layers of copper nanowire connections on the surface of a silicon die, where the layers are separated by a combination of barrier metals, passivation films, and brittle dielectric ceramics. Furthermore, these chips are then assembled to a substrate which itself is a laminate of metal, glass, and organic polymers. The material properties and deposition conditions of each of these films vary greatly, and as a result they respond differently to temperature and mechanical stresses.

The interface between materials is often mechanically weaker than the bulk. Thus, multilayered thin film systems are often prone to interfacial delamination under various loading conditions resulting in premature failure of the devices. For example, sudden catastrophic delamination failures can occur due to overstresses caused by an unforgiving fabrication process or an overload in the field. Alternatively, interfacial cracks can nucleate and grow incrementally over many loading cycles until device failure. Thus, interfacial delamination is an important reliability concern for a wide range of applications as shown in Figure 1.2.

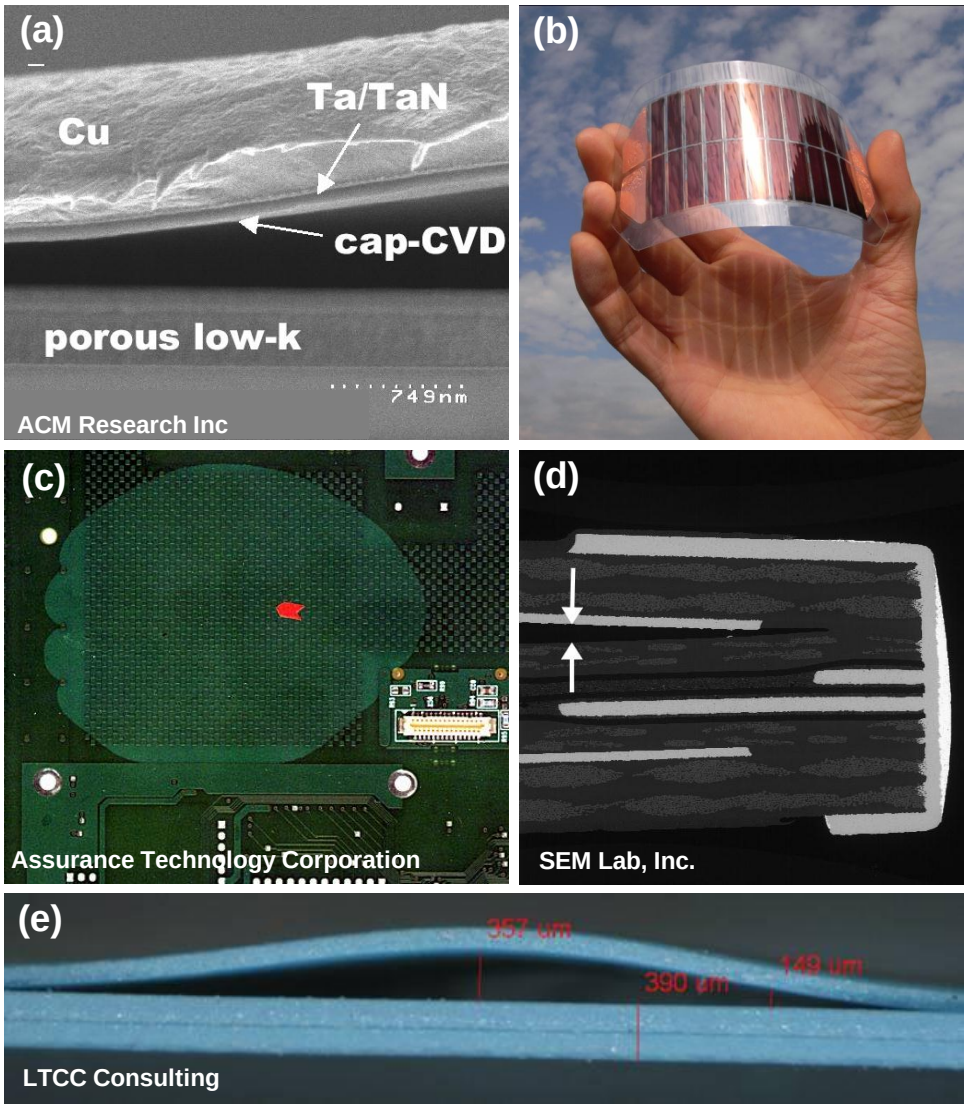

Figure 1.2. Example applications which commonly suffer from delamination failure: (a) active silicon die interface between nanoscale metal/ceramic films, (b) flexible solar cell, (c, d) organic printed circuit board, (e) glass-ceramic substrate laminate.

Prediction (and ultimately, prevention) of delamination failure requires a comprehensive understanding of the interfacial mechanics governing crack propagation. Many theoretical and numerical studies detailing approaches for characterizing interfacial fracture have been advanced in the literature. These approaches must be validated through experimental methods, where delamination can be initiated and studied under controlled conditions. Numerous experimental test techniques have been proposed, but the delamination testing of thin film systems remains a challenge. Consequently, there is

a gap in experimental data for interfacial fracture between thin films. This gap is even greater for interfacial fatigue, where there are few published results of thin film delamination propagation. New experimental test techniques are therefore needed to be able to generate interfacial fracture data for a diverse set of thin film systems subjected to various applied loads and various environmental conditions.

CHAPTER 2

LITERATURE REVIEW

2.1 Fracture Mechanics Approaches

The basic principles of interfacial fracture mechanics are shared with traditional cohesive fracture mechanics. The objective in both cases is to find characteristic parameters that define the material's or interface's resistance to fracture, regardless of the applied loading conditions at the crack tip. The following approaches have thus been developed to characterize fracture under monotonic loading.

2.1.1 Thermodynamic Approach

The most broadly applicable method of characterizing resistance to fracture is through performing an energy balance, a concept first proposed by Griffith in 1920 [1]. Under quasistatic equilibrium, the amount of energy supplied to a system undergoing fracture must be balanced by the energy stored due to elastic deformation, and the energy dissipated due to the creation of new crack surfaces, plastic deformation, and other losses. For steady state delamination this is expressed in differential form by

$$dW = dU_e + dU_p + dU_f + dU_d, \tag{2.1}$$

where W is the external work, U_e is the elastic strain energy, U_p is the plastic work, U_f is the energy of fracture, and U_d is the sum of other losses due to the generation of heat, sound, etc. The energy of fracture, which includes the energy expended to break the interfacial bonds and the resulting surface energy of the newly cracked surfaces, can be expressed as

$$U_f = \Gamma A, \tag{2.2}$$

where Γ is the fracture energy rate (FER), or adhesion energy per unit area, and A is the area of the crack. When the crack propagates through a homogeneous material or

through a consistent interface, one can assume that the FER is constant throughout the crack growth process. Thus, by considering only the external work, elastic strain energy, and plastic work, Γ can be solved for using

$$\Gamma = \frac{d}{dA}[W - U_e - U_p]. \tag{2.3}$$

When determining whether or not a crack will propagate, one can consider Γ to be the available energy for fracture. Therefore, $\Gamma \geq \Gamma_0$ must be satisfied in order for fracture to occur, where Γ_0 is the critical FER that is characteristic of the cracked body or interface.

The calculation for Γ can be separated into two components: (1) potential energy from external work and elastic strain energy, and (2) plastic dissipation. The potential energy contribution to Γ is referred to as the energy release rate (ERR) [2] and is expressed as

$$G = \frac{d}{dA}[W - U_e]. \tag{2.4}$$

When the plastic zone at the crack tip is negligible, $G = \Gamma$. However, when there is significant plastic dissipation, as is often the case with ductile materials, $G > \Gamma$. From an analytical and numerical modeling perspective, the external work and elastic strain energy are generally straightforward to calculate. The plastic dissipation, on the other hand, can be very challenging to accurately calculate when dealing with ductile materials.

The loading conditions at the crack tip are either opening (mode I), in-plane shear (mode II), out-of-plane shear (mode III), or some combination thereof [3]. An interface's resistance to delamination is usually different for each fracture mode, and thus Γ_0 must be a function of the mode mix. The interface can therefore be fully characterized by at least two parameters – interfacial fracture toughness and mode mix. The mode mix, however, can also be challenging to calculate, and is not well defined for interfacial cracks in ductile systems.

2.1.2 Linear Elastic Approach

For the case with small scale yielding at the crack tip, such as brittle fracture, linear elastic fracture mechanics (LEFM) provides an alternative stress-based approach to fracture characterization. The solution schemes of linear elasticity are used to solve for the stress fields for a cracked body under load. The resulting magnitude of the stress fields at the crack tip are then used to determine a characteristic fracture toughness of the material. A stress intensity factor K is thus defined as

$$K = \sigma\left(\sqrt{a}\right)Y(a/b) \tag{2.5}$$

where σ is the remotely applied stress, a is the characteristic crack dimension, and Y is a geometric factor based on the ratio of the crack length a to the width b [4]. The onset of fracture occurs when the applied K exceeds the critical stress intensity factor K_c. A material is most restricted in deformation and is thus most susceptible to unstable fracture when in the plane-strain state. Therefore, the characteristic fracture toughness is generally reported under plane-strain conditions.

The stress field around the crack can be determined from a solution to the biharmonic equation with the appropriate boundary conditions. For two-dimensional geometry as shown in Figure 2.1, the Airy stress function can be determined for homogenous, isotropic, linear elastic solids such that

$$\sigma_{ij} = \frac{K}{\sqrt{2\pi r}} f_{ij}(\theta) \tag{2.6}$$

where σ_{ij} is the stress component, r and θ are the polar coordinates, and $f_{ij}(\theta)$ is a function dependent on the corresponding stress component considered [3]. It is clear that Equation 2.6 produces a stress singularity at the crack tip, and thus K can be interpreted as the magnitude of the singularity field.

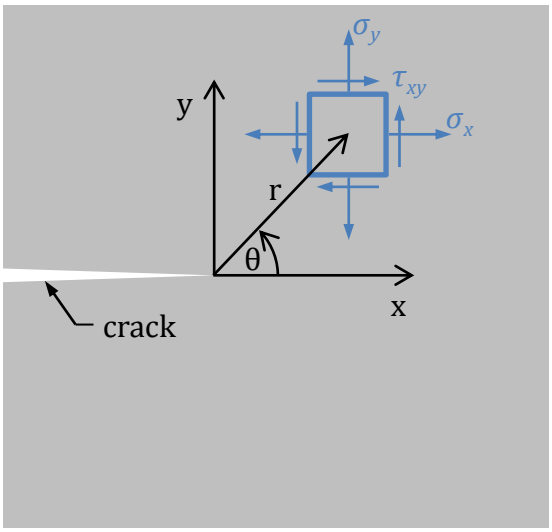

Figure 2.1. Stress element near crack tip in homogenous solid.

There are separate solutions to Equation 2.6 for remote loading on an infinite solid depending on the opening mode of the crack. For strict mode I loading, the resulting stress field is described as

$$\sigma_x = \frac{K_I}{\sqrt{2\pi r}}\cos\frac{\theta}{2}\left(1 - \sin\frac{\theta}{2}\sin\frac{3\theta}{2}\right) \tag{2.7}$$

$$\sigma_y = \frac{K_I}{\sqrt{2\pi r}}\cos\frac{\theta}{2}\left(1 + \sin\frac{\theta}{2}\sin\frac{3\theta}{2}\right) \tag{2.8}$$

$$\tau_{xy} = \frac{K_I}{\sqrt{2\pi r}}\cos\frac{\theta}{2}\sin\frac{\theta}{2}\cos\frac{3\theta}{2} \tag{2.9}$$

whereas for strict mode II loading the stress field is

$$\sigma_x = -\frac{K_{II}}{\sqrt{2\pi r}}\sin\frac{\theta}{2}\left(2 + \cos\frac{\theta}{2}\cos\frac{3\theta}{2}\right) \tag{2.10}$$

$$\sigma_y = \frac{K_{II}}{\sqrt{2\pi r}}\sin\frac{\theta}{2}\cos\frac{\theta}{2}\cos\frac{3\theta}{2} \tag{2.11}$$

$$\tau_{xy} = \frac{K_{II}}{\sqrt{2\pi r}}\cos\frac{\theta}{2}\left(1 - \sin\frac{\theta}{2}\sin\frac{3\theta}{2}\right) \tag{2.12}$$

where K_I and K_{II} are the stress intensity factors for mode I and mode II, respectively [3]. For mixed mode loading, the total stress distribution is a superposition of the two cases. Since the local stresses are dominated by the crack, knowledge of K and its mode I and mode II components is sufficient to characterize the stress distribution at the crack tip regardless of the global loading conditions. Equivalence between K and G [5] can also be established such that

$$G = \frac{K^2}{E'} \tag{2.13}$$

where the Young's modulus E' is defined for plane-stress and plane-strain conditions as

$$E' = \begin{cases} E & \text{(plane stress)} \\ \dfrac{E}{1-\nu^2} & \text{(plane strain)} \end{cases} \tag{2.14}$$

Interfacial Cracks

An interfacial crack presents some additional complications to the LEFM approach due to the discontinuity across the crack direction. A bimaterial crack with two dissimilar isotropic materials is shown in Figure 2.2, where E_i is the Young's modulus, μ_i is the shear modulus, and ν_i is the Poison's ratio of each material, respectively. The resulting stress field is dependent upon the elastic mismatch quantified by the non-dimensional Dundurs parameters α and β through

$$\alpha = \frac{\mu_1(\kappa_2+1) - \mu_2(\kappa_1+1)}{\mu_1(\kappa_2+1) + \mu_2(\kappa_1+1)} \tag{2.15}$$

$$\beta = \frac{\mu_1(\kappa_2-1) - \mu_2(\kappa_1-1)}{\mu_1(\kappa_2+1) + \mu_2(\kappa_1+1)} \tag{2.16}$$

where $\kappa_i = 3\text{-}4\nu_i$ for plane strain and $\kappa_i = (3\text{-}\nu_i)/(1+\nu_i)$ for plane stress [6]. Both α and β equal zero when there is no mismatch between the two materials (i.e. a homogeneous solid).

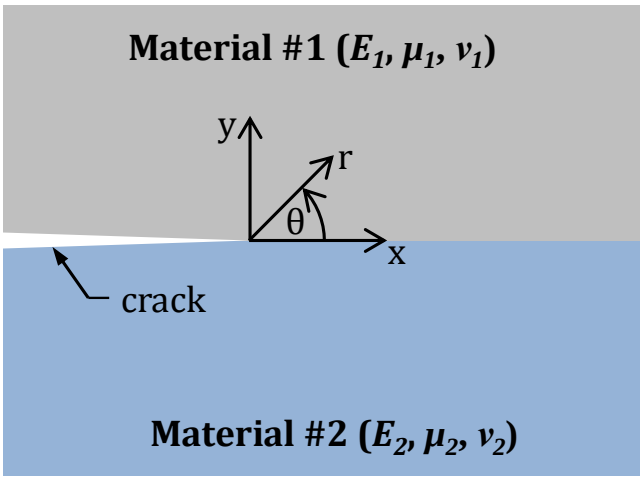

Figure 2.2. Bimaterial crack with mismatched elastic parameters.

A linear elastic solution for the stress distribution for interfacial fracture was first developed by Williams [7] using the Airy stress function approach. The result was a complex form of the stress with an inverse-square singularity at the crack tip as well as local oscillatory stress behavior. Others have obtained similar conclusions through other means [8-10]. However, a troubling consequence of the oscillatory stress solution is that it also results in interpenetration of the crack faces behind the crack tip. By considering a transition zone in lieu of a single crack tip transition point, Comninou [11-13] obtained a similar singularity but without the oscillating stress. However, the assumptions of the arbitrarily defined transition zone were found to significantly influence the resulting local stress field shape.

Building off the notion of the complex stress intensity factor, $K = K_1 + iK_2$ proposed by Erdogan [8, 14], Rice [15, 16] developed an expression for the stress distribution around an interfacial crack as

$$\sigma_{ij} = \frac{\mathrm{Re}\left[Kr^{i\epsilon}\right]}{\sqrt{2\pi r}}\sigma_{ij}^{I}(\theta,\epsilon) + \frac{\mathrm{Im}\left[Kr^{i\epsilon}\right]}{\sqrt{2\pi r}}\sigma_{ij}^{II}(\theta,\epsilon), \tag{2.17}$$

where σ^{I}_{ij} and σ^{II}_{ij} are functions of the polar angle and elastic mismatch, r and θ are the polar coordinates as in Figure 2.2, and

$$\epsilon = \frac{1}{2\pi} \ln\left(\frac{1-\beta}{1+\beta}\right). \tag{2.18}$$

The stress at the interface ahead of the crack tip ($\theta = 0$) is thus described as

$$\sigma_y + i\tau_{xy} = \frac{(K_1 + iK_2)r^{i\epsilon}}{\sqrt{2\pi r}} \tag{2.19}$$

where

$$r^{i\epsilon} = \cos(\epsilon \ln r) + i \sin(\epsilon \ln r) \tag{2.20}$$

A small contact zone resulting from this oscillatory solution was derived by Shih [17] from the displacements of the debonded surfaces behind the crack tip. The size of the contact zone was shown to be smaller than all relevant length scales, and thus confirmed that the solution was valid away from the immediate vicinity of the crack tip.

The ERR can also be calculated from the complex stress intensity factor [18] through

$$G = \frac{(1-\beta^2)}{E_*}(K_1^2 + K_2^2) \tag{2.21}$$

where

$$\frac{1}{E_*} = \frac{1}{2}\left(\frac{1}{E'_1} + \frac{1}{E'_2}\right) \tag{2.22}$$

Fracture at a bimaterial interface is inherently mixed mode, as the shear and tensile stresses are coupled such that both K_1 and K_2 are active at the crack tip even under a pure remote opening load [19]. The interfacial fracture toughness G_c, or the critical ERR at which a crack propagates, is therefore a function of the phase angle ψ. Since the mode mix has been shown to be insensitive to the Dundars parameter β [20], for convenience the phase angle can be evaluated for $\beta = 0$ through

$$\psi = \tan^{-1}\left(\frac{K_2}{K_1}\right) \tag{2.23}$$

Limitations

The conditions for which LEFM assumptions are appropriate are restricted to small scale yielding where the plastic zone size at the crack tip is much smaller than the dimensions of the cracked body. Ductile material systems, however, often form a large plastic zone during the fracture process which dissipates much of the applied energy, and therefore require other approaches to characterize the fracture parameters.

These large plastic effects can disrupt the stress distribution such that the stress intensity factor is no longer meaningful for characterizing the stress field. Consequently, the mode mix for ductile fracture is not well defined. Others have suggested alternative parameters in lieu of ψ to characterize the mode mix, such as the crack tip slope angle [21] and effective strain at the crack tip [22]. However, there remains no generally accepted characterization of the mode mix for large scale plastic fracture.

A branch of elastic-plastic fracture mechanics has been pursued to account for some of these large plastic effects. For example, the R-curve was introduced as a measure of the crack extension resistance through a plot of the energy dissipation relative to the crack size [23]. Also, the J-integral was developed as an alternative criterion for crack propagation, and involves performing an energetic contour path integral which circumscribes the plastic zone around the crack tip [24]. However, these methods still have difficulty applying to the case where the plastic zone reaches the boundary of the material, as is often the case with the peeling of thin ductile films. In addition, there is evidence that these methods are not independent of the specimen geometry [21, 25].

2.1.3 Cohesive Zone Approach

A different approach aims to capture the adhesive properties of an interface directly by attributing an energy potential to the interface that defines its traction-separation behavior. Based on work by Dugdale [26] and Barenblatt [27], the interface is modeled as a cohesive zone between the debonding surfaces, where the normal and tangential separation behavior can be individually defined by a unique potential as shown in Figure 2.3. These potentials can be modeled using either a multi-linear or exponential curve, and are typically defined by the maximum allowed stress $\hat{\sigma}$, the critical separation gap δ_c, and the interfacial adhesion energy Γ_0 which is equivalent to the area under the σ-δ curve. Once the potentials are appropriately defined, they can be incorporated into a model to not only predict whether or not delamination will occur, but also how and in which direction the crack will propagate.

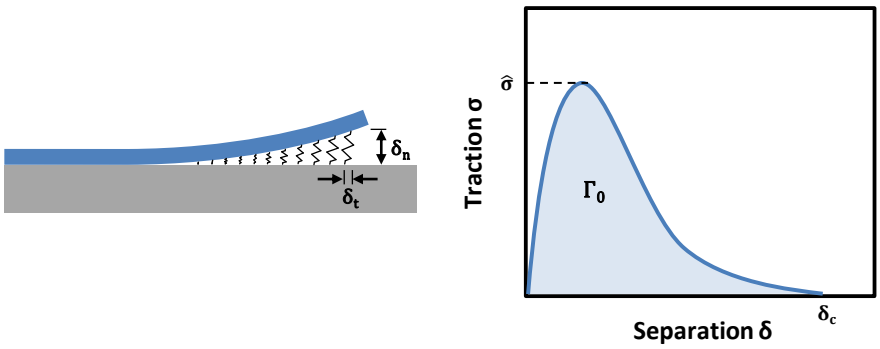

Figure 2.3. Cohesive zone model for interface of a bimaterial system.

The difficulty with using this approach is that determining the cohesive zone potentials for each of the fracture modes can be an onerous task. There are many assumptions regarding the shape of the energy potentials as well as their defining parameters. From a characterization standpoint, these potentials must be iteratively redefined until the simulated fracture occurs at the same critical load as observed in the matching experiment. Moreover, it is difficult to experimentally verify whether the derived potentials make physical sense.

2.2 Fatigue Crack Propagation

The fracture mechanics approaches discussed previously are able to characterize the interfacial fracture toughness and therefore predict the conditions under which a crack will grow when subjected to monotonic loading. However, when an interface is subjected to cyclic fatigue loading, a crack can grow under subcritical loads due to the damage accumulated over many cycles. In fact, fatigue cracks have been observed to propagate at loading amplitudes as little as 1/6 of the critical monotonic load for metal/ceramic interfaces [28].

The crack growth rate for metals under various constant amplitude loads can be categorized into three different regimes. Stage-I is the crack nucleation regime characterized by very slow growth about some threshold loading amplitude. Stage-II is an intermediate regime of stable crack growth, and finally Stage-III is characterized as rapid unstable fracture as the loading amplitude approaches the critical monotonic fracture strength. Paris [29] was the first to observe that the dominant Stage-II fatigue crack growth speed can be shown to be a predictable function of the applied stress intensity factor. As shown in Figure 2.4, a more general formula for the Paris law trend can be expressed as

$$\frac{da}{dN} = C(\Delta G)^m, \tag{2.5}$$

where a is the crack length, N is the number of loading cycles, ΔG is the ERR amplitude, and C and m are constants. Based on these experimentally derived parameters, one can then develop fatigue crack growth models with damage metrics that correlate with the Paris law fit.

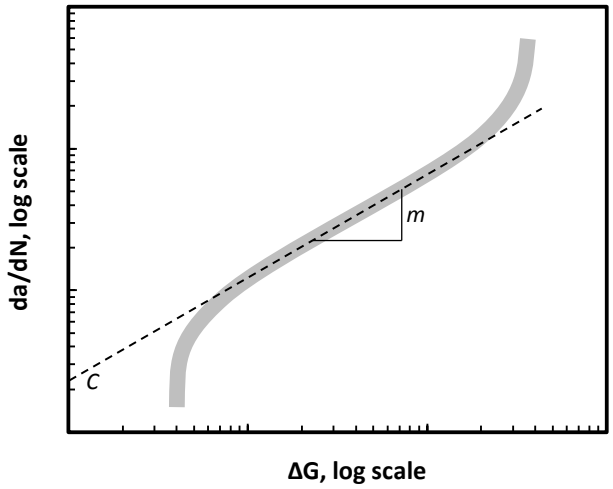

Figure 2.4. Typical crack growth rate trend with Paris law fit.

In general, the fatigue crack growth rate is a function of the stress amplitude at the crack tip, the crack length, and the stress ratio $R = \sigma_{min}/\sigma_{max}$. Some additional factors which can affect the fatigue behavior include the material microstructure, temperature and humidity conditions, and stress state, among others. However, due to the difficulty in testing and handling thin film specimens, there is a lack of experimental data in the literature for interfacial fatigue crack growth within thin film systems.

2.3 Experimental Characterization

Experimental test methods are needed to study the interfacial fracture process under controlled conditions, and therefore numerous test methods and specimen designs have been proposed in the literature. Since materials and the interfaces they share often have different mechanical properties at the micro/nano scale than in bulk, there has been a particular focus toward developing appropriate test methods to characterize interfacial fracture between thin films. Specimen fabrication, handling, experimental setup, and analysis are all challenges regarding experimental thin film delamination studies. Some common established delamination test techniques for thin films are shown in Figure 2.5 and are discussed below.

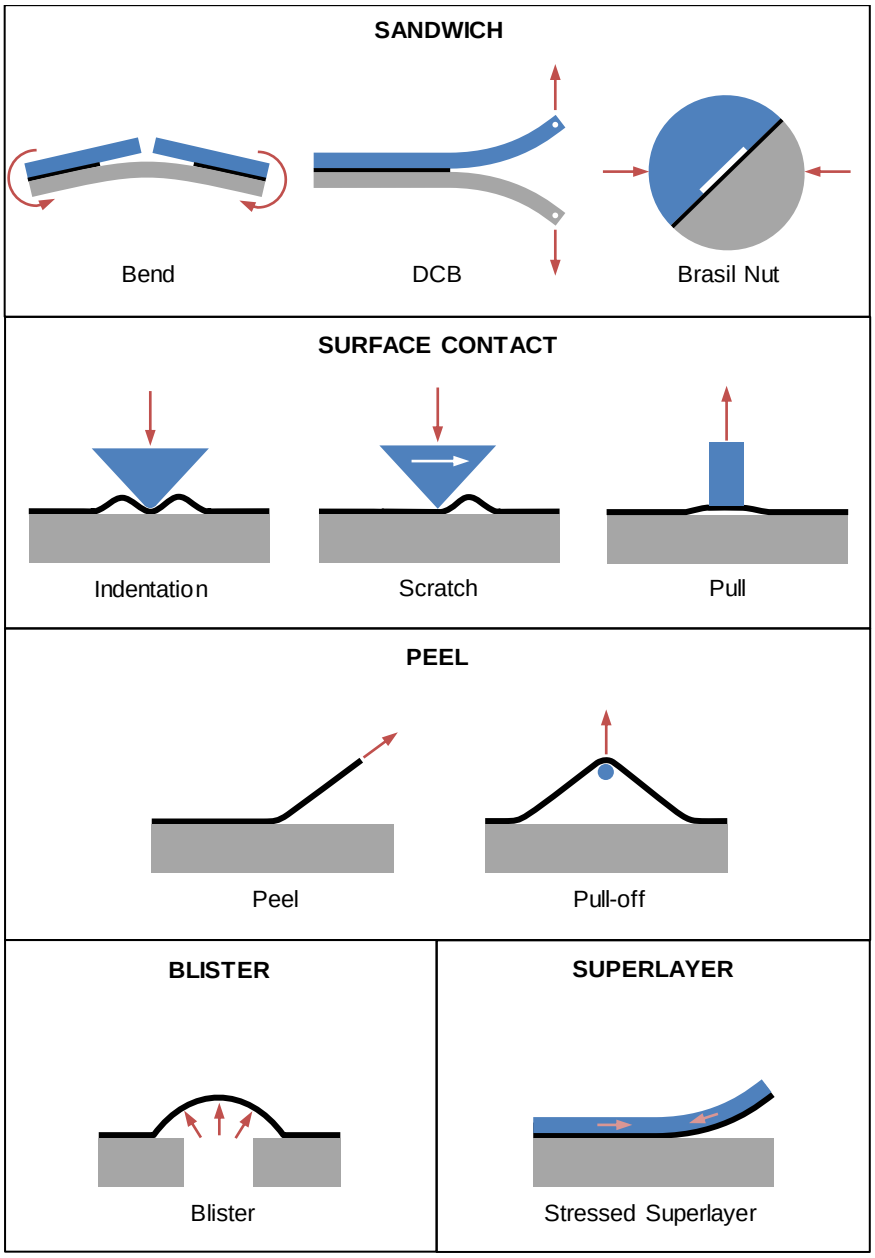

Figure 2.5. Common thin film delamination test techniques.

2.3.1 Established Thin Film Delamination Tests

Sandwich

The traditional sandwich specimen tests involve separating two or more substrates along their bonded interface. These tests are modifications of classical cohesive fracture mechanics specimens for which solutions have been extensively developed, and the

fracture parameter calculations are dominated by the substrate behavior. Some example geometries include the modified compact tension (CT), single cantilever beam (SCB), double cantilever beam (DCB), four-point bend, and Brazil-nut.

Although the interfacial region of the specimen can be made to include thin films, the supporting substrates are large and generally fused together using non-standard fabrication that does not correlate to films as deposited in production. For example, standard diffusion bonding is performed at high temperature and can result in annealed films. Also, the thin film interface can become overconstrained due to the structurally reinforcing substrates.

One of the primary test techniques used in practice, specifically in the microelectronics industry, is the four-point bend test. The multilayered structure and bending loads are similar to the stresses induced within microelectronic systems. Fabrication of the test specimen involves assembling the sandwich structure and cutting a vertical notch into one of the substrates [30]. Upon bending, the notched substrate is cleaved and the resulting stress concentration causes delamination between the bonded substrates. Multilayered film stacks have also been incorporated in order to determine the weakest interface [31]. Unlike the DCB test, the ERR does not depend on the debond length as long as the crack is within the applied supports, thus simplifying the analysis.

However, in addition to the potentially non-representative films and interfaces, there are difficulties with executing the test in practice. Even with embedded pre-cracks, there is a tendency for the crack emanating from the vertical notch to continue straight through the test sample rather than make the required 90° turn into the bonded interface [32]. When delamination does occur, it is also rarely symmetrical as assumed by the analytical models.

Surface Contact

Surface contact techniques involve locally disturbing a film to cause delamination from the underlying substrate. Several different examples of this approach are discussed below, such as the scratch, indent, and pull test. Since these techniques involve precise direct contact with the test specimen near the crack tip, the resulting stress fields are often complicated and the required setup involves sophisticated fixturing and equipment. Also, for thin films embedded within layered structures, surface contact loading is often very different from the loading conditions experienced in the field.

An indenter technique, normally used to characterize a film's elastic modulus and hardness, can also be used to study brittle delamination between a thin film and rigid substrate. The indentation from a hard, sharp stylus tip that is driven vertically into the film can induce buckling and cause a ring shaped delamination to form and propagate radially outward from the contact zone [33]. Plane-stress and plane-strain conditions can be achieved with different indenter geometry, and the phase angle also changes with the crack size [34]. However, it can be difficult to cause delamination of ductile materials due to the film's ability to dissipate energy through plastic deformation rather than fracturing at the interface. Furthermore, very thin films can result in the indenter penetrating into the substrate which additionally complicates the stress fields. For such cases, the film can be coated with a stiff and highly stressed superlayer to create the necessary constraints to initiate delamination, yet the results can be somewhat inconsistent [35].

In the scratch method, a stylus is dragged across the sample surface, and can initiate an interfacial crack either through sufficient normal force at the tip [36] or by contacting the edge of a patterned film strip with an embedded pre-crack [37]. Like the indenter technique, the scratch test suffers from similar limitations since it is designed to transfer the load to the interface through a stiff elastic film, and is therefore not well suited for testing of thin ductile films.

Alternatively, the pull-test employs a flat stylus tip which is directly bonded to the top surface of the film, and then lifted to initiate a circular delamination at the film-substrate interface [38, 39]. This test configuration requires fixturing similar to that of the tensile test, and is very sensitive to any misalignment which can cause a bending moment at the contact point. The bonding process for fusing the loading tip to the film surface can also affect the natural state of the film-substrate interface. Furthermore, it can be difficult to decouple the interfacial and cohesive failure elements resulting from the pull-test, and consequently there is often significant variation in delamination behavior [40]. Thus, the pull-test is more appropriately used as a qualitative measure of adhesion.

Peel

The peel test requires pulling a partially detached film at an angle from a rigid substrate. This is a well-documented technique with a history of studying delamination of many types of film material due to its simple preparation and straightforward execution. The interfacial crack tip position is easily observable during testing, and a variety of mode mix can be applied by adjusting the peel angle from between 0 and 180 degrees.

For an elastic peeling process, the force of peel can be directly linked to the interfacial adhesion energy [41]. However, there can be significant plastic dissipation which becomes more pronounced for thinner films [42]. Additional complications result from testing of very thin films with thickness less than several tens of microns, as the peel test can result in rupture of the film due to severe deformation either at the crack tip or near the mechanical grips [43]. Variations of the peel test, such as the pull-off test [44], have been developed to alleviate some of these issues but setup remains a challenge for microscale specimens.

Blister

Blister tests are comprised of a partially released film membrane which is then delaminated from an anchoring substrate. Most commonly, the membrane is internally pressurized to facilitate the delamination driving force, thus circumventing any mechanical contact with the film. Pressure is applied to the membrane by injecting either a liquid [45] or pressurized gas [46] in the space between the film and substrate. Interfacial fracture parameters are then related to the critical pressure at which delamination occurs as well as the deformed geometry of the film.

The major disadvantage of the blister test technique is that specimen fabrication and experimental setup is generally complicated. Drilling into the substrate is required to provide access for the pressurized fluid to enter the interface gap. The sample and fixture must then provide a hermetic seal for the driving fluid, and precise flow control is required to regulate the pressure. Additionally, very thin or ductile films may also rupture under pressure rather than delaminate.

Another drawback of the blister test is that the crack propagation is often non-uniform and results in irregular blister shapes. This effect is exacerbated by residual compressive stresses in the film which can cause the film to buckle [47]. Some of these behavioral limitations are addressed with the modified “island” [46] or “peninsula” [48] blister geometry, where the membrane has an annulus shape and the critical pressure delaminates the film from the small pillar at the center, rather than radially outward. However, sample preparation is still an issue, as is the difficulty with applying cyclic pressurized loading for a fatigue delamination study.

Stressed Superlayer

The stressed superlayer technique is a convenient fixtureless and noncontact method to characterize interfacial fracture. Unlike the previously described techniques, no external work is applied to the system, but rather the energy for delamination comes

from the stored intrinsic energy. In this technique, a stiff and highly tensile stressed material is deposited on top of the peeling film of interest, and provides the energy required to spontaneously delaminate the film from the underlying substrate [49].

Since the energy for delamination is a function of the superlayer stress and thickness, the test must go through several iterations with varying superlayer properties in order to bound the critical value of the interfacial fracture toughness. Recent modifications to the superlayer test have included a patterned release layer between the film and substrate such that different crack driving forces can be achieved with the same superlayer through variations in the film/substrate contact area [50, 51]. However, the main disadvantage of this technique is that the internal stress of the superlayer is fixed once the specimen is fabricated, and so it is not amenable to provide cyclic loading for a fatigue delamination study.

CHAPTER 3

OBJECTIVES AND SCOPE OF RESEARCH

The objectives of this research are the design, development, demonstration, and critical analysis of a new experimental test technique for thin film fracture and fatigue characterization. This work is focused on a common and technologically relevant thin film material system; however, it is expected to facilitate the testing of a wide range of film interfaces and loading conditions for which interfacial fracture data is currently unavailable. Furthermore, analytical and numerical models of the proposed test will be developed as part of this work. The details of the scope of research are outlined in the following sections.

3.1 Desired Test Features

Current interfacial fracture test techniques are limited in their scope either because of non-representative sample fabrication, cumbersome experimental setup, or restricted loading conditions. A robust and widely useful technique for thin film interfacial characterization should therefore have the following characteristics: (1) ability to test micro- and nano- scale film thicknesses; (2) precise and fixtureless loading; (3) capable of monotonic and cyclic loading; (4) simple specimen fabrication with representative films and interfaces; (5) simple and predictable mechanics; (6) easily observable crack propagation; and (7) amenable to testing under various environmental conditions. The development of a new experimental test technique that can incorporate all of these characteristics would be valuable to the community. Thus, the focus of this work is to develop and demonstrate an innovative test technique for characterizing thin film interfacial delamination.

3.2 Specimen Fabrication

The test specimen must feature representative films and interfaces, and should be simple and cost effective to fabricate. Therefore, a batch fabrication and assembly process needs to be developed which utilizes conventional cleanroom processing with minimum photolithographic process steps. The sample preparation should be robust and be able to produce multiple test specimens on a single substrate.

In addition, the specimen should be functionalized with the ability to induce fracture without requiring physical contact through mechanical fixtures. This ability would present a key advantage over most other test techniques which suffer from issues regarding handling and fixturing of delicate test specimens.

3.3 Experimental Setup and Execution

Interfacial fracture characterization experiments must feature simple and straightforward setup. Most current techniques rely on large and high resolution actuation equipment, such as MTS machines, in order to apply loads and displacements directly to the test specimen. Instead, the new test technique should incorporate an alternative method of applying non-contact loading with a high degree of precision using compact and low cost equipment. Furthermore, the setup must be amenable to both monotonic and cyclic fatigue loading.

Measurement of the specimen deformation and resulting interfacial crack propagation under load must be accomplished *in situ*, preferably through microscopy or other optical techniques. Thus, since both the loading and measurement mechanisms are achieved remotely, the sample can potentially be enclosed within an environmental chamber for conducting fracture experiments under temperature and humidity conditions.

3.4 Analytical and Numerical Analysis

Finally, appropriate analytical and numerical models must be developed in order to extract the critical fracture parameters from the experimental data. These include analysis of the interfacial fracture mechanics through closed form solutions as well as through finite element models. As this work focuses on the interfacial peeling of thin ductile films, both elastic and plastic effects must be considered.

Analytical approaches are typically developed for steady-state delamination conditions. However, typical finite element approaches attempt to characterize the fracture parameters through one- or two-step methodologies, which cannot capture the mature steady-state condition for an elastic-plastic delamination process. Therefore, a new finite element strategy must be developed in order to simulate the evolution of an interfacial crack from its initial to steady-state condition. Furthermore, additional material hardening mechanisms, such as strain gradient plasticity, should be considered where appropriate.

CHAPTER 4

MAGNETICALLY ACTUATED PEEL TEST DESIGN

The proposed delamination test design is the Magnetically Actuated Peel Test (MAPT). In this approach, a partially released thin film structure is gradually displaced out-of-plane until the peel force exerted on the adherend is sufficient to initiate delamination. The actuation force is supplied by the magnetic interaction between a permanent magnet assembled onto the film structure and a nearby electromagnet. With precise control of the current supplied to the electromagnet (and thus force exerted on the assembled permanent magnet), a noncontact, load-controlled peel test is performed. The proposed test has several key elements: (1) electromagnetic actuation provides the driving force needed for delamination propagation, and thus does not require any fixtures to apply loads; (2) an optical profiler monitors the delamination propagation in situ; (3) a wide range of loading amplitude and frequency is obtainable by adjusting the current supplied to the electromagnet generating the external magnetic field; (4) sample preparation involves only two photolithography steps and results in representative as-deposited films; (5) tens to hundreds of test samples can be batch fabricated onto a single wafer; (6) applied loading and delamination detection methods are suitable for both monotonic and fatigue crack characterization; and (7) samples can be placed within an environment of excessive temperature and humidity while the load is modulated by an external magnetic field.

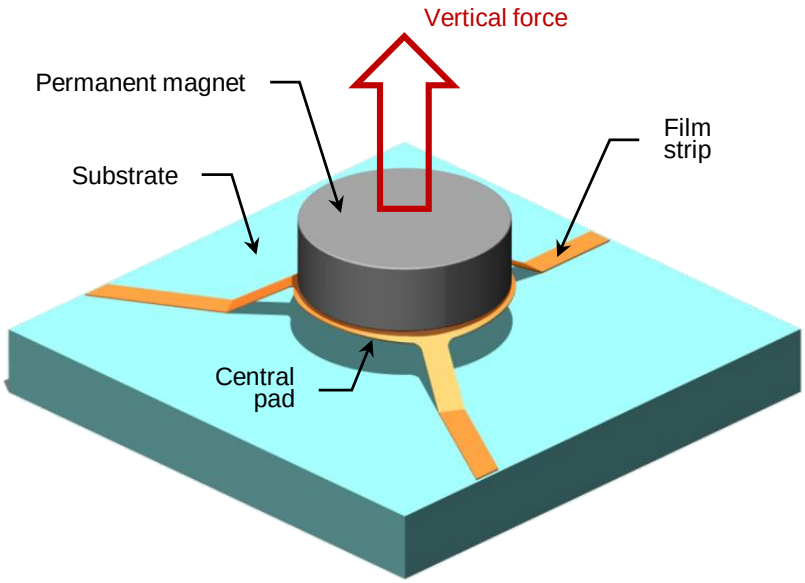

Figure 4.1. MAPT schematic showing vertical displacement of central pad and attached permanent magnet due to an applied magnetic force.

4.1 Test Design

The MAPT design features a patterned thin film on a rigid substrate such that three strips of film extend radially outward from a circular central pad as shown in Figure 4.1. The central pad and adjacent portion of the attached strips are first selectively debonded from the substrate by removal of an intermediate sacrificial layer. The resulting released film structure features a floating circular pad which is anchored to the substrate by three constant width strips, or "legs". The released pad serves as a platform for the subsequent attachment of a permanent magnet using a surface mount epoxy. During the delamination experiment, the fully assembled specimen is situated above an electromagnet of opposing magnetic alignment as in Figure 4.2a. Before power is supplied to the electromagnet, the sample is at rest with an initial interfacial pre-crack of diameter 2a created by the removal of the sacrificial layer (Figure 4.2b-I). With precise control of the external magnetic field strength (i.e. voltage V applied to the electromagnet) and separation gap δ, a calibrated repulsive magnetic force P lifts the permanent magnet and attached central pad, and in the process imposes a peel force along

the three anchoring film strips (Figure 4.2b-II). Once the peel force reaches a critical value, delamination along the film strip/substrate interface will progress (Figure 4.2b-III). Therefore, with knowledge of the critical peel force, associated peel angle, geometry, and mechanics of the film/substrate system, the fracture toughness of the interface can be inferred.

For monotonic interfacial fracture characterization, the load is steadily increased until peeling is observed as described above. Alternatively, for an interfacial fatigue crack propagation study, the specimen can be cyclically loaded at a constant subcritical value by supplying AC power to the electromagnet. In this test mode, characteristic Paris Law parameters that relate crack growth rate to the applied cyclic load can be determined. Thus, the primary focus of the MAPT design in this work is to study interfacial delamination under monotonic and fatigue conditions. In addition, the test design can also be used to perform material characterization of the thin film strips, since the vertical compliance of the released structure is dependent upon the tensile stress-strain behavior of the anchoring film strips.

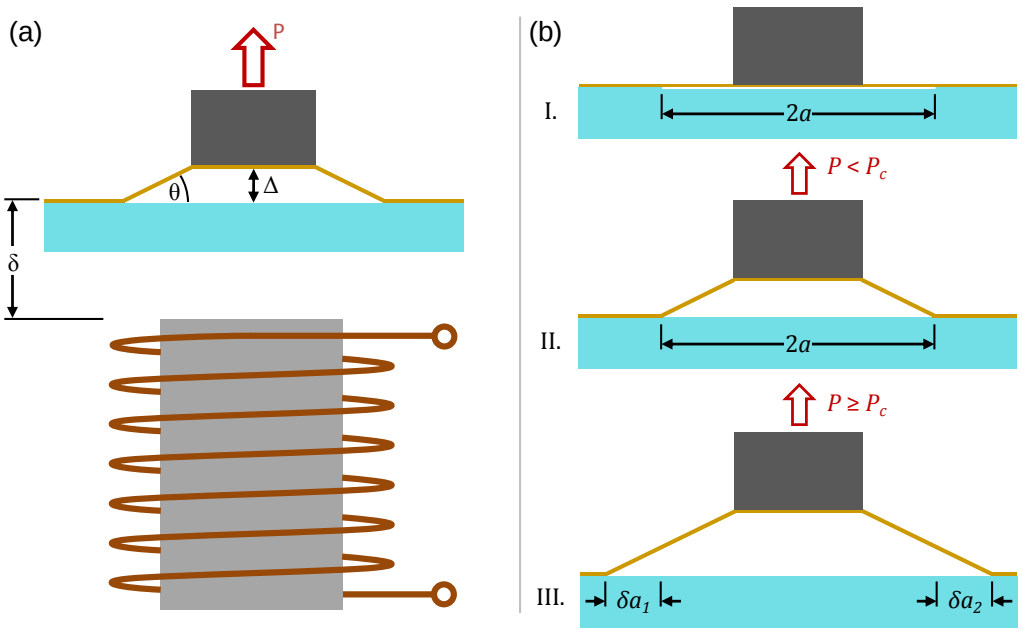

Figure 4.2. (a) Side view of test specimen at a fixed distance δ above the driving electromagnet. An applied magnetic force *P* results in vertical displacement Δ of the central pad which imposes a peel force at an angle θ along the anchoring strips. (b) Stages of MAPT: (I) at rest after removal of sacrificial layer; (II) initial displacement due to application of magnetic force; (III) onset of peel at critical load.

The use of magnetic loading in general allows for a fixtureless test design, noncontact actuation, and elimination of some of the practical issues involved with handling the test specimen and applying the load through mechanical means. In addition, there are several more key advantages of the proposed MAPT design in particular. By using three anchoring strips rather than one or two, the permanent magnet is restricted from rotation during actuation and maintains its orientation with respect to the driving electromagnet; thus the applied force is uniform and strictly controlled by the electromagnet current. Also, since the driving electromagnet is beneath the test specimen, the area above the specimen is free of obstruction for an optical profiler or other device to capture the out-of-plane deflection and hence determine both the strain in the released film and the progression of delamination. Furthermore, as the external magnetic field is generated away from the sample, the test specimen can be easily placed in temperature/humidity chambers to perform mechanical characterization under various environmental conditions. As most materials in MEMS, microelectronic, and other thin

film systems have weak or negligible magnetic properties, a wide variety of material systems can be tested so that the only magnetic interaction is between the external field and the assembled permanent magnet. In the proof-of-concept test specimens developed in this work, the interface of interest is between electroplated Cu films on Si substrates.

4.2 Magnetic Actuation

Several examples of magnetically actuated micro-devices have been developed for various applications, such as for micropumps [52], microfluidic valves [53], and paddle-type actuators [54-56]. These devices feature movable structures that are functionalized with a magnetic material, and forces are thus imposed on the structure in response to an applied external magnetic field. In fact, the concept of utilizing magnetic actuation for an interfacial fracture characterization test has already been proposed previously, and featured a thin film cantilever with evaporated ferromagnetic material at the tip [57]. However, the design of this test technique was unable to create high enough forces to propagate an interfacial crack. Thus, one of the primary advantages of the MAPT design is that much larger and more predictable forces are achieved by using a macroscale permanent magnet versus a thin ferromagnetic film.

A ferromagnetic material, or "soft" magnet, is comprised of mobile and disordered magnetic dipoles, which tend to align along the same direction as with an applied external magnetic field H. As the dipoles realign in response to the external field, an internal magnetization M develops from the cumulative effect of dipole realignment, such that $M=H$. Within a uniform external field, the ferromagnetic body will undergo an applied moment in order to most efficiently develop a matching M field by aligning the body's long dimension with the external field. However, in the presence of a magnetic flux gradient, the body will undergo both a moment as well as an attractive translational force in the direction of stronger gradient. Therefore, ferromagnetic materials are

attracted to a nearby permanent magnet or active electromagnet which projects a non-uniform magnetic field in space.

Permanent magnetic materials, or "hard" magnets, have an intrinsic magnetization regardless of the presence of an external field. Thus, two permanent magnets will experience a repulsive force when their like poles are aligned. Closed form solutions have been developed for the magnetic force between two identical magnets with aligned fields [58]. However, differences in scale, geometry, material, or orientation between the two magnets can drastically complicate the magnetic field interaction and usually require numerical analysis methods to calculate the resulting forces.

In general, permanent magnets can generate more force than ferromagnetic materials, and they can be used for both attractive and repulsive actuation. Electrodeposition processes have been developed for hard magnetic alloys, such as CoPt and CoNiMnP; however, the resulting structures are generally brittle and very highly stressed [59]. In addition, the magnetic force is roughly proportional to the volume of the magnetic material, and thus it is challenging to electrodeposit and pattern a sufficient amount of magnetic alloy in order to generate forces large enough to be used in a fracture test specimen. Hence, the MAPT design incorporates the assembly of pre-fabricated permanent magnets made from neodymium (NdFeB) - the strongest rare earth magnetic material commercially available. Further details of the magnet and assembly process are discussed in Chapter 6.

CHAPTER 5

ANALYTICAL PEEL MODEL

5.1 Background

The delamination forces borne by the anchoring film strips in the MAPT design are identical to that of the traditional peel test. The peel test has been a widely studied technique to characterize interfacial fracture strength. As shown in Figure 5.1a, a flexible film is peeled off an underlying substrate by a force F acting along an angle θ. However, when applied to very thin films with thickness less than several tens of microns, the peel test can result in rupture of the film due to severe deformation either at the crack tip or near the mechanical grips. This kind of cohesive failure can be mitigated by using a modification of the peel test called the pull-off test introduced by Gent and Kaang [44], where a vertical load P applied at the center of a debonded strip imposes a simultaneous peel force on both adhered ends of the film (Figure 5.1b). Here the low angle of peel limits the bending stresses near the crack tip, and the load is typically applied by a horizontal pin underneath the debonded strip rather than mechanical grips. The MAPT design is most analogous to the pull-off test, except that there are three debonded strips rather than two, and these strips are coupled to the bottom surface of a cylindrical permanent magnet supplying the vertical load.

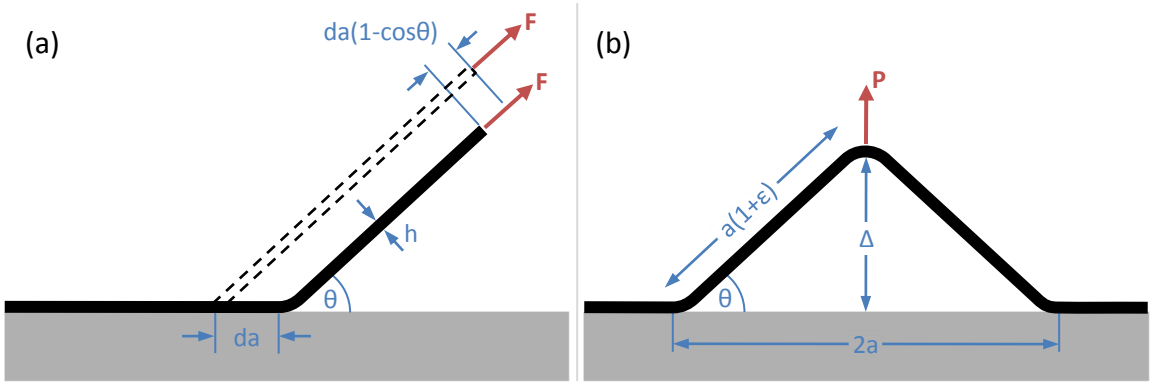

Figure 5.1. (a) Peel test as diagramed by Williams [56]. (b) Pull-off test.

Many theoretical models specific to the peel and pull-off tests can be found in the literature. For displacement- or load-controlled delamination (as in the MAPT design), the change in external work is a straightforward calculation. However, the challenge is in accurately calculating the change in strain energy per crack growth *dU*/*dA*. When there is significant plastic contribution to the strain energy, the calculation becomes even more challenging.

5.2 Uniform Tension Model

As a simple first order peel test model, Williams [60] assumes a flexible peel strip on a rigid substrate with uniform tensile strain in the released strips (i.e. ignoring bending), and develops an expression for the applied FER as

$$\Gamma = \frac{F}{b}(1 - \cos\theta + \varepsilon) - h\int_0^{\varepsilon} \sigma \cdot d\varepsilon, \tag{5.1}$$

where F is the peel force, b is the strip width, θ is the peel angle, ε is the tensile strain, h is the strip thickness, and σ is the tensile stress. The Williams model can be adapted to the MAPT design by incorporating three peel strips that are coupled to the central pad. Assuming symmetry and an initially flat and stress-free film, the following additional constraints can be imposed:

$$cos\,\theta = \frac{1}{1+\varepsilon}, \tag{5.2}$$

$$P = 3F\sin\theta, \tag{5.3}$$

where P is the vertical magnetic force. Substituting (5.2) into (5.1) and solving for Γ/h results in

$$\frac{\Gamma}{h} = \sigma\frac{\varepsilon(2+\varepsilon)}{1+\varepsilon} - \int_0^{\varepsilon} \sigma \cdot d\varepsilon. \tag{5.4}$$

Equation (5.4) shows the ratio of FER to film thickness as a function of tensile stress and strain. Alternatively, the ERR can similarly be calculated by incorporating only the elastic strain energy which results in

$$\frac{G}{h} = \sigma\frac{\varepsilon(2+\varepsilon)}{1+\varepsilon} - \frac{\sigma^2}{2E}, \tag{5.5}$$

where E is the elastic modulus of the film. Additionally, (5.2) and (5.3) can be combined into

$$\frac{P}{bh} = 3\sigma\frac{\sqrt{\varepsilon(2+\varepsilon)}}{1+\varepsilon}. \tag{5.6}$$

Since Equations (5.5-5.6) are in terms of only stress and strain, we can implicitly solve for G or Γ in terms of the magnetic force and cross section of the film strip for a given film constitutive model. It should be noted that the film material is not necessarily limited to an elastic analysis, since a nonlinear stress-strain relation can be used to model the elastoplastic stretching of the adherend. A nonlinear model for Cu thin films derived from [61] was used for calculations, which can be approximated with the elastic-plastic power law hardening constants E = 110 GPa, K = 1490 MPa, and n = 0.24, where K and n are the hardening modulus and hardening exponent, respectively. The ERR and FER are compared as a function of the magnetic force in Figure 5.2. The two curves are observed to diverge meaningfully for P/bh > 75 μN/μm^2, which is beyond the force level applied to MAPT specimens in this work. Therefore, it is sufficient in this case to use the loading amplitude ΔG for characterization of the interfacial delamination between the peeling film and substrate. Additionally, the length of the peeling strip does not affect the calculations. Therefore, ΔG is only dependent on the magnetic load and is stable as the delamination progresses. Comparison of the analytical model with a more sophisticated finite element approach as discussed in Chapter 10 shows that the uniform tension

assumption appropriately captures the ERR for the load range applied in experiments, and can be used as a conservative estimate of the critical ERR for a given peeling load.

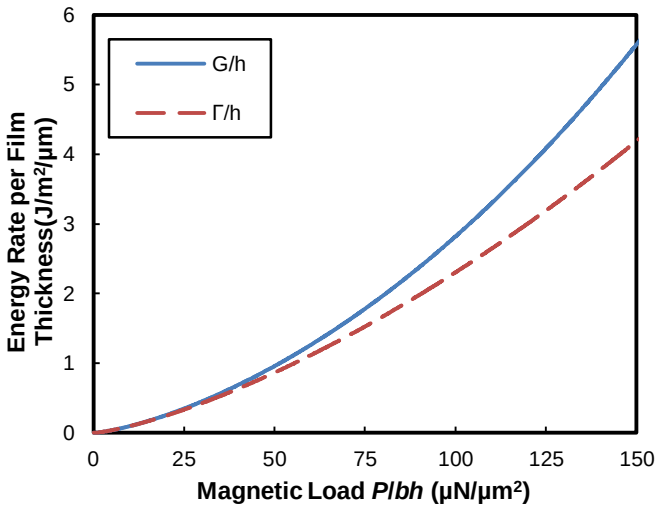

Figure 5.2. Comparison of ERR and FER as a function of the applied magnetic load.

5.2.1 Effect of Slack

The released film strips of a MAPT specimen may not lie perfectly flat on the substrate, but instead have some residual slack after removal of the underlying sacrificial layer. As a result, there can be additional displacement of the film strips under load as shown in Figure 5.3.

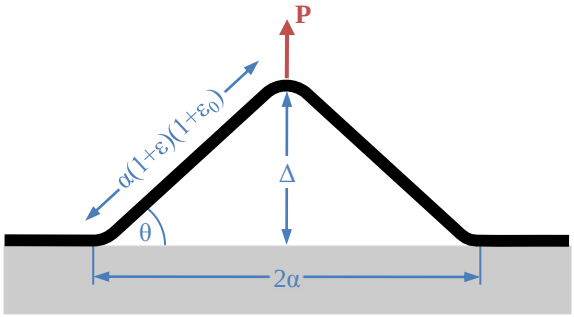

Figure 5.3. Pull-off test with slack strain ε_0.

The displaced geometry of the film with initial slack has the constraint

$$\cos\theta = \frac{1}{(1+\varepsilon)(1+\varepsilon_0)}, \tag{5.7}$$

where ε_0 is a measurement of the inherent slack in the film but does not contribute to the mechanical strain. If there is no initial slack (i.e. $\varepsilon_0 = 0$), then Equation (2) simply reduces to Equation (5.2). Consequently, Equations (5.6) and (5.4) can be updated to include the slack term such that,

$$\frac{P}{bh} = 3\sigma\sqrt{1 - \frac{1}{\left((1+\varepsilon)(1+\varepsilon_0)\right)^2}}, \tag{5.8}$$

and

$$\frac{\Gamma}{h} = \sigma\left(1 - \frac{1}{(1+\varepsilon)(1+\varepsilon_0)} + \varepsilon\right) - \int_0^{\varepsilon} \sigma \cdot d\varepsilon. \tag{5.9}$$

Using the same constitutive model for the film as in Section 5.1, the impact of slack on the resulting peel angle is shown in Figure 5.4. For applied force values $P/bh <$ 150 μN/μm^2, it is clear that even a relatively small amount of slack ($\varepsilon_0 = 0.2\%$) can affect the resulting peel angle to be ~1° greater than if the film was initially flat.

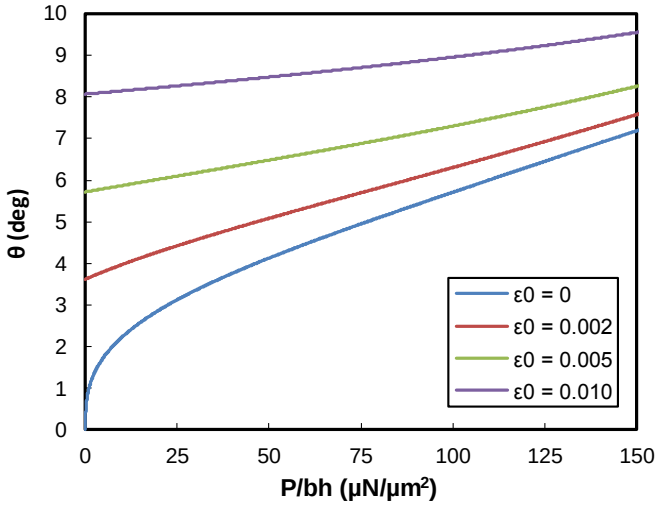

Figure 5.4. Effect of slack on peel angle.

Even though the peel angle may be sensitive to initial slack, the resulting calculation for the FER is quite insensitive as shown in Figure 5.5. There is virtually no effect on the calculated FER for $\varepsilon_0 = 0.2\%$ despite the increased peel angle. As is

discussed in Chapter 9, the amount of slack in the MAPT specimens in this work was measured to be no more than 0.3%, and therefore did not factor into the calculations for either G or Γ.

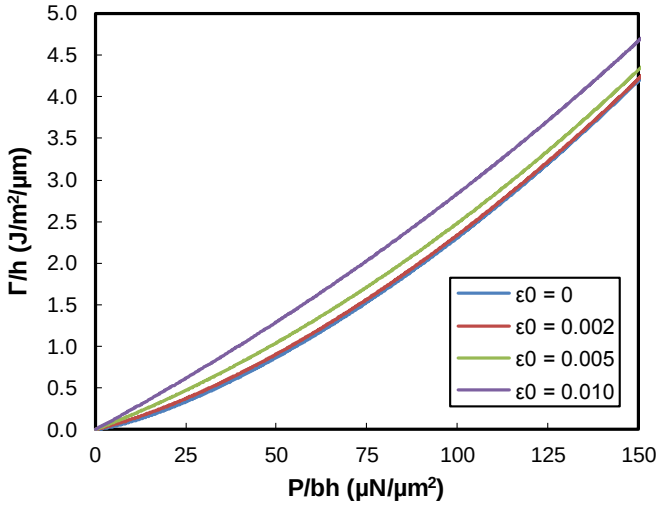

Figure 5.5. Effect of slack on FER.

5.2.2 Effect of Differing Peel Angles

For an ideal test specimen, each of the three identical strips would peel uniformly and endure equivalent peel angles (and thus tensile stress) when subjected to the vertically applied magnetic force. In practice, there can be minor flaws in the specimen and unequal peeling which results in slightly different peel angles amongst the peel strips. For such non-symmetric deformation the tensile force along each strip as shown in Figure 5.6 can be obtained from force balance using

$$P = F_1 \sin\theta_1 + F_2 \sin\theta_2 + F_3 \sin\theta_3, \tag{5.10}$$

$$F_1 \cos\theta_1 = F_2 \cos\theta_2 = F_3 \cos\theta_3, \tag{5.11}$$

where P is the vertical magnetic force, F is the tensile force along the film strip, θ is the released strip angle with respect to the substrate, and the subscripts refer to the strip number. Solving for the tensile force along one of the strips results in

$$F_i = \frac{P \cos\theta_j \cos\theta_k}{\sin\theta_i \cos\theta_j \cos\theta_k + \sin\theta_j \cos\theta_i \cos\theta_k + \sin\theta_k \cos\theta_i \cos\theta_j}, \tag{5.12}$$

where the subscript indices *i*, *j*, and *k* refer to the strip number and are used for brevity. Because the strip angles are generally small (<10°), Equation (3) can be approximated by

$$F \cong \frac{P}{3 \sin\theta_{avg}}, \tag{5.13}$$

where

$$\theta_{avg} = \frac{\theta_1 + \theta_2 + \theta_3}{3}. \tag{5.14}$$

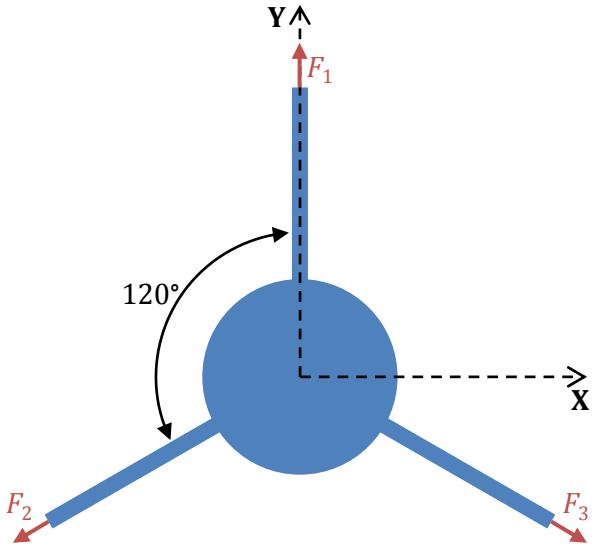

Figure 5.6. Top-down schematic of tensile test specimen.

This result implies that even if the strip angles are several degrees apart, the tensile forces supported by each film strip are equivalent. For example, if the three strip angles are 1°, 1°, and 10°, respectively, then the tensile force calculated from Equations (3) and (4) differ by less than 1%. Therefore, the three strips are assumed to have equivalent tensile stress and the average strip angle from the experimental data is used for calculating the stress.

5.3 Crack Tip Bending

For steady-state peeling of flexible films where the energy of deformation is dominated by the stretching of the adherend, the uniform tension model can be used to accurately calculate interfacial fracture toughness. However, for a ductile peeling process, there can be significant contribution of plastic dissipation in the sharp bend near the crack tip. This extra dissipative energy can result in the uniform tension assumption to overestimate the FER. Kim et al. [62, 63] therefore developed a bending model that accounts for the elastoplastic loading and subsequent unloading of the film as a crack propagates. The bending approach has since been adopted in many peel test studies where the interface is modeled with a cohesive zone formulation, and several candidate two-parameter characterization criteria have been proposed [22]. The validity of the bending model has been so far limited to cases when the film is very thin and the interface is relatively weak based on correlations with finite element approaches [64], however a general analytical formulation for all cases has yet to be developed. These approaches are significantly more complex than the uniform tension assumption, generally require numerical methods for implementation into the analysis, and are beyond the scope of this work.

CHAPTER 6

FABRICATION OF TEST SPECIMENS

For the initial test specimens detailed in this work, Cu film strips are fabricated over a natively oxidized silicon substrate. The main steps of fabrication are outlined in Figure 6.1: (a) patterning of sacrificial layer; (b) seed metallization; (c) doming of thin metal film through polymer reflow followed by additional blanket metal electrodeposition; (d-e) patterning metal film test structure through etching; (f) release to define the initial interfacial pre-crack; (g) epoxy adhesive printing; and (h) assembly of permanent magnet onto the released film structure. Fabrication is relatively simple, requires only two photolithography mask steps, and samples can be batch fabricated to produce tens to hundreds of samples on a single wafer.

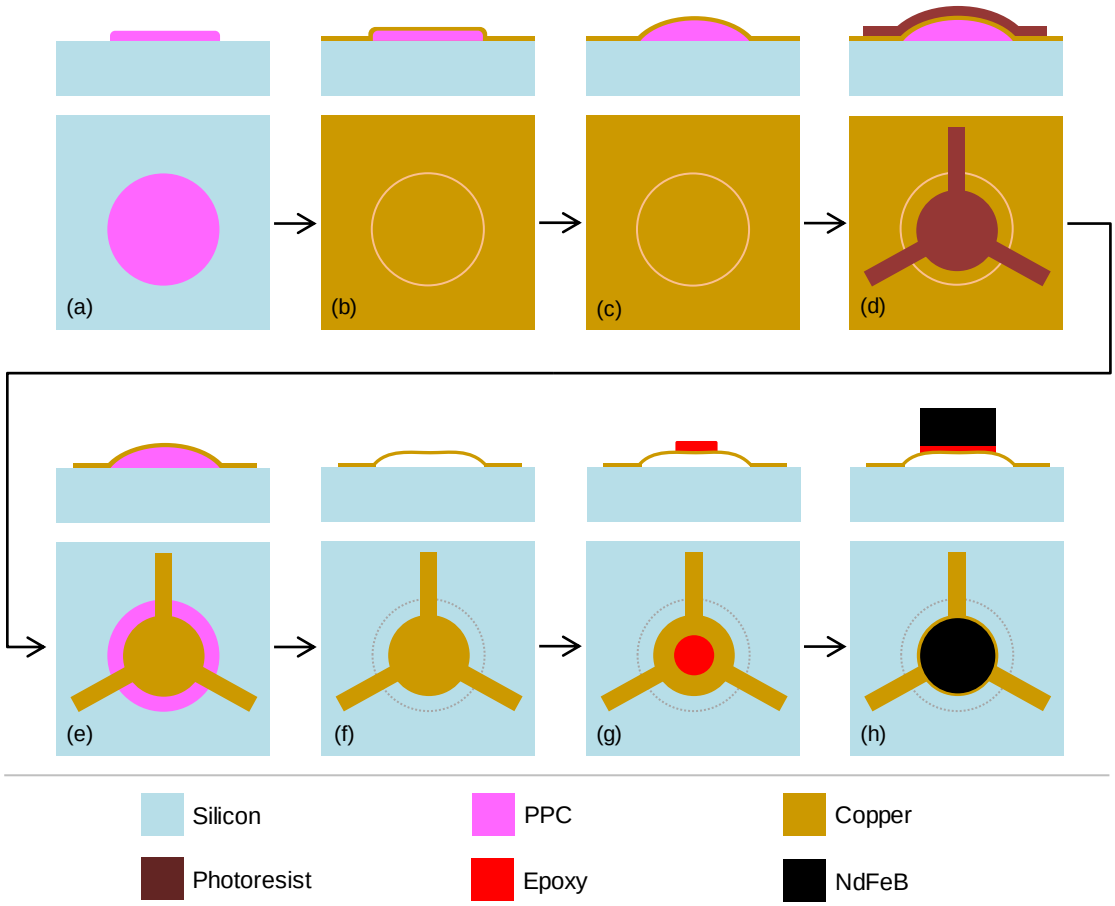

Figure 6.1. Fabrication process of the MAPT test specimen for characterizing interface between Cu film and Si substrate.

In the mask designs used in this research, 36 individual samples were batch fabricated on a 4 in wafer as shown in Figure 6.2. Varying dimensions were used in order to determine their potential impact on adhesion measurement. The Cu pad diameter was 1650 µm for all samples as they were designed for same size permanent magnet. Sacrificial disc diameters of 2150, 2650, and 3650 µm were used to vary the starting delamination length. Peel strips were designed with widths of 25, 50, 75, 100, 150, and 200 µm. Also incorporated into the mask were hash marks alongside the peel strips, which serve as markers to easily determine the position of the delamination edge through

visual inspection. A close-up of the mask design for one example MAPT specimen is shown in Figure 6.3.

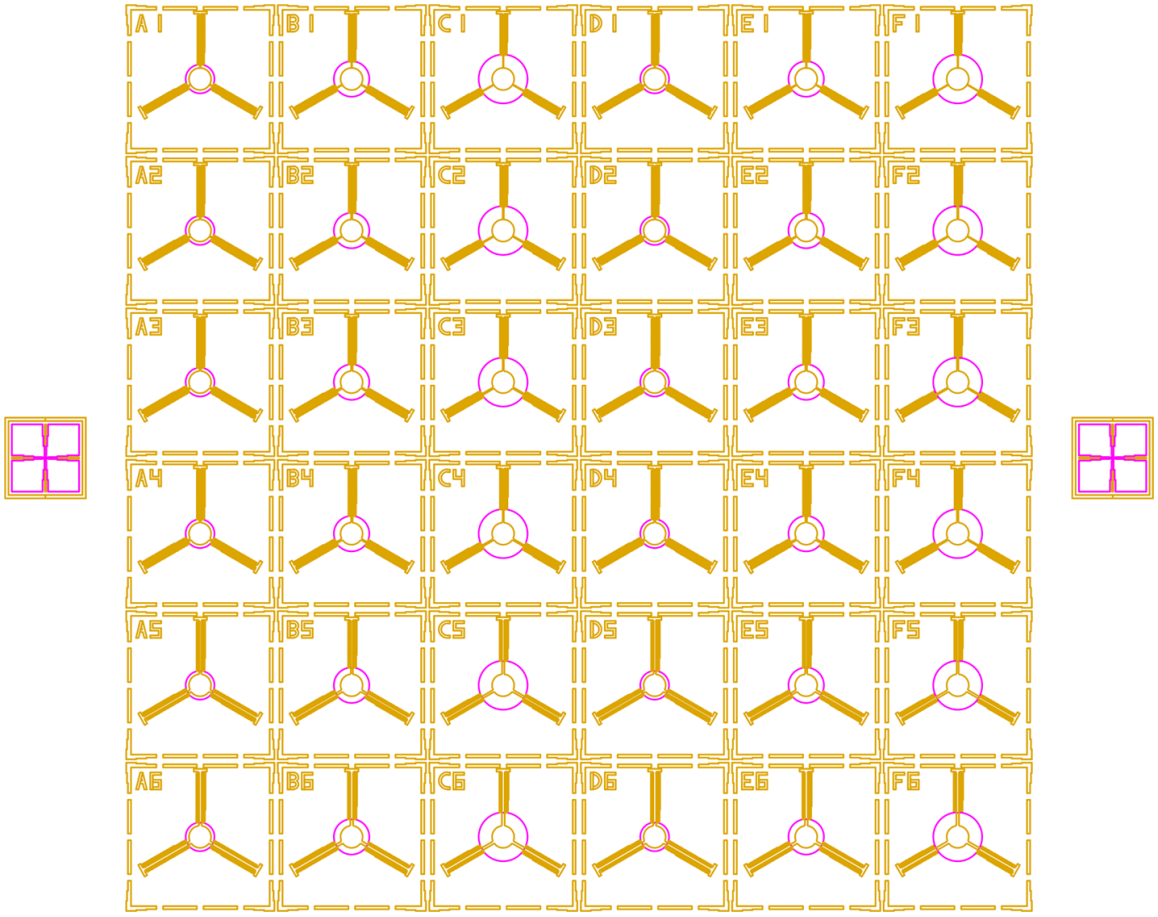

Figure 6.2. Overlay of sacrificial layer photomask (magenta) and metal film pattern (copper).

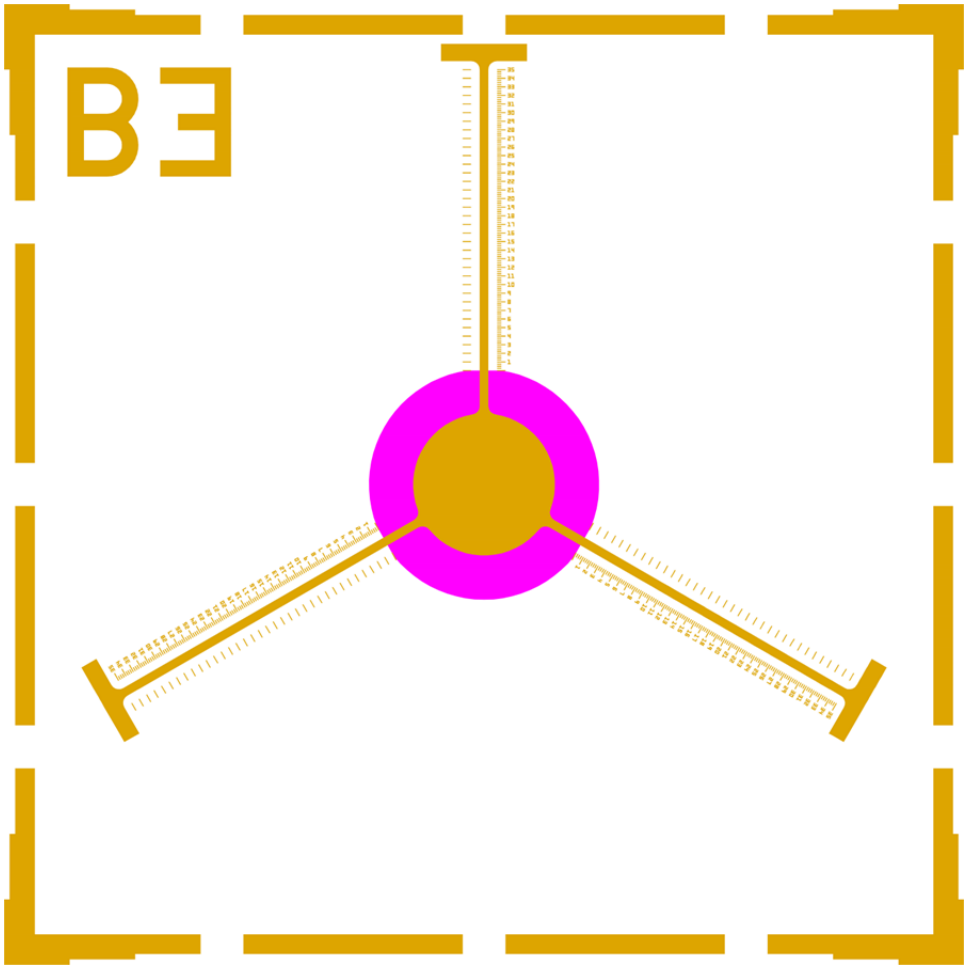

Figure 6.3. Close-up of mask design showing one example MAPT specimen.

6.1 Sacrificial Photoresist

A polypropylene carbonate (PPC) based photoresist was formulated and used in this work to define the sacrificial release layer. PPC and similar polymers have been studied previously for a number of temporary place holder applications in microelectronics [65-69]. Unlike conventional aqueous developed photoresists, PPC is developed thermally. In the particular formulation used, the native PPC decomposes into gas at temperatures above ~150°C. After exposure to deep ultraviolet (DUV) 248 nm radiation, the decomposition temperature drops to ~100°C, and thus allows for positive-tone imaging by subsequent heating to 100-150°C.

PPC synthesized by Novomer, Inc. was diluted into *gamma*-Butyrolactone (GBL) for a 20 wt. % polymer loading. A 3% by weight of polymer photoacid generator (PAG) was added to make the formulation photosensitive. When exposed, the PAG releases an acid that decomposes the PPC into small volatile organic compounds when heated above ~80°C. The formulation was spin coated onto a bare silicon wafer at 3600 rpm for 40 s to a thickness of 3 μm after a soft bake for 2 min at 100°C. DUV exposure (6 J/cm^2) through a photolithography mask and subsequent heating to 110°C on a hot plate for 2 min resulted in patterned discs with diameters of 2190, 2680, and 3670 μm (Figure 6.1a). The remaining unexposed PPC is stable in isopropyl alcohol (IPA), and thus an IPA wash removed any residue left by the exposed photoresist. The patterned PPC discs were then subjected to a DUV flood exposure. The impact of this final exposure step on reflow and decomposition are discussed in the following sections.

6.2 Seed Metal Encapsulation

The use of a domed sacrificial layer rather than a flat layer is significant for two reasons: (1) a sharp and shallow pre-crack as opposed to a stepped profile is created where the film and substrate are initially debonded, and (2) the domed film is more resistant to stiction during the release step as is discussed below. Therefore, a process by which PPC can be reflowed into a dome shape was developed.

The strategy for forming precisely defined domes involves encapsulating the photoresist within a thin flexible membrane in order to confine the volume in which the polymer can reflow. Thus, 500 nm of copper was sputter-deposited onto patterned PPC samples (both exposed and unexposed) as shown in Figure 6.1b using a Denton Vacuum Discovery® DC sputterer. The sputter pressure and source current were the primary parameters affecting sputter deposition rate. As shown in Figure 6.4, the sputter yield increases as the pressure is reduced from 65 to 4 mTorr, and at a fixed pressure of 5.4 mTorr the deposition rate increases linearly with the source current.

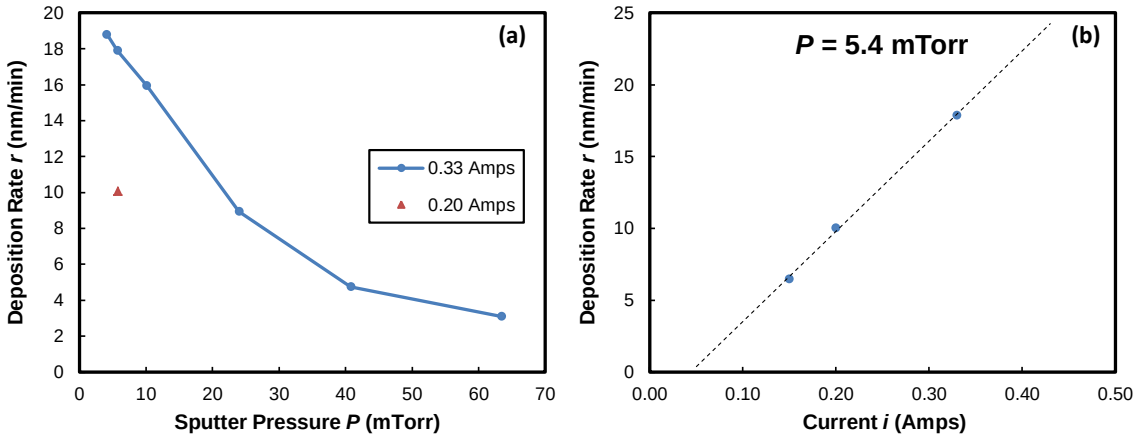

Figure 6.4. Sputter deposition rate for copper (a) versus sputter pressure for a given current, and (b) versus current at fixed sputter pressure of 5.4 mTorr, with linear fit.

At high deposition rates, the PPC often decomposed during sputtering due to significant substrate heating (Figure 6.5a). At high sputter pressure, a low quality copper film with numerous microcracks resulted from potential contamination in the gas chamber (Figure 6.5b). Therefore, an optimized sputter pressure of ~5 mTorr and deposition rate of ~10 nm/min was employed to have uniform copper thickness and a crack-free film.

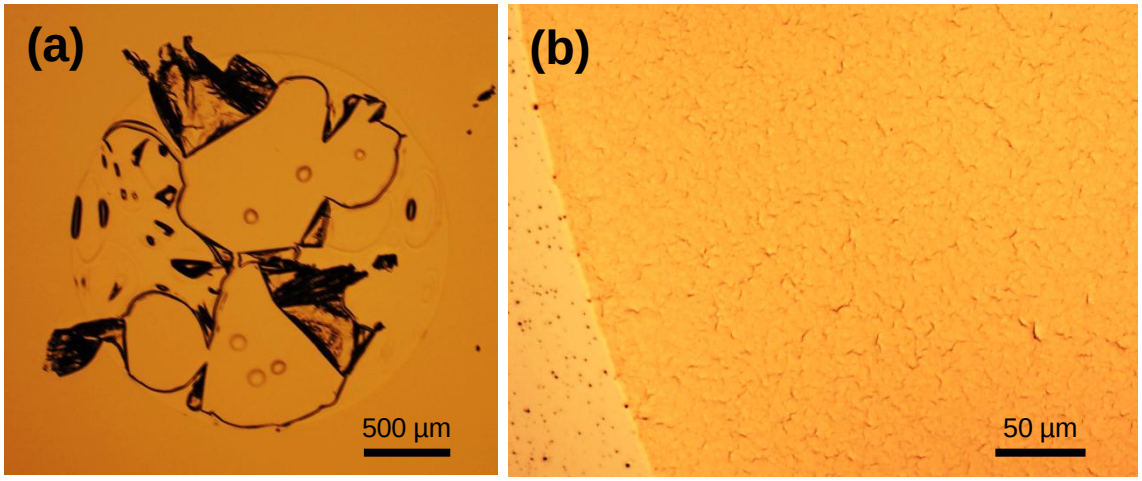

Figure 6.5. Unsuccessful sputtering results: (a) decomposition of PPC during sputtering, and (b) microcracks in Cu film.

6.3 Reflow and Dome Formation

Reflow characterization experiments were conducted to determine the effects of both flood exposure and metal coating on the reflow behavior of the fabricated PPC discs. Four sample sets were considered: bare unexposed PPC, bare exposed PPC, Cu coated unexposed PPC, and Cu coated exposed PPC. Samples were placed on a hotplate set to a series of increasing temperatures from 60°C to 140°C in increments of 10°C. Scanning profiles tracking the reflow progress of PPC were taken after 10 minutes at each bake temperature.

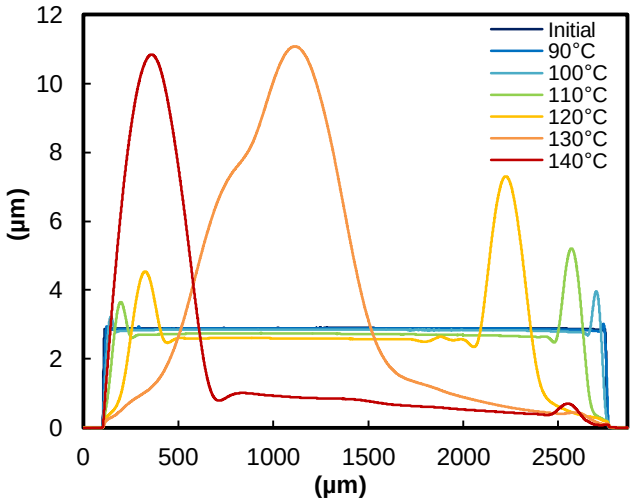

Figure 6.6. Reflow of bare unexposed PPC. Profiles correspond to 10 min of heating at each incrementally increasing hotplate temperature.

Bare unexposed PPC was observed to reflow above 90°C but resulted in highly asymmetrical dome-like profiles. The typical reflow progression for this case started with highly elevated edge beads that coalesced into a large off-center mound (see Figure 6.6). Also, surface tension caused the outer diameter to shrink inwards during reflow, and decomposition of the unexposed PPC was observed to occur at 140°C. Bare exposed PPC, on the other hand, began to decompose above 70°C before reflow could be observed. The Cu coated unexposed PPC was not observed to reflow or decompose at all for the entire temperature range tested. Conversely, Cu coated exposed PPC reflowed above 70°C into perfectly spherical domes (Figure 6.7), with no decomposition apparent

for temperatures up to 120°C. Above this temperature, some samples developed a large protruding bubble indicating significant decomposition of PPC within the dome.

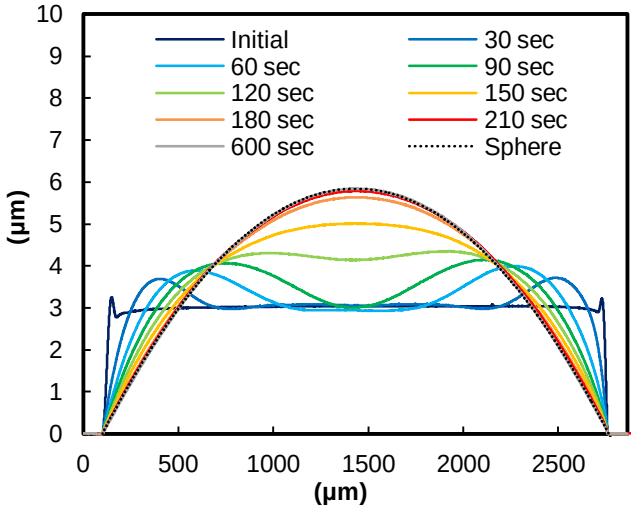

Figure 6.7. Reflow of exposed PPC encapsulated by 500 nm of Cu. Profiles correspond to amount of time sample spent on 100°C hotplate. Stabilized dome matches a spherical cap with a radius of curvature *R* = 15.4 cm.

For practical dome fabrication, the metal coated exposed PPC should be baked at a constant temperature of ~100°C; high enough for rapid reflow yet low enough to prevent the risk of decomposition. The evolution of the dome shape at this temperature is shown in Figure 6.7, and indicates a fully formed dome within less than 4 minutes with no change in curvature for as long 10 minutes. An analytically derived profile of a constant curvature dome is overlaid to show that the stabilized profile is a perfect spherical cap. Images of the encapsulated PPC before and after reflow were taken with both an optical microscope and an optical profiler as shown in Figure 6.8.

The difference in behavior between the bare and sputter coated PPC samples is believed to be attributable to a hermetic sealant effect, where the encapsulated PPC experiences elevated pressure when heated, and thus the characteristic reflow and decomposition shifts to a higher temperature. During reflow a spherical dome should therefore naturally form in order to equalize the pressure contained within a flexible membrane. The volume of the encapsulated PPC was measured to remain constant before and after doming indicating no phase change during reflow. Domes were also

fabricated in the same manner using Al and Ti encapsulants with similar reflow progressions, supporting the claim that the encapsulation effect and not a chemical reaction with the metal coating is responsible for the difference in PPC reflow and decomposition.

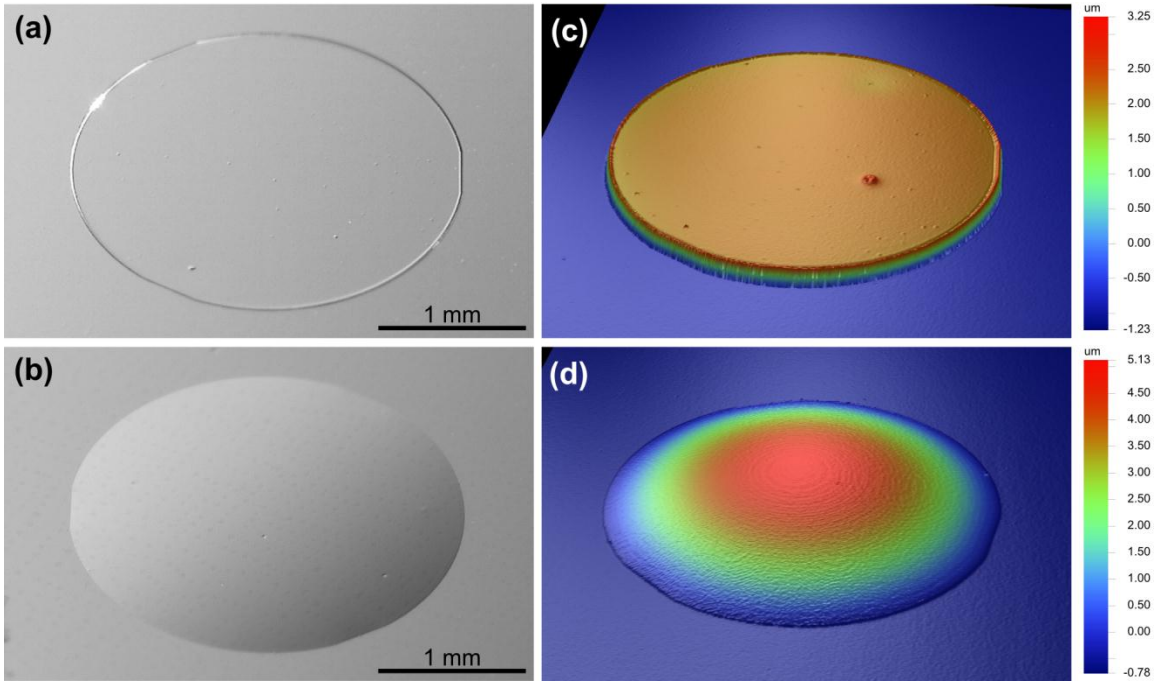

Figure 6.8. Cu coated PPC before and after reflow showing transformation from disc shape to dome shape. (a, b) Optical images taken with Keyence VHX-600 microscope. (c, d) Images generated by Veeco Wyko® NT-2000 optical profiler.

A significant advantage of reflowing the sacrificial polymer within an encapsulant is that the lateral dimensions of the dome are precisely defined. Even with the relatively weak adhesion of Cu to Si, the outer diameter of the PPC did not change after reflow. Also, the final curvature of the dome stabilizes after only a few minutes of heating. Thus, the height and curvature of a reflowed dome can be simply determined by equating the volume of the initial PPC disc to that of a spherical cap of equivalent base diameter using Equations (6.1) and (6.2).

$$V = \frac{\pi}{6} h_f \left(3r^2 + h_f^2\right) \tag{6.1}$$

$$R = \frac{r^2 + h_f^2}{2h_f} \tag{6.2}$$

Where V is the spherical cap volume, h_f is the dome height, r is the base radius, and R is the radius of curvature. It should be noted that the initial profile of the Cu/PPC disc before reflow as shown in Figure 6.7 contains a slightly sloped sidewall and edge bead. Thus, the volume of the initial disc was found to be about 3-5% less than that calculated using $\pi r^2 h$. When designing for specific dome dimensions by this conservation of volume approach, it is therefore important to account for this difference when choosing the appropriate dimensions of the encapsulated PPC disc. The dimensions of the fabricated reflowed domes are summarized in Table 6.1. The three different dome diameters were chosen to accommodate the different released film strip lengths.

Table 6.1. Dimensions of fabricated Cu/PPC spherical domes

Planar diameter d (μm)	Initial disc height h_i (μm)	Dome height h_f (μm)	Radius of curvature R (cm)
2190	3.04	5.75	10.4
2680	3.04	5.84	15.4
3670	3.04	5.89	28.6

6.4 Electrodeposition

After the reflow process, additional Cu was electroplated up to a final film thickness of 1.5-1.7 μm. Pretreatment in a citric acid/hydrogen peroxide solution was done immediately before plating to remove any surface oxides and ensure a strong bond with the seed layer. Electroplating was done using a standard copper/sulfuric acid electrochemical bath [70] with a phosphorus doped copper anode. Trace amounts of polyethylene glycol, bis(sodiumsulfopropyl)disulfide, and janus green B were added to the bath as a carrier, brightener, and leveler, respectively, to improve the quality of the

copper deposition. The sample was plated at room temperature with no agitation and a current density of 10 mA/cm^2 for a copper electrodeposition rate of 13 µm/min.

6.5 Test Film Patterning

A second photolithography step was used to define the MAPT film pattern as shown in Figure 6.1d. AZ-1512 photoresist was chosen as the etch mask because of its low bake temperature so as not to decompose the encapsulated PPC. However, the poor adhesion of AZ-1512 to copper necessitated the use of an adhesion promoter. HMDS-P20 was therefore first deposited at 3000 rpm for 30 s followed by a bake at 90°C for 1 min. AZ-1512 was then deposited at 4000 rpm for 30 s followed by a softbake at 90°C for 1 min. After an exposure dose of 80 mJ/cm^2 at the 405 nm wavelength, the pattern is developed in 300MIF developer for 1 min at room temperature. The effect of the HMDS adhesion promoter on the developed pattern can be seen in Figure 6.9.

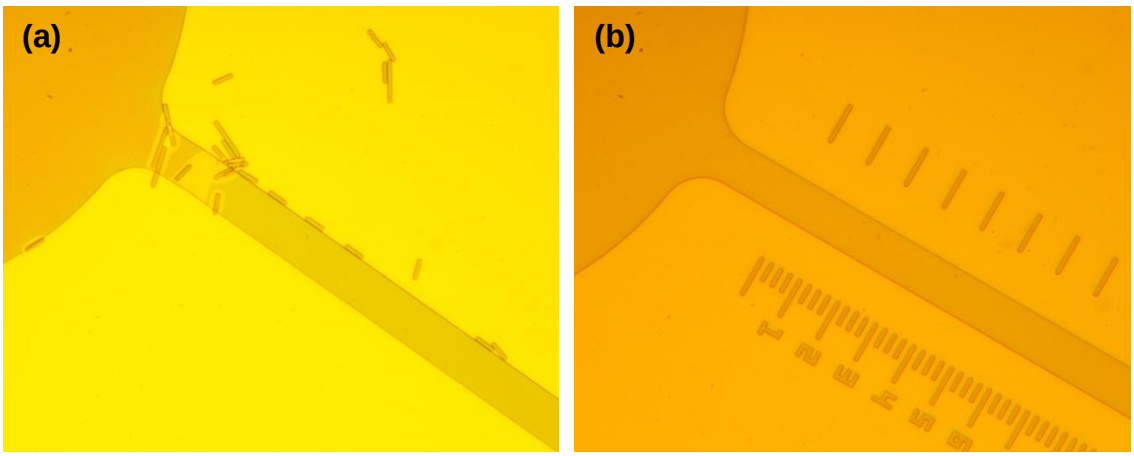

Figure 6.9. Photoresist mask after developing (a) without HMDS adhesion promoter and (b) with HMDS.

A subtractive wet etch was accomplished using diluted Transene APS-100 Cu etchant to define the test film pattern (Figure 6.1e). It was found that a 1:5 dilution ratio into water along with constant sloshing of the solution reduced the copper underetch significantly from over 10 µm to about 3 µm (Figure 6.10). After etching, the PPC is no longer fully encapsulated by the Cu film, facilitating its removal during the release step.

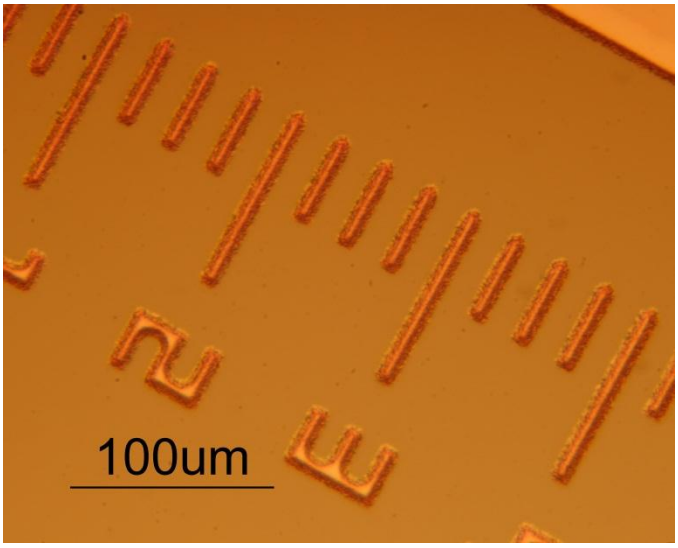

Figure 6.10. Patterned Cu film showing underetch of about 3 µm.

6.6 Removal of Sacrificial Layer

After the Cu pattern is defined, the underlying PPC dome must be removed in order to release the central pad and strip ends from the substrate. For typical sacrificial materials removed by wet etch, stiction forces can cause the released film features to collapse and re-adhere to the substrate [71]. To overcome stiction effects, two alternative release methods are demonstrated: (1) dry thermal decomposition and (2) wet etch and supercritical dry. The thermal release technique requires baking the samples at high temperature within a nitrogen purged oven in order decompose the PPC.

6.6.1 Thermal Release Approach

Test specimens that were fabricated using the thermal release technique were first immersed in IPA to dissolve the photoresist etch mask and then baked at 250°C for 2 hours. Although a handful of specimens were successfully released in this manner, the majority of samples suffered from relaxation of the thin Cu dome and re-adhesion of the central pad to the substrate during the bake process as shown in Figure 6.11. While it was expected that the thin flexible Cu film would somewhat collapse upon removal of the underlying PPC, the resulting surface contact often resulted in a strong bond that

rendered the specimen unusable for thin film characterization. The cause of this re-adhesion is unknown, and was problematic for a wide range of bake temperature profiles. For comparison, non-domed samples were also fabricated and baked, but achieved no success with all cases suffering from Cu re-adhesion. The domed samples performed marginally better than the flat ones, most likely because their initially curved surface would warp and ripple during relaxation and limit the available contact area to the substrate. It is expected that lower aspect ratio domes with thicker and stiffer metalized features would be more reliably released using thermal decomposition. However, due to the low yield of samples for the thin film characterization test and the need for a low temperature fabrication option, an alternative wet release technique was pursued.

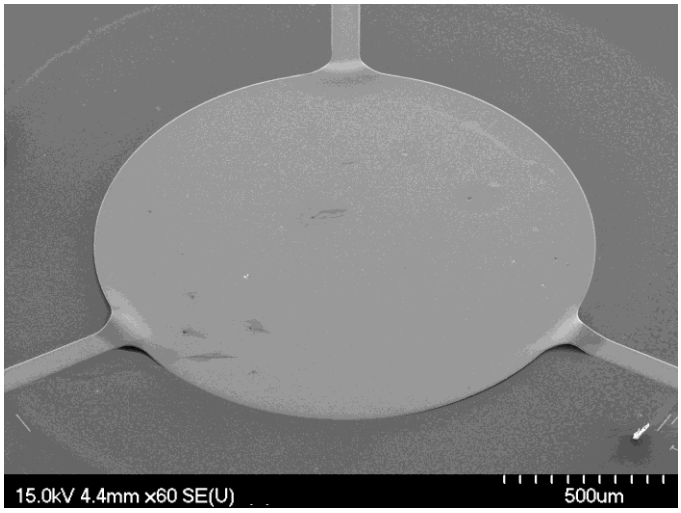

Figure 6.11. SEM image showing re-adhesion of Cu film pattern after PPC decomposition.

6.6.2 Supercritical Release Approach

The second method used to release the Cu film features involved dissolving the PPC in solvent followed by supercritical drying. Samples were first immersed in agitated N-Methyl-2-Pyrrolidone (NMP) solvent for 24 hours to dissolve the PPC, followed by immersion in IPA for another 24 hours. The supercritical drying process was done using a Tousimis Autosamdri®-815B. During this process CO_2 is dissolved into the IPA bath, and the chamber conditions are ramped to exceed the fluid critical point of 1072 psi and

31°C. After reaching supercritical conditions, the chamber is vented at elevated temperature so that the fluid transitions into the gas phase and results in the release of the central Cu pad and film strip ends. The supercritical drying process averts the stiction problems that plague conventional wet release techniques, and was shown to be a reliable release process for fabrication of test specimens. A successfully released sample via supercritical dry is shown in Figure 6.12. As mentioned above, the initially curved surface above the PPC dome becomes rippled upon removal of the PPC dome due to it being a thin flexible film. However, the resulting degree of waviness is slight, as only a few ripples are formed with heights of less than 10 μm over the entire 2-4 mm span of the released structure. Also, the ripples have not been shown to be an issue for the subsequent attachment of a permanent magnet or other loading mechanism.

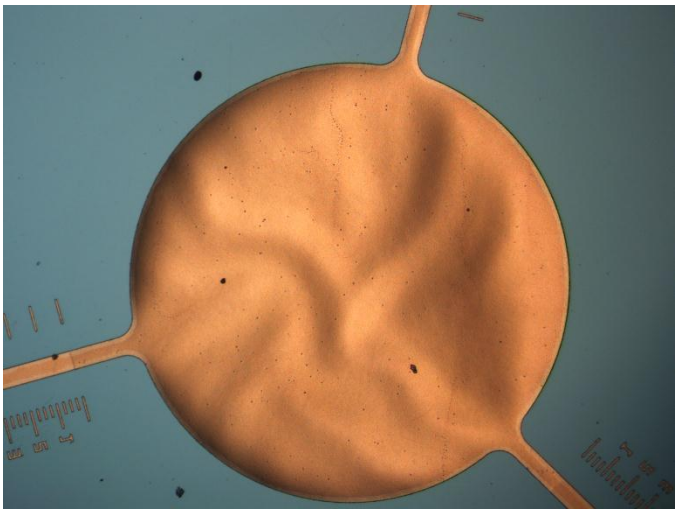

Figure 6.12. Patterned and released Cu film structure after removal of underlying PPC dome through supercritical drying.

Closer inspection of the released peel strips shown in Figure 6.13 reveal a smooth transition from the adherend to the bonded portion of the strip, and a sharp starting delamination edge. The residue visible in the SEM images is leftover from thermally decomposing the PPC; samples which were soaked in solvent and released through supercritical drying have no residue but similar overall shape.

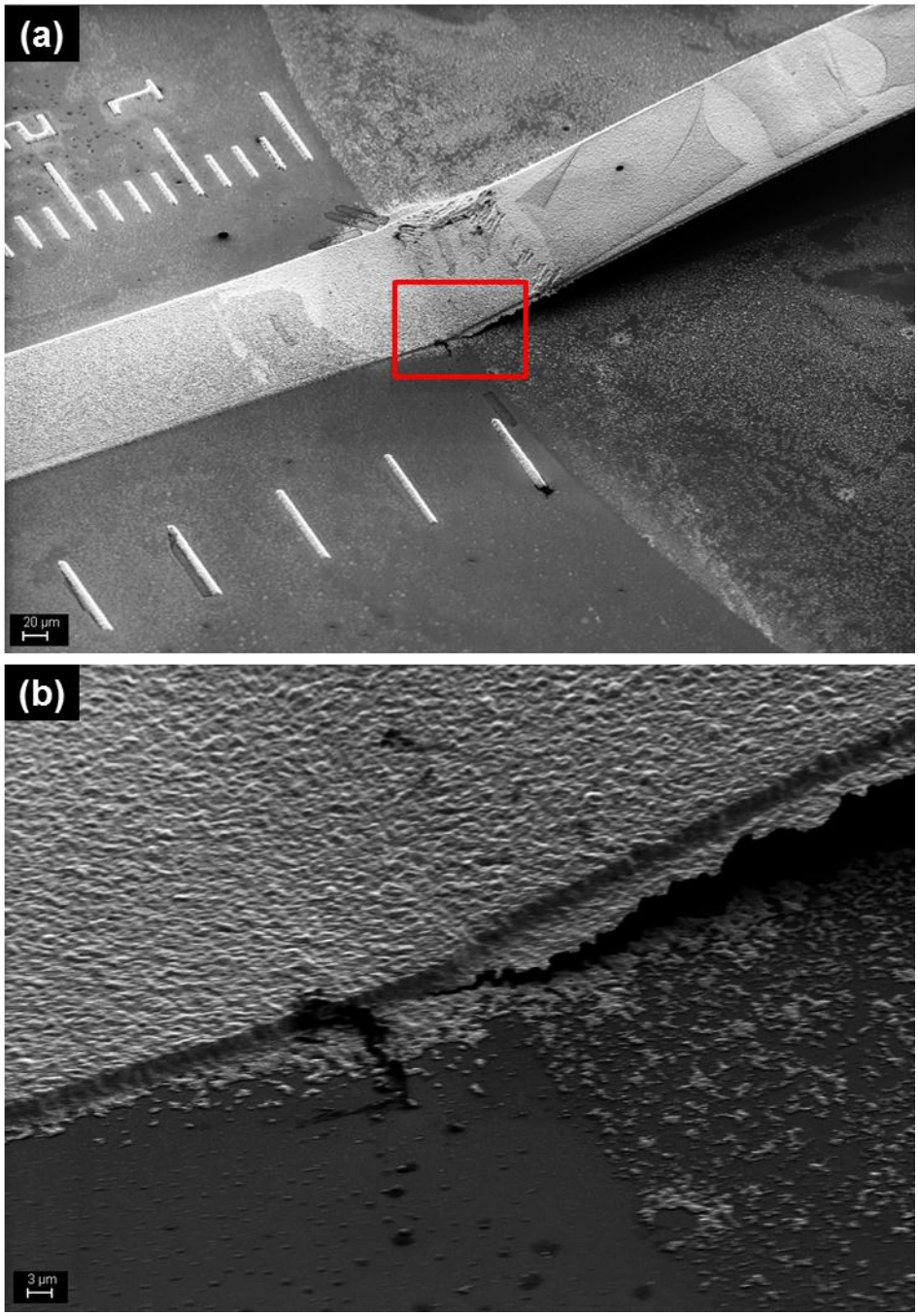

Figure 6.13. SEM images of released MAPT specimen showing (a) the base of one peel strip and (b) magnified image within the red box.

6.7 Permanent Magnet Assembly

A batch assembly process was developed in order to adhere permanent magnets onto the patterned test specimens across the wafer in parallel. After removal of the sacrificial polymer, Epibond® 7275 epoxy was first printed though a 3 mil stainless steel

stencil onto the released central copper pads using an MPM screen printer as shown in Figure 6.1g. The volume of printed epoxy is critical; too little can result in a poor bond, while too much can result in excess epoxy being squeezed out beyond the copper pad and onto the substrate. Therefore, stencil hole sizes with diameters ranging from 600 to 1500 µm were tested, where an optimized size of 660 µm resulted in the most complete bond.

A custom alignment setup was developed to precisely place a nickel-plated neodymium (NdFeB-42SH) axially-aligned magnetic cylinder (1/16”D x 1/16”H) onto the central pad as shown in Figure 6.1h. A two-part holder shown in Figure 6.14 was machined which featured an aluminum plate with an array of bored holes into which the permanent magnets are placed, and a steel backing plate which held the magnets in position through magnetic attraction and prevented them from popping out and attaching to each other.

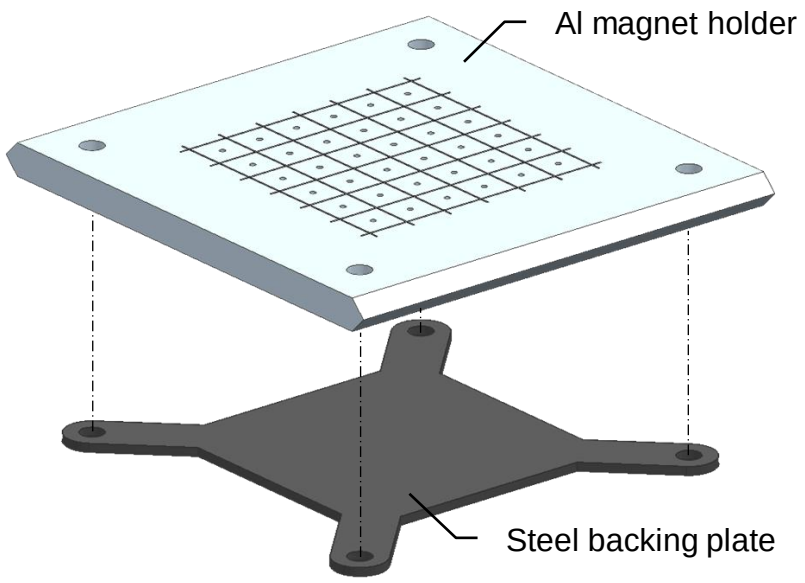

Figure 6.14. Illustration of permanent magnet holder used for batch assembly.

The assembly process is outlined in Figure 6.15. Once the permanent magnets are placed into the holder, the epoxy printed wafer is held upside-down and aligned over the magnets using a PDR XYtronic rework station (Figure 6.15a). The wafer is then brought

down to make contact with the magnets (Figure 6.15b), after which a heat lamp is placed above the sample and cures the epoxy at a measured 100ºC for 20 min. The high temperature grade neodymium showed no loss of magnetism after the cure bake. After cooling, the steel backing plate is detached from the holder (Figure 6.15c), and this allows the wafer with assembled magnets to be released from the fixture (Figure 6.15d). Finally, the wafer is cleaved into individual samples for testing (Figure 6.15e). Batch assembly of magnets is shown in Figure 6.16.

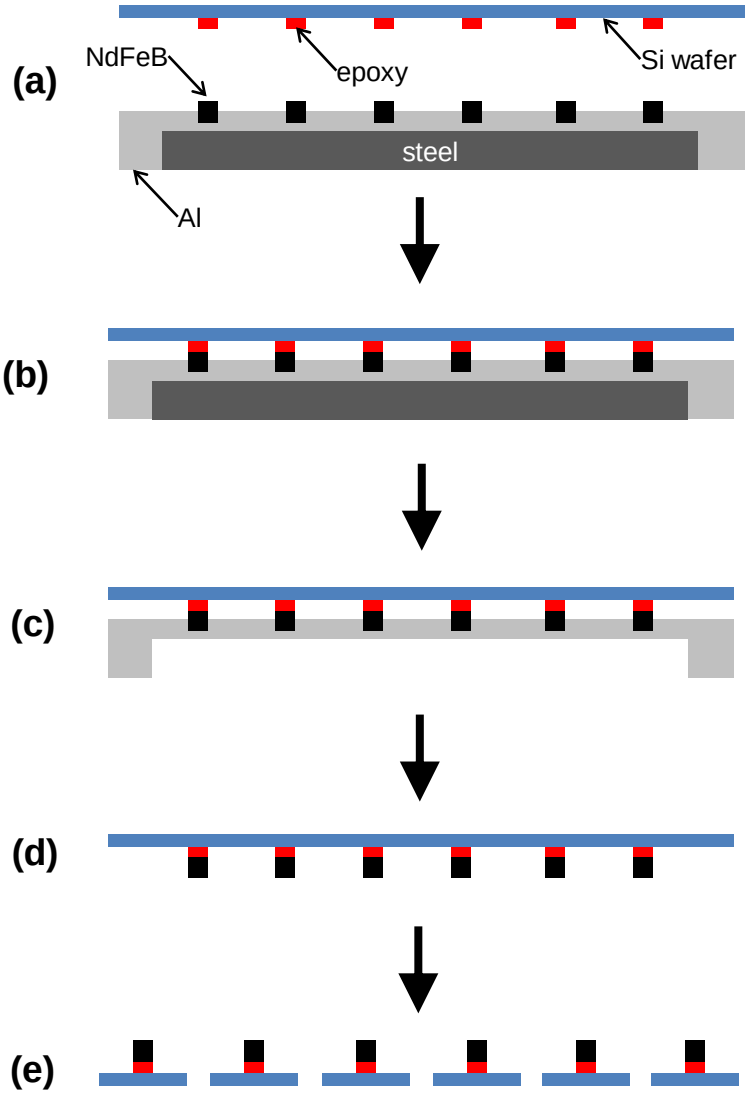

Figure 6.15. Permanent magnet assembly process.

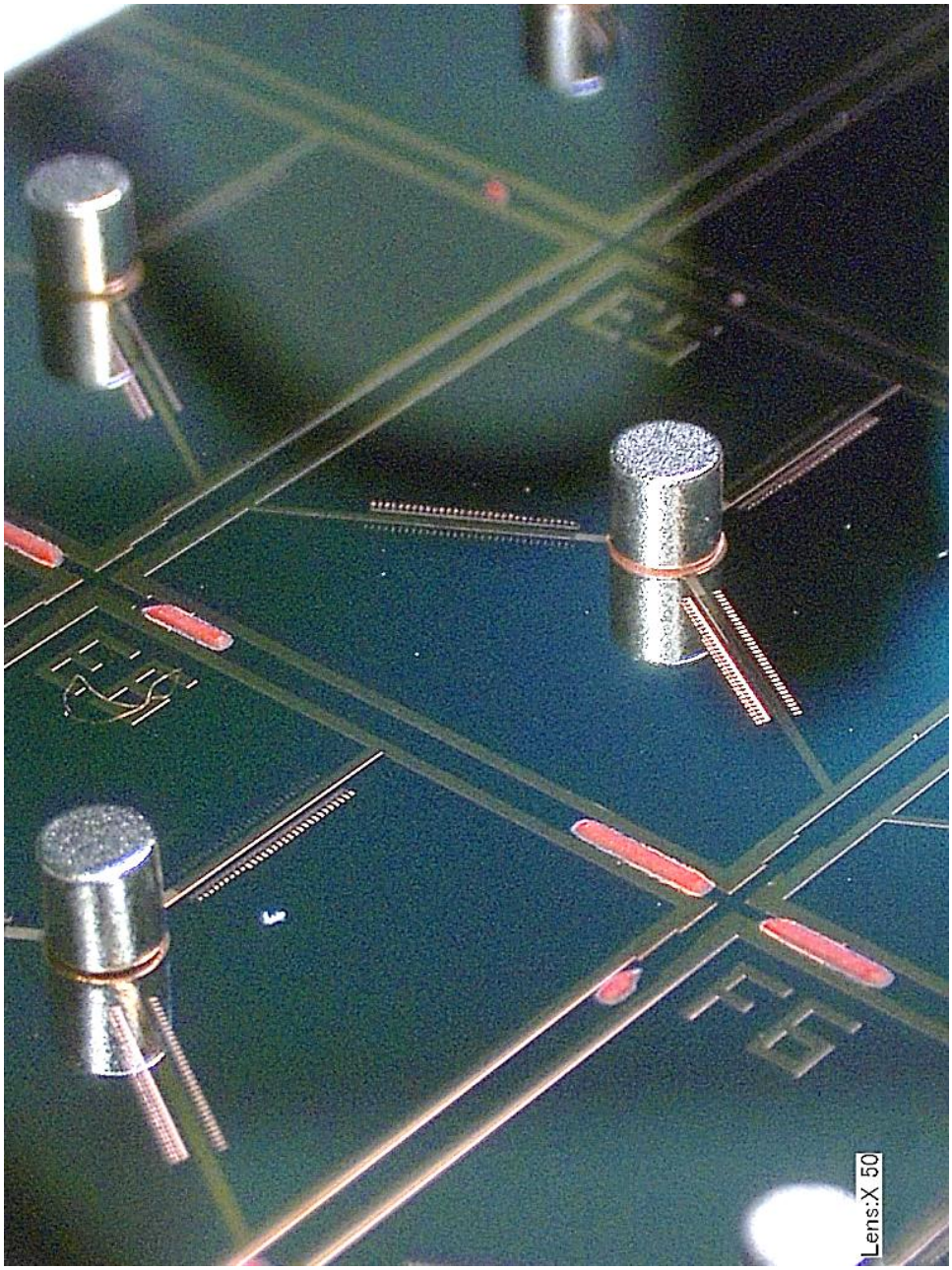

Figure 6.16. Batch assembled MAPT specimens.

In addition to the batch assembly process, permanent magnets were also assembled onto individual samples in a serial manner. In other words, the wafer was cleaved after the sacrificial release process. Epoxy was then stencil printed onto each sample separately, followed by placement onto a permanent magnet in the holder. This method resulted in more accurate assembly of the magnet onto the central pad than the batch method, due to alignment difficulties across the whole wafer. Thus, most of the

samples for which delamination results are reported in this work were assembled serially. An individual specimen is shown in Figure 6.17 where the red epoxy is visible just beyond the edge of the magnet indicating good coverage.

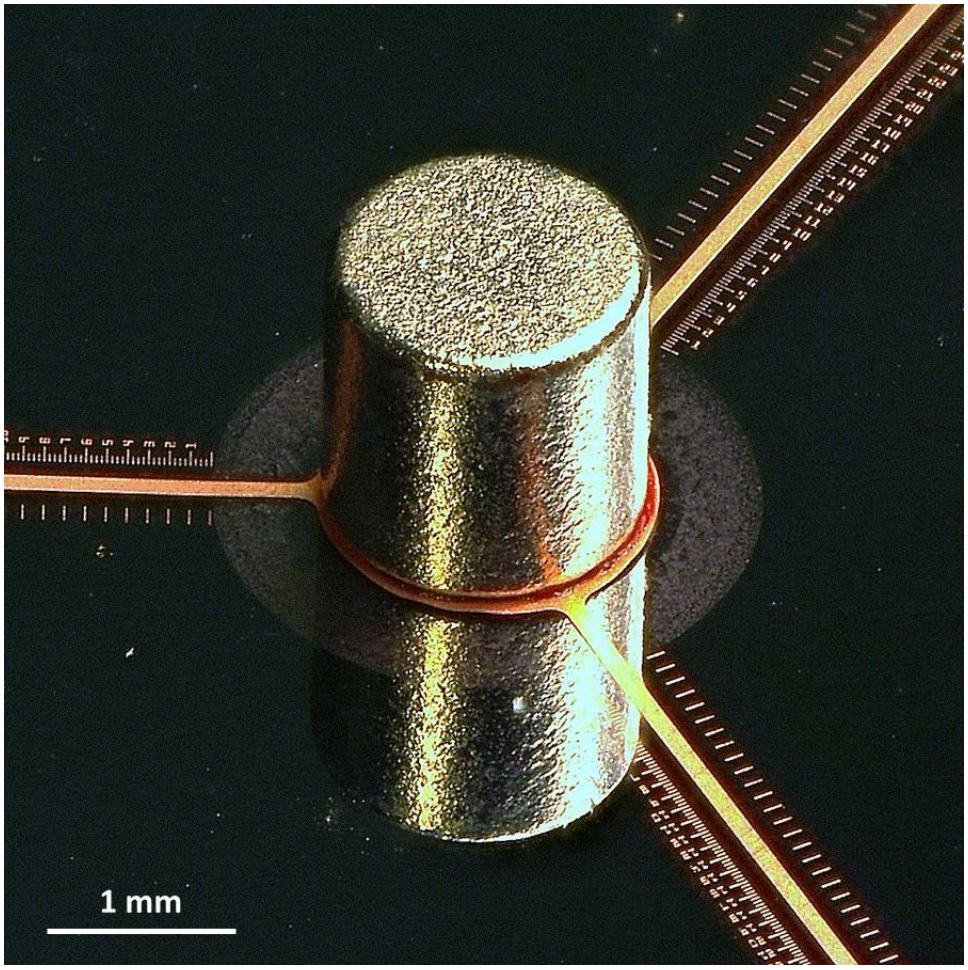

Figure 6.17. Assembled MAPT specimen. A ring of residue left after thermal decomposition of PPC is visible on the substrate. No residue is left for samples that underwent supercritical release.

CHAPTER 7

MONOTONIC PEEL TEST EXPERIMENTS

7.1 Background

Monotonic peel tests were performed on the fabricated MAPT specimens to determine the critical load at which unstable interfacial fracture occurs. Non-contact force actuation was accomplished using common low-cost analog equipment in contrast to alternative techniques which rely on fixtures and high precision mechanical actuators, such as MTS machines. Film strip deflection measurements and ultimately delamination growth were detected using high resolution optical techniques. The following sections describe in detail the calibration of the magnetic force, experimental setup and procedure, as well as a discussion of the results.

7.2 Magnetic Force Calibration

Delamination in the MAPT design is driven by the force of magnetic repulsion, and this force is characterized using the experimental setup illustrated in Figure 7.1. Here a Magnetic Sensor Systems E-66-38 tubular electromagnet is fixed at a specified distance δ from the NdFeB magnet, which is resting on a high precision scale with ~1 μN sensitivity. Accounting for the weight of the permanent magnet, the downward force is directly captured by the scale. In this setup, the two critical parameters are the separation δ and the voltage potential V applied to the electromagnet.

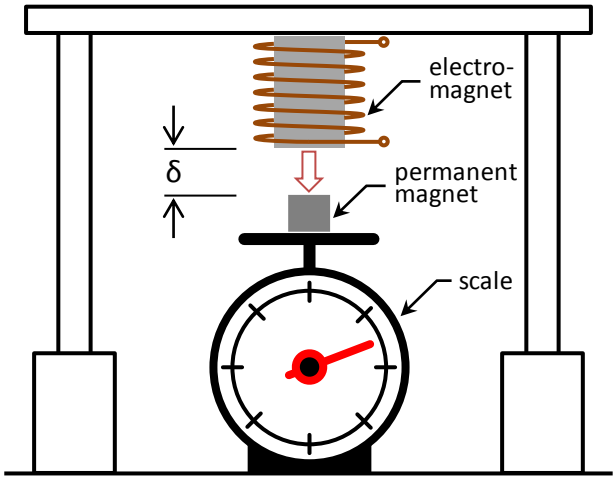

Figure 7.1. Experimental setup for magnetic force calibration.

A voltage range of 0-13 V was applied at separation distances from 1.0 to 2.2 mm as shown in Figure 7.2a, with maximum force achieved to be ~16 mN. Positive values of force indicate magnetic repulsion, whereas negative values indicate magnetic attraction. At low voltage, the ferromagnetic core of the electromagnet has a weak native polarity and is thus attracted to the permanent NdFeB magnet regardless of the direction of alignment. However, once ample current is supplied in the proper direction, the electromagnet will have a stable opposing polarity and repel the NdFeB magnet when at sufficiently large separation distances. It was interesting to observe that at very close distances the magnets would experience a net attractive force even at high voltage levels. This occurs because of the size effects of the magnetic field interaction between the small NdFeB magnet and the larger electromagnet.

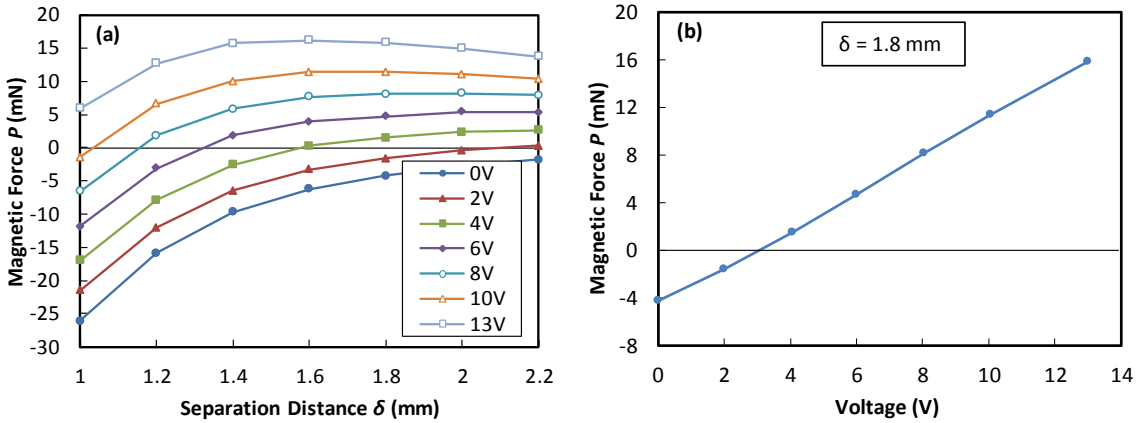

Figure 7.2. (a) Typical force vs. magnet separation gap δ for varying applied voltage to the electromagnet. (b) Typical force vs. electromagnet voltage at fixed δ = 1.8 mm.

The separation gap is fixed during the peel test, and δ = 1.8 mm was chosen as an optimized distance due to high force potential, large operable voltage range, and low sensitivity to variations in the gap distance. At this distance, the magnetic force was found to be a linear function of *V*, transitioning from magnetic attraction to repulsion at ~3 V (see Figure 7.2b). Each MAPT specimen magnet was calibrated individually in this manner with near identical results. For the peel test, the actual gap between the permanent magnet and electromagnet is $\delta+\Delta$, where Δ is the vertical displacement of the central Cu pad. However, the magnitude of Δ was at most a few hundred microns in the experiments, and so remained within the calibration's range of accuracy.

7.3 Experimental Procedure

During the peel test, an electromagnet of opposing magnetic alignment is placed underneath the MAPT specimen such that actuation is a result of a repulsive magnetic force as shown in Figure 7.3. Monotonic peel test experiments were conducted while a Veeco Wyko® NT-2000 optical profiler was used to measure the sample surface topography *in situ*. The voltage applied to the electromagnet was slowly ramped in discrete increments, and then held constant momentarily while the optical profiler imaged the sample surface, thus capturing the deflection of the film and delamination propagation over a range of applied forces.

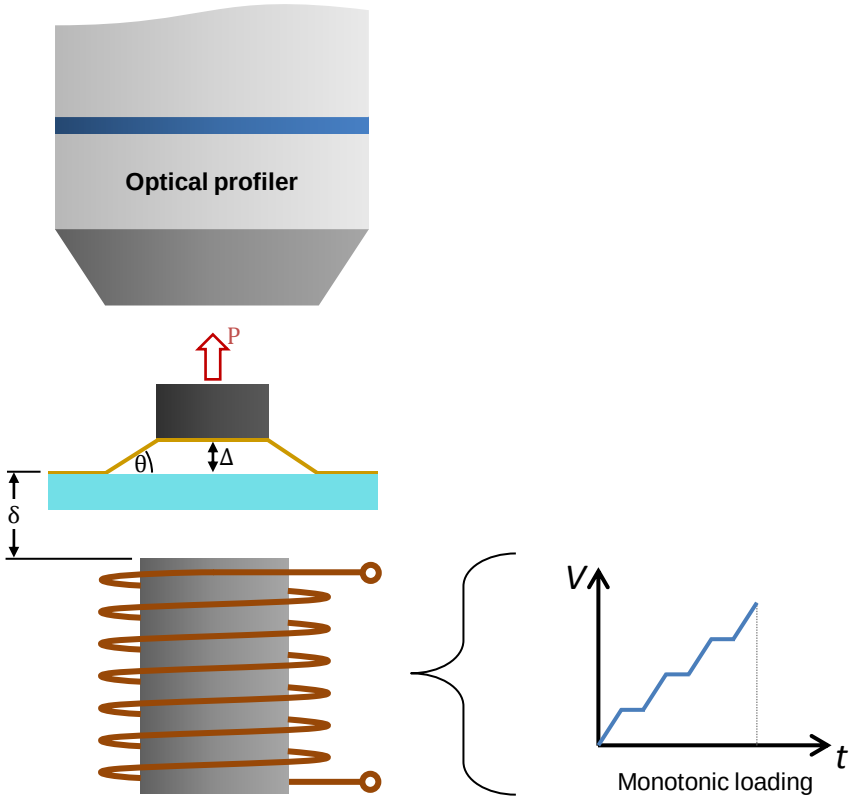

Figure 7.3. MAPT setup for monotonic peel test experiment. The voltage was applied in a series of ramps followed by a short dwell during which the optical profiler scanned the displaced film strips.

Photographs of the test specimen in the loaded and unloaded state are shown in Figure 7.4. The resulting vertical translation of the magnet is stable under load and promotes even stretching of the three anchoring peel strips. Also, the permanent magnet assembly process resulted in accurate placement with strong and uniform adhesion to the central pad. Shown in Figure 7.5 are example profiler images from one test specimen taken at significant points during the delamination test. At 3.0 V the sample experiences essentially no force and is in the initial at rest state. At 6.0 V the strips are raised and pulled taught but no significant delamination is observed. At 7.0 V some incremental delamination is first observed and then slowly propagates until 9.1 V, after which steady state delamination results in total failure of the peel test.

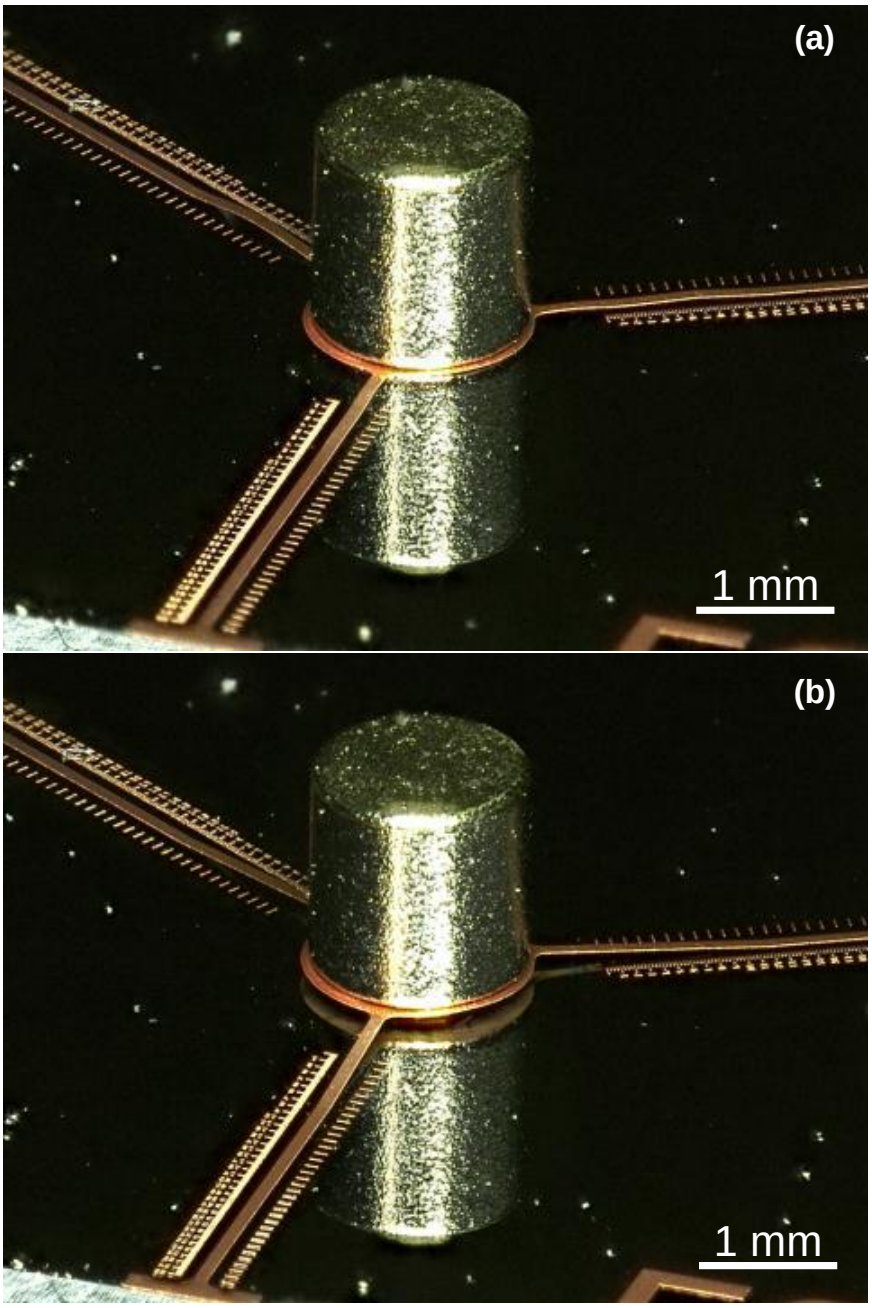

Figure 7.4. MAPT specimen (a) at rest with no applied force and (b) with permanent magnet elevated due to repulsion from driving electromagnet below, and imposing peel forces along the three anchoring strips.

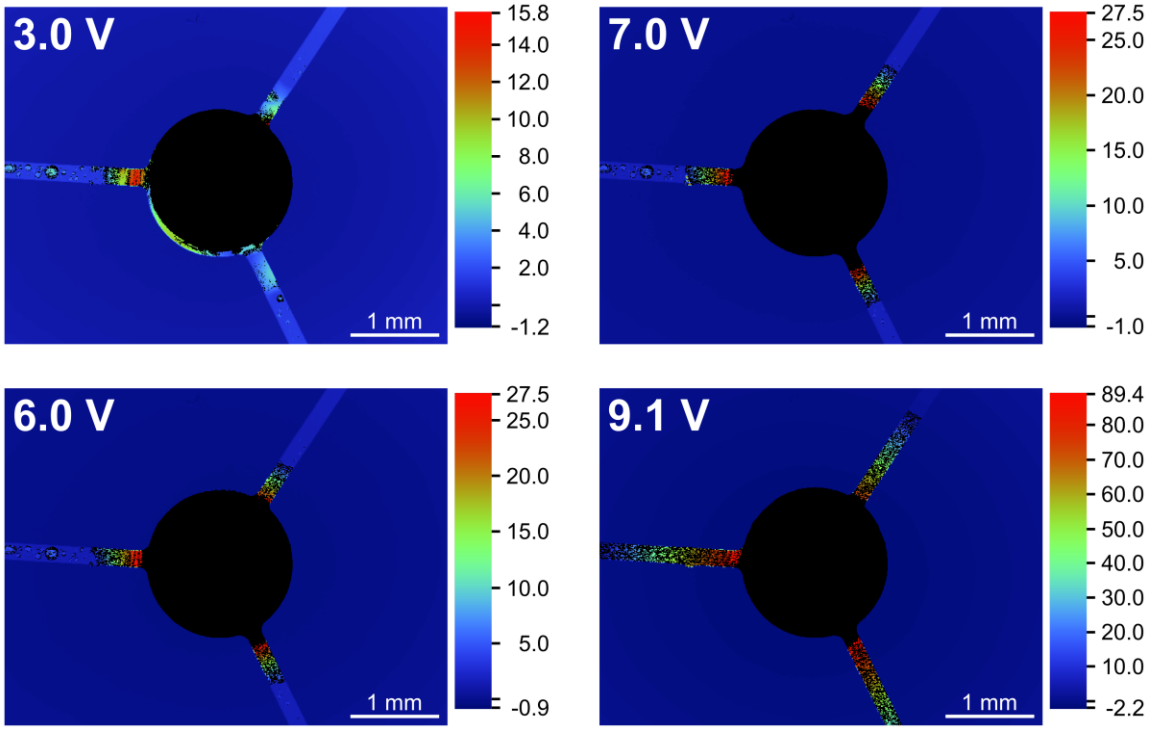

Figure 7.5. Optical profiler images at select intermittent applied voltage during delamination test. Black color indicates areas that are missing out-of-plane height data. Delamination is first observed at 7.0 V and propagates until 9.1 V, after which steady-state peeling commenced.

Throughout these images, black pixels indicate that no height data was registered in that location. Since the profiler was set to only scan near the substrate surface, the top of the permanent magnet was well out of range and thus generates the central black circle in its place. Black spots are also dispersed along the film strips as well. This is due to the fact some of the downward light is reflected off the shiny copper film at an angle rather than back up straight into the detector.

The slope of each peel strip along with the location of the crack front was determined from each of the profiler images, as shown in Figure 7.6. Thus, along with the previous force calibration results, measurements of the interfacial crack length and peel angle were obtained as a function of the applied magnetic force.

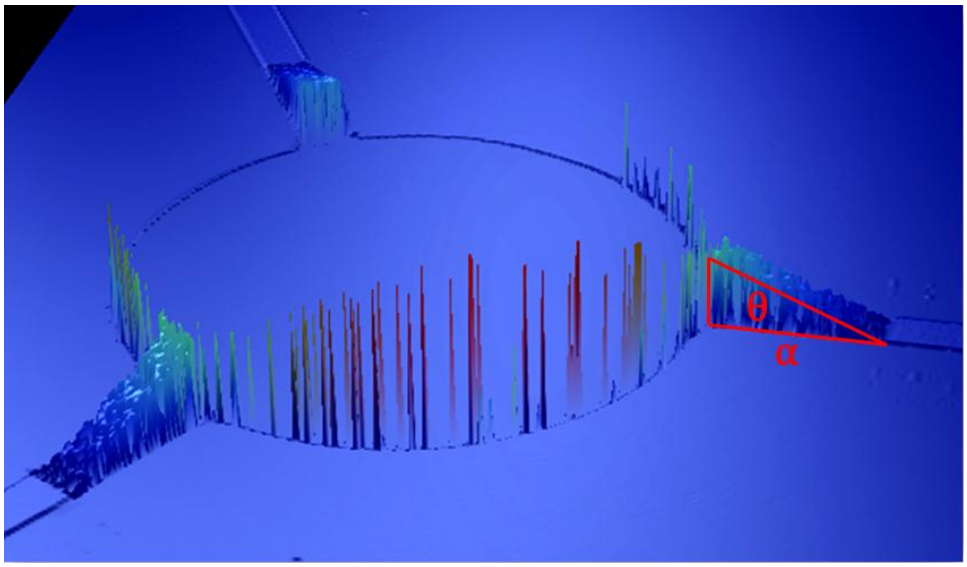

Figure 7.6. 3D view generated by optical profiler. A linear fit of the peel strip height data allows for measurement of the peel angle θ and delaminated strip length α.

Each MAPT specimen provides displacement data for three peel strips simultaneously. Assuming evenly distributed force amongst the three strips, the critical peel force and associated peel angle are determined once delamination of at least one peel strip reaches steady-state. In all specimens tested, at least two (if not all three) of the strips totally peeled off upon reaching steady-state delamination, while the remaining strip was cohesively fractured before peeling (see Figure 7.7). Since no images could be taken during the dynamic peeling process, it is assumed that any incrementally higher force beyond the last stable deflection measurement would induce steady state delamination. Consequently, the highest sustained peel force is reported here as a conservative estimate for the critical peel force.

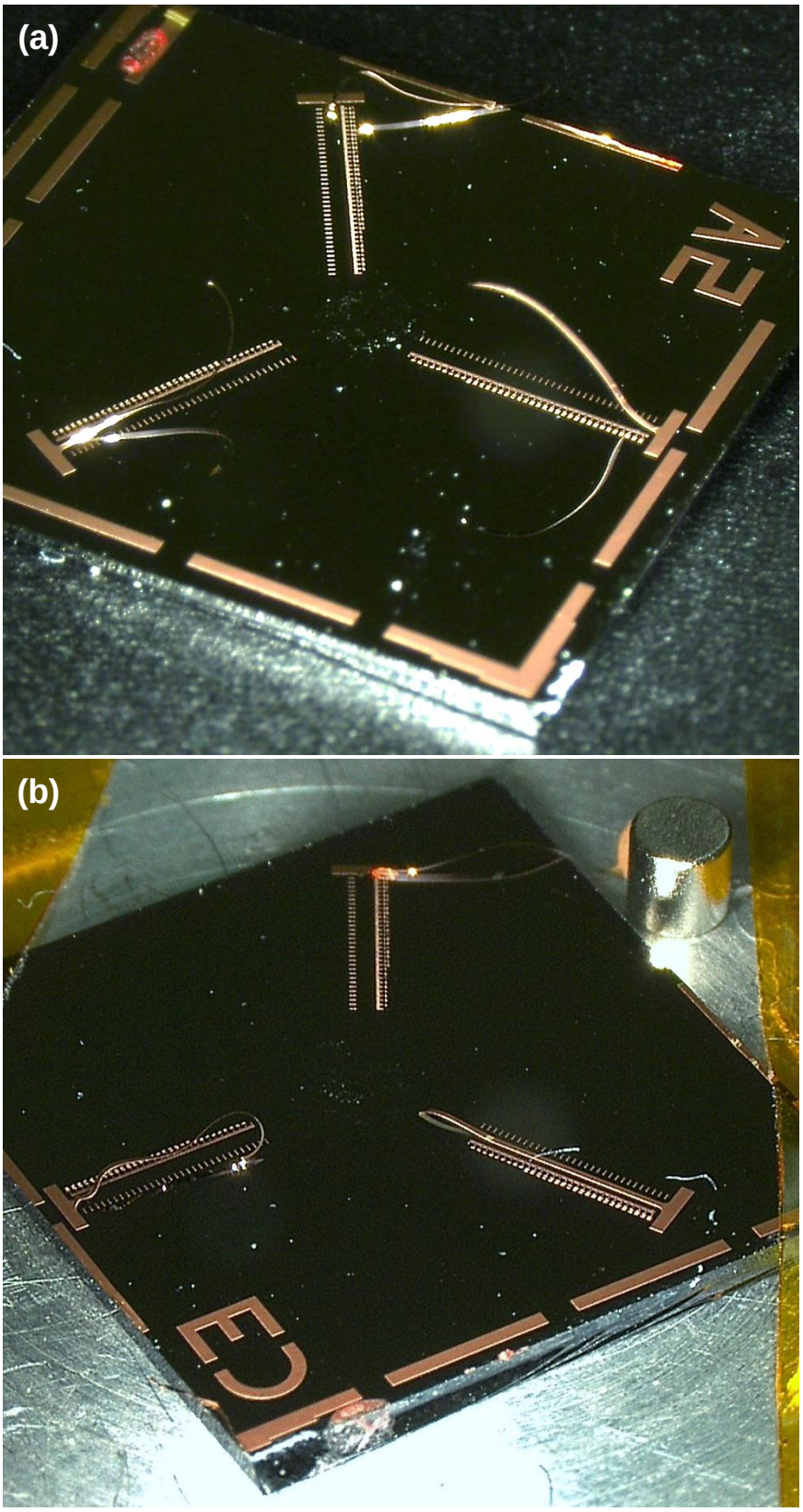

Figure 7.7. Delaminated MAPT specimens where (a) all three strips reached steady-state peeling and (b) two strips were peeled. The strips are cohesively fractured where the permanent magnet and attached central pad was torn off at the conclusion of the test.

while the remaining five specimens were released through supercritical drying and were thus not heat treated.

7.4 Results

Processing of the optical profiler images resulted in the typical peel angle vs. magnetic force relationship shown in Figure 7.8a. There was no observed trend indicating whether the strip with higher or lower peel angle would delaminate first, thus the average peel angle at a given voltage was used to estimate the peel force and applied energy release rate. In most cases, steady-state peeling was reached immediately following delamination initiation. However in two of the samples (one heat-treated and the other not), incremental and unstable crack growth was observed during ramping of the applied force until steady-state peeling was reached at the critical load (Figure 7.8b).

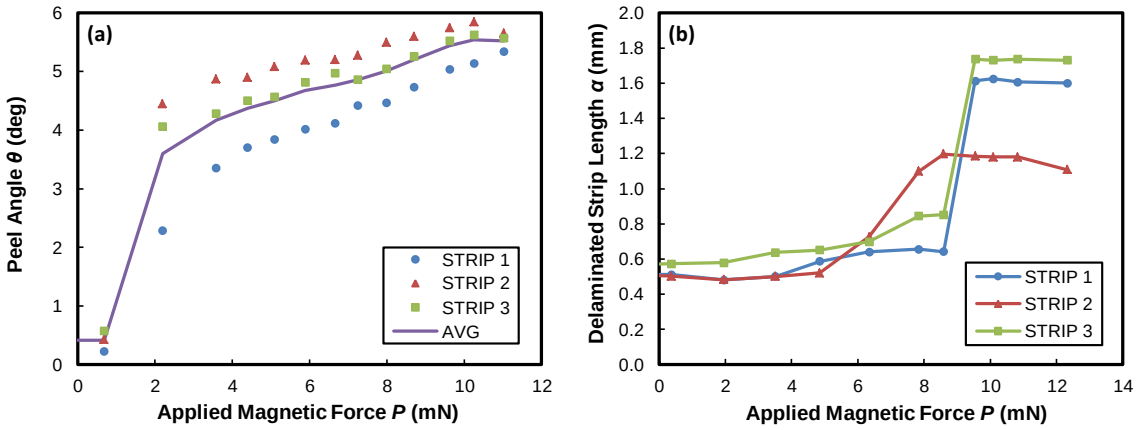

Figure 7.8. (a) Peel angle and (b) delamination length as a function of magnetic force.

The results of the MAPT experiments are summarized in Table 7.1. In order to appropriately compare peel strips of varying dimensions, the magnetic pull-off force and tangential peel force are expressed per strip cross section as P/bh and $\sigma=F/bh$, respectively. The critical ERR and FER were calculated using a uniform tension model as described in 0.

Table 7.1. MAPT results for electroplated Cu on natively oxidized Si substrate.

Sample number	Cu strip thickness h (μm)	Cu strip width b (μm)	Pull-off force P_c/bh (μN/μm^2)	Average peel angle θ_{avg} (deg)	Average peel stress σ_{avg} (MPa)	G_c (J/m^2)*	Γ_0 (J/m^2)*
Heat treated at 250°C							
1	1.7	100	33	4.1	154	0.8	0.8
2	1.7	200	36	3.8	184	0.9	0.9
Not heat treated							
3	1.5	100	47	4.0	229	1.4	1.2
4	1.5	100	53	5.5	187	1.6	1.5
5	1.5	100	74	5.5	255	2.5	2.3
6	1.6	75	55	4.8	218	1.6	1.5
7	1.6	100	43	4.2	175	1.0	0.9

Note: *calculated using uniform tension assumption.

7.5 Discussion

The critical ERR of the heated samples was 0.8-0.9 J/m^2, whereas the non-heat-treated samples exhibited slightly higher values of 1.2-2.2 J/m^2. If instead the Cu film is assumed to be linear elastic with a modulus of 110 GPa, the reported interfacial fracture energy rate would increase by ~10-20%. These values are in line with the literature, of which a range of ~1-10 J/m^2 has been published for ~1 μm Cu on SiO_2 [72, 73]. While this trend may not be statistically significant due to the limited sample size, we suspect that several factors may contribute to the decreased interfacial strength of the heated samples, such as damage due to thermal expansion mismatch and Cu film grain coarsening. While it is suspected that thermal expansion mismatch and Cu film grain coarsening is causing damage at the interface, the conclusive reasoning for this weakened interface, including the testing of a larger sample set, is beyond the scope of this work.

CHAPTER 8

FATIGUE PEEL TEST EXPERIMENTS

8.1 Background

Current experimental test techniques are mainly suited to characterize thin film interfacial fracture toughness under monotonic loading. In other words, these techniques determine the critical load at which fracture occurs, however they are generally ill-suited to provide rapid and precise cyclic loading for a fatigue crack propagation (FCP) study. Consequently, there is a general lack of data in the literature concerning interfacial delamination under cyclic fatigue loading for virtually all thin film material systems.

Relatively few studies have experimentally characterized interfacial FCP under constant stress amplitude loading, namely for metal-ceramic [28, 74-79], ceramic-ceramic [32], polymer-metal [80-82], and polymer-glass [83] interfaces. Only a handful of these report delamination growth rates for systems involving thin films with thickness less than 10 μm [28, 32, 77, 79, 81]. This lack of available data is partly due to the reliance of these studies on sandwich-type test specimens, such as the double cantilever beam (DCB), double cleavage drilled compressive (DCBC), compact tension (CT), and four-point bend (FPB) tests. The fabrication of these sandwich specimens, in which macroscale supporting substrates are bonded together by the thin films of interest, often involve unusual processes which result in non-representative films and interfaces. After bonding, specimens may then require precision cutting or drilling into the samples in order to initiate the crack, and/or have difficulty in controlling the crack propagation along the desired interface.

An alternative to the sandwich-style test is the peel test and its similar variations, which operate by stretching a partially detached film at an angle from the adhered substrate until the film delaminates. Although this test technique has been successfully used to characterize the critical interfacial fracture strength for many material systems,

very few have reported testing films with thickness less than 10 μm due to complications with specimen handling and applying peel forces through mechanical fixtures [84]. These peel tests are generally performed using displacement controlled actuators, which pull on the film at a constant rate while measuring the reaction force. Consequently, any FCP study to date that has utilized a peel-type test has been conducted under constant displacement amplitude loading and for films with thickness greater than several tens of microns [85, 86].

The MAPT approach was specifically designed for the dual purpose of characterizing both monotonic and fatigue delamination which addresses the limitations of other test techniques. Of particular interest is the ability to observe the interfacial fatigue response under load-controlled conditions such that the crack tip loading amplitude can be related to the pace of crack growth, and thus provide the empirical data necessary for device lifetime predictions. The focus of this work is therefore to perform an interfacial FCP study using the MAPT technique, which is believed to be a first for a peel-type test under constant stress amplitude loading.

8.2 Approach

The MAPT design is ideally suited to conduct interfacial crack propagation experiments under fatigue loading in addition to the monotonic tests described in Chapter 7. A subcritical cyclic load can also be applied simply by supplying an AC current to the electromagnet. The amplitude and frequency of the applied force is thus a direct function of the input signal to the electromagnet. As the area above the specimen is free of obstruction, photographs of the test sample can be taken intermittently to capture the delamination propagation. Therefore, the crack growth rate can be observed as a function of the loading amplitude, from which Paris Law parameters can be determined. In this work, a FCP study was conducted for MAPT specimens featuring electroplated copper films on a silicon wafer under constant subcritical amplitude loading.

8.3 Experiment Design

The experimental setup for MAPT specimens subjected to cyclic fatigue loading is shown in Figure 8.1 and Figure 8.2. The test specimen is first placed onto a stand, and then moved into alignment with the electromagnet below. The outer edges of the specimen substrate are taped to the stand to keep it stationary during loading. An optical microscope is positioned above the test specimen, and was used to capture the cyclic displacement and delamination propagation of the film strips. All objects in the near vicinity of the test specimen, such as the stand and microscope, do not contain magnetic materials and thus did not affect the applied magnetic force.

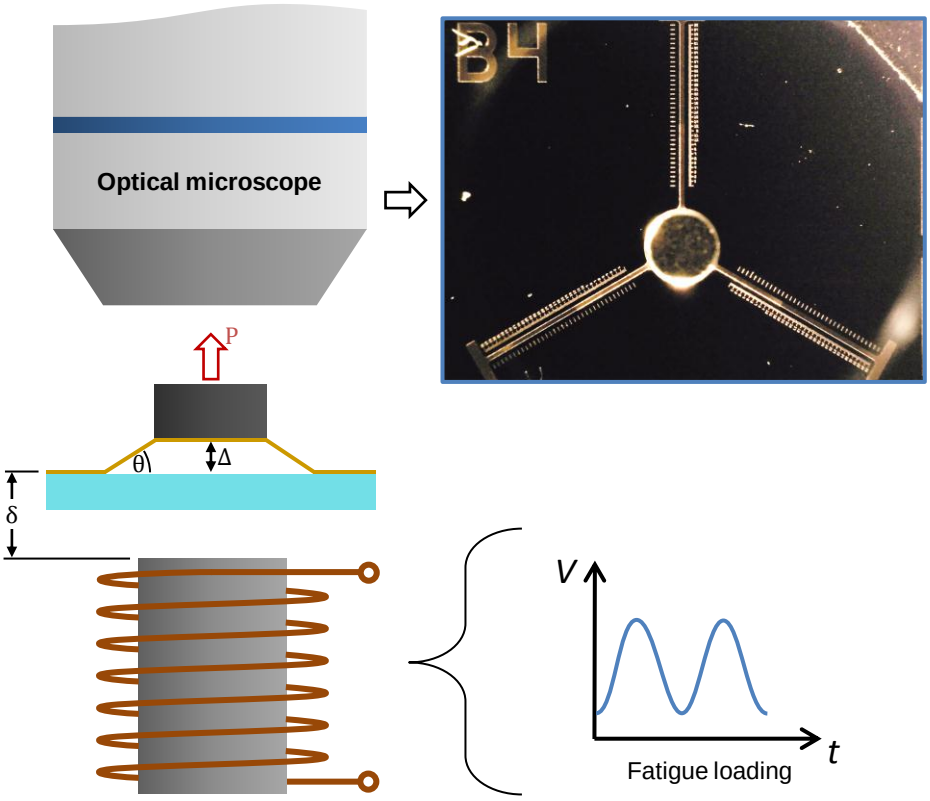

Figure 8.1. MAPT setup for fatigue delamination propagation experiment.

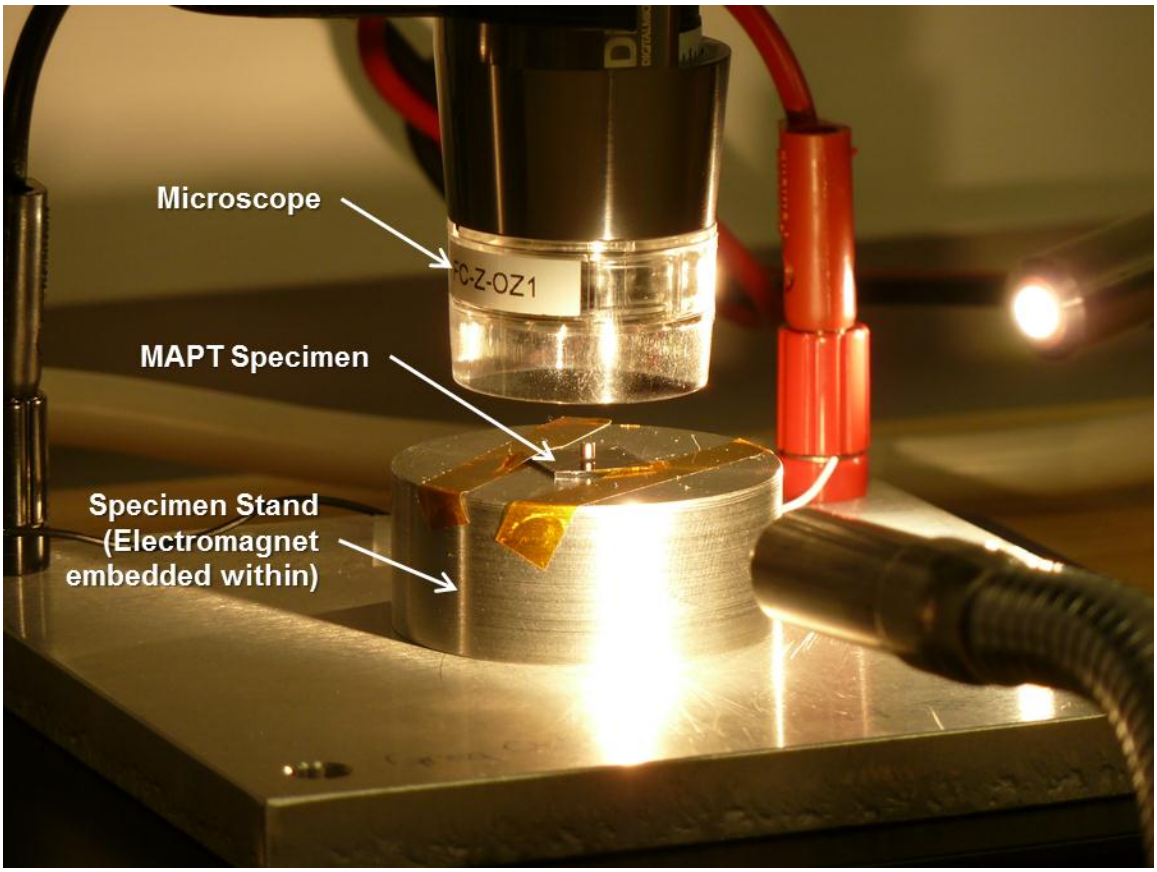

Figure 8.2. Photograph of experimental setup.

A sharp crack tip is inherently present between the peel strip and substrate upon fabrication of the test specimen. Therefore, moderate crack propagation that results from cyclic subcritical loading is considered Stage-II crack growth. The rate of crack growth in this regime under constant amplitude loading is determined experimentally, and can commonly be empirically fit using the Paris Law, where C and m are constants.

It is well known that the loading ratio R can significantly affect the crack growth rate. Since the MAPT design does not allow for negative vertical displacement (i.e. the released film structure cannot penetrate the substrate), the available range of stress ratios are $R \geq 0$. In this work, crack propagation was studied under $R = 0$ fatigue loading by ensuring the permanent magnet and attached central pad make contact with the substrate at the bottom of the loading cycle (i.e. at V_{min}).

8.3.1 Application of Cyclic Loading

In order to minimize the dynamic kinetic effects of cyclic loading, the electromagnet was driven by a voltage sine wave from V_{min} to V_{max} at 500 mHz; a frequency slow enough to not interfere with the natural frequency of the samples and also be considered electrically DC, yet fast enough to apply several thousand cycles per hour. The voltage sine wave was output from a function generator; however this signal needed to be passed through an amplifier in order to have sufficient power to drive the electromagnet. A non-inverting operational amplifier circuit was therefore constructed with a maximum output of ±20 V as shown in Figure 8.3. In this setup, the amplification magnitude is governed by

$$V_{out} = V_{in}\left(1 + \frac{R_2}{R_1}\right). \tag{9.2}$$

where V_{out} is the output voltage, V_{in} is the input voltage, and R_1 and R_2 are resistors in the circuit. Appropriate resistor values were chosen to achieve the necessary gain.

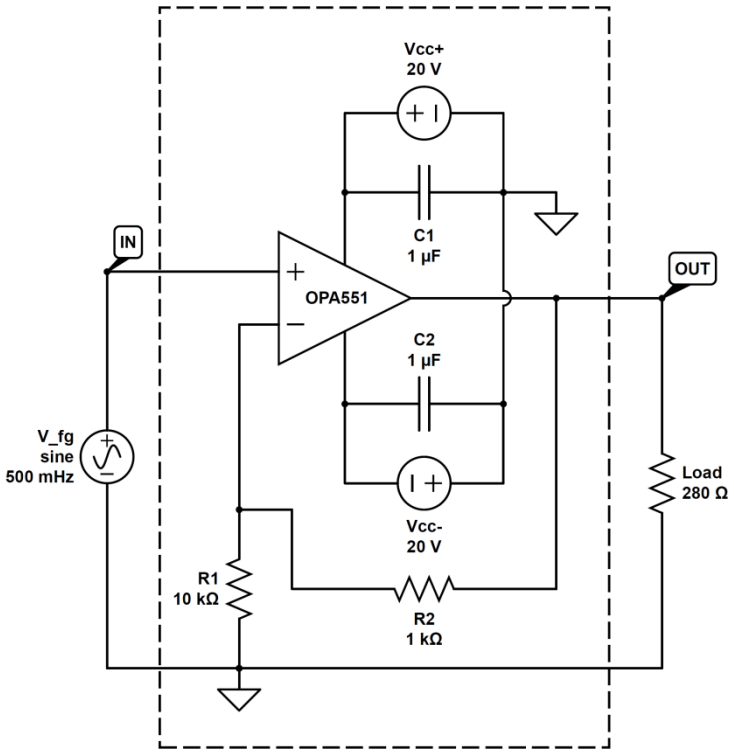

Figure 8.3. Non-inverting op-amp circuit used to drive the electromagnet. A voltage sine wave from a function generator is input into the amplifier, and the output signal is applied to the electromagnet load. Capacitors are used to remove signal noise.

A force calibration was performed under monotonic loading conditions as reported in Chapter 7, which resulted in positive repulsive force when the voltage applied to the electromagnet was greater than 2.7 V for an initial magnet separation gap δ of 1.8 mm. The magnetic force was shown to be insensitive to the gap distance for this configuration, as the permanent magnet can displace several hundred microns away from the substrate and the calibration is still valid. The magnetic field strength (and thus the total magnetic force) generated by the driving electromagnet when the voltage reaches V_{max} during cycling is assumed to be equivalent to the case where the voltage is held constant at V_{max}. In the fatigue experiments, V_{min} was chosen to be 1.8 V such that the sample would touch the substrate ensuring $R = 0$ loading condition, and the maximum force at V_{max} was derived from the monotonic calibration results. Fatigue cycling tests were conducted for loading amplitudes $\Delta P/bh$ ranging from 31.8 to 43.8 µN/µm^2.

8.3.2 Experimental Procedure

Fatigue testing was performed in a laboratory environment at 22°C and 50% relative humidity. MAPT specimens were subjected to a series of constant amplitude loading blocks of $N \approx 15{,}000$ - 125,000 cycles each, depending on the resulting delamination rate. The rate of delamination propagation da/dN within each loading block was captured using time-lapse photography, where the optical microscope captured photographs of the specimen intermittently every few minutes. With proper in-plane lighting, the location of the peeling edge of each strip was determined from these images as shown in Figure 8.4, and thus provided a means to monitor the crack propagation over time. Visible hash marks which run alongside the peel strips were also incorporated into the mask design, and are a convenient reference to determine the delamination front position through visual inspection. The rate of delamination was determined to be in the range of 0 nm/cycle to about 100 nm/cycle, depending on the loading amplitude.

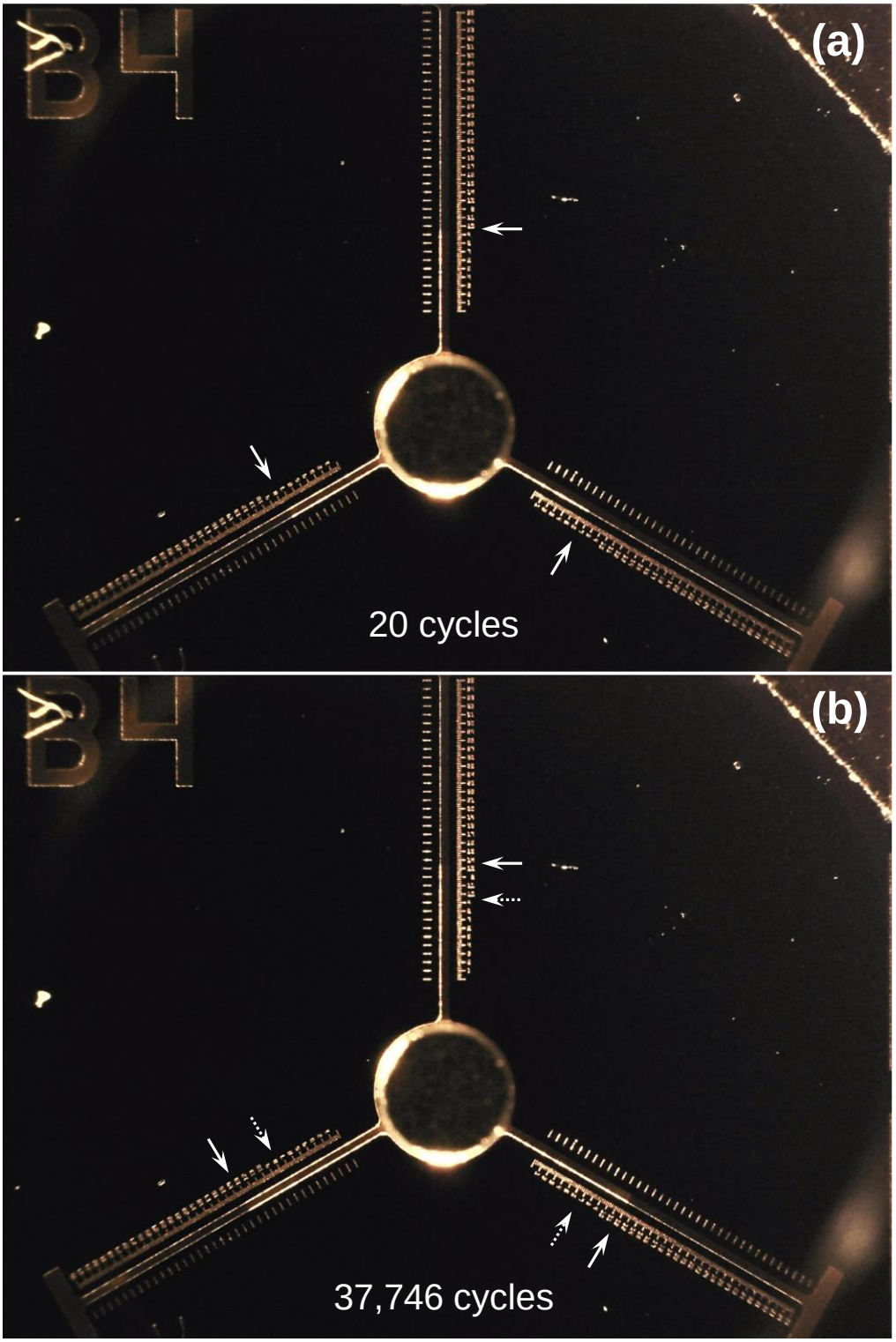

Figure 8.4. MAPT specimen undergoing fatigue cycling from 1.80 - 6.99 V after (a) 20 cycles and (b) 37,746 cycles. Solid arrows indicate current delamination front position, with dashed arrows in (b) indicating the delamination at the start of fatigue cycling.

8.4 Results

The delamination of each strip was tracked individually, and typical delamination progression results are shown in Figure 8.5 over a range of loading amplitudes. No crack propagation was observed for $\Delta P/bh \leq 31.8$ μN/μm^2 ($\Delta G \leq 0.78$ J/m^2) for as long as 125,000 cycles, so this is considered to be roughly the endurance limit. When the loading amplitude $\Delta P/bh$ was greater than 37 μN/μm^2, the delamination rate for the three strips was observed to be typically consistent and uniform. However, some variability in peeling behavior amongst the strips was observed for lower loading amplitudes.

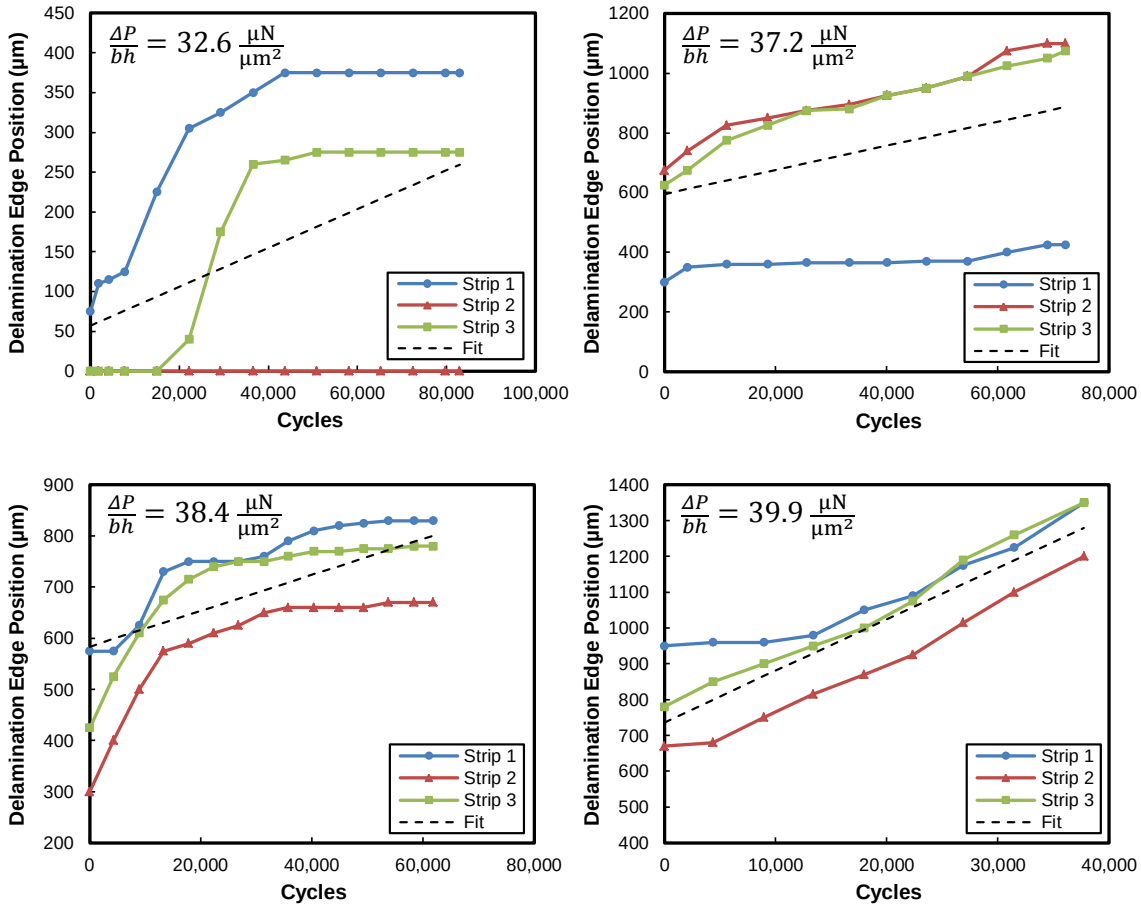

Figure 8.5. Delamination propagation at various loading amplitudes (R = 0). The dashed line represents the average linear fit amongst the three strips for a given loading block.

An average delamination rate within each loading block was determined from the slope of a linear fit of the cumulative crack propagation data. This averaged crack growth rate is shown in log-scale relative to the applied ΔG in Figure 8.6. A Paris Law

fit of the delamination rates results in constants $C \approx 3 \cdot 10^{-9}$ and $m \approx 15$, and has good correlation with the experimental data. Monotonic testing results for identical samples as discussed in Chapter 7 are also shown and indicate the range of critical loading amplitudes for steady-state peeling.

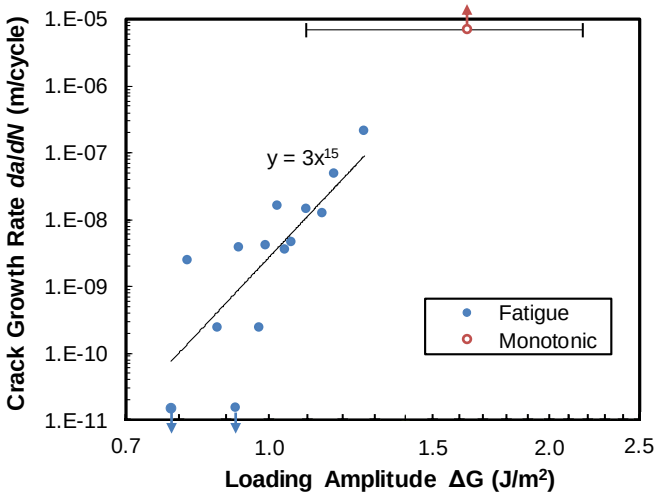

Figure 8.6. Delamination propagation of 1.6 µm electroplated Cu on Si with overlaid Paris Law fit. Average critical loading amplitude with error bar is shown from monotonic fracture test results.

8.5 Discussion

The overall trend observed for delamination growth rate is consistent with typical fatigue crack behavior; a threshold level for crack advance followed by a Paris regime for propagation and finally unstable growth near the critical limit. Since a sharp crack tip is inherently present between the peel strip and substrate upon fabrication of the test specimen, the resulting crack propagation from cyclic subcritical loading is considered Stage-II crack growth.

For larger loading amplitudes, each of the three strips behaved similarly with relatively constant delamination growth rates. However, at lesser amplitudes, there is increased scatter in the crack growth rate, with appreciable deviation in fatigue behavior between the three strips. In such cases, the delamination progressed with varying speed, often with one or more strips experiencing temporary crack arrest or not delaminating at

all. This pronounced variability under low amplitude fatigue loading may be attributable to the thin membrane effect, where the out-of-plane deformation is very sensitive to small forces until the film is sufficiently stretched. Additionally, there may be inherent variability due to the scale effect in thin film peeling, as discontinuous peeling behavior has been reported for <10 μm thick copper films [63, 84].

This work is believed to be the first to report delamination propagation rate as a function of constant amplitude fatigue loading using a peel test configuration. For 1.6 μm thick Cu films on a Si substrate, interfacial fatigue crack propagation was observed for a minimum applied ERR amplitude that was about half the critical value required for steady-state peeling. Intermediate loading amplitudes resulted in a Paris Law regime with relatively predictable delamination rates.

CHAPTER 9

MATERIAL CHARACTERIZATION OF COPPER THIN FILM

9.1 Background

Calculations of interfacial fracture strength are dependent on the material properties of the film and substrate. Under brittle fracture, the elastic modulus and Poisson's ratio are sufficient material parameters. However, in cases of ductile fracture, the plastic hardening behavior of the materials must be characterized as well. For the MAPT specimens in this work, the Si substrate is brittle and its elastic properties have been thoroughly characterized in the literature. Therefore, the focus of this chapter is on characterizing the elastic-plastic properties of the fabricated Cu thin film through analysis of the MAPT experimental data as well as through other techniques.

Material behavior of metal films is strongly influenced by factors such as film thickness, manufacturing process, fabrication parameters, environmental exposure, microstructure, etc. Therefore, a vast range of material properties can be found in the literature for copper thin films as shown in Table 9.1. Here, the experimental tensile test data was fit with the general elastic-plastic power-law hardening model

$$\varepsilon = \frac{\sigma}{E} + \left(\frac{\sigma}{K}\right)^{1/n}, \tag{9.1}$$

where K is the hardening modulus and n is the hardening exponent.

Table 9.1. Cu film elastic-plastic properties

Thickness (μm)	Type	E (GPa)	σ_y* (MPa)	n	K (MPa)	Ref.**
	bulk	110-128		0.44		
12.00	electroplated (DC)	85	235	0.10	440	[87]
15.00	electroplated (DC)	72	360	0.09	668	[88]
18.00	electroplated (DC)	102	150	0.09	275	[89]
53.00	electroplated (DC)	76	205	0.16	546	CINDAS
71.00	electroplated (DC)	91	250	0.16	680	CINDAS
18.00	electroplated (pulsed)	73	137	0.11	262	[89]
0.27	evaporated	102	885	0.04	1144	[90]
0.30	evaporated	93	520	0.29	3175	CINDAS
0.45	evaporated	102	675	0.07	1047	[90]
0.95	evaporated	102	500	0.08	850	[90]
2.00	evaporated	110	345	0.24	1490	[61]
2.03	evaporated	102	360	0.11	731	[90]
2.78	evaporated	102	325	0.13	713	[90]
36.00	wrought foil	78	105	0.10	212	CINDAS

** determined using 0.2% offset; elastic limit may be considerably less.*
*** CINDAS indicates properties were published in the database with no particular reference cited.*

9.2 Modulus

The elastic modulus of films can be determined experimentally using a nanoindenter. Here, an indenter tip is pressed into the film, and the initial elastic rebound is captured upon removal of the tip. A Hysitron TriboIndenter was used to measure the elastic modulus of the fabricated copper films. About 30 separate indentations were performed with depths ranging from 63 to 333 nm. Accounting for the effect of both the substrate and indenting tip, the deduced modulus of the copper film ranged from about 112 to 147 GPa, with an averaged value of about 126 GPa. This is within expected values of bulk copper albeit slightly higher than what is reported in Table 9.1 for thin films.

9.3 Plastic Hardening

MAPT specimens feature peel strips that undergo predominantly tensile forces like the analogous pull-off test specimens as shown in Figure 9.1. As the applied force

increases, the strips become more stretched and as a result the peel angle increases. Therefore, assuming uniform tension in the strip, the stress and strain in the film at any given point during the peel test can be calculated from the applied force and the deformed film geometry.

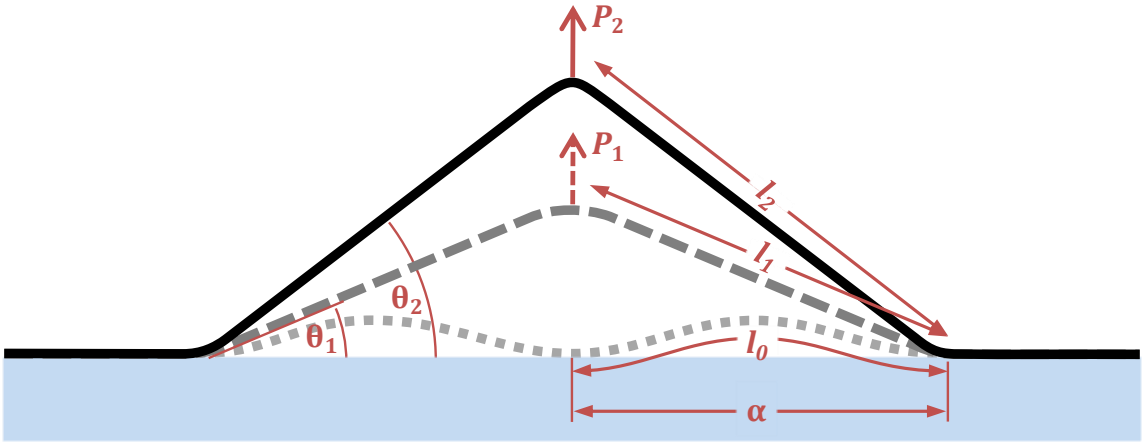

Figure 9.1. Illustration of peel strip deformation due to tensile forces. Two strips are shown in the figure, whereas three symmetric strips are considered for strain calculations from MAPT displacement data.

The tensile strain of the stretched peel strips must be calculated relative to their initial unstressed length, l_0. However, as discussed in Chapter 6, the patterned film strips do not lie flat on the substrate but rather are slightly wavy after they are released. This makes it difficult to determine their initial relaxed serpentine length directly. However, once sufficient magnetic force P_1 is applied to lift the permanent, the three anchoring strips become taut and assume the average peel angle θ_1. The resulting stress in the strip can then be calculated from force balance using

$$\sigma_1 = \frac{P_1}{3bh\sin\theta_1}. \tag{9.2}$$

If σ_1 is about equal to (or less than) the yield stress σ_y, then the corresponding strain ε_1 can be approximated using

$$\varepsilon_1 = \frac{\sigma_1}{E}, \tag{9.3}$$

where the elastic modulus E can be determined through other means (e.g. nano-indentation). Once the force is increased to P_2, the stress σ_2 can be again calculated similarly from force balance. The strain ε_2 can be calculated by solving the system

$$\begin{cases} l_1 = \dfrac{\alpha}{\cos\theta_1} = (1+\varepsilon_1)l_0 & (9.4) \\ l_2 = \dfrac{\alpha}{\cos\theta_2} = (1+\varepsilon_2)l_0 & (9.5) \end{cases}$$

which results in

$$\varepsilon_2 = (1+\varepsilon_1)\frac{\cos\theta_1}{\cos\theta_2} - 1. \tag{9.6}$$

In this manner, the film strip position at force P_1 serves as a reference for calculating the strain for all subsequently applied forces. Therefore, the tensile stress of the MAPT film strips at any applied force P_n is

$$\sigma_n = \frac{P_n}{3bh\sin\theta_n}, \tag{9.7}$$

and the strain is

$$\varepsilon_n = \begin{cases} \dfrac{\sigma_1}{E}, & \text{if } n = 1 \\ \left(1+\dfrac{\sigma_1}{E}\right)\dfrac{\cos\theta_1}{\cos\theta_n} - 1, & \text{if } n > 1 \end{cases} \tag{9.8}$$

where $n = 1$ is the moment at which the film strips first become taut.

The calculations above depend on the assumptions that the applied force is purely vertical and the three film strips displace symmetrically. Therefore, average peel angles amongst the three peel strips were used in Equations 9.7 and 9.8 to calculate the tensile stress and strain for various applied loads. Assuming the elastic modulus was 126 GPa, the resulting stress-strain points for the monotonically loaded samples is shown in Figure 9.2. The power law fit with hardening constants K = 1490 MPa and n = 0.3 most closely resembles the values obtained from [61] in Table 9.1.

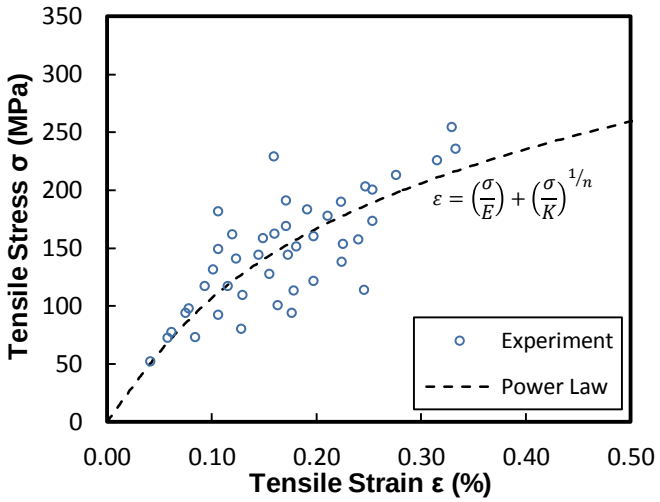

Figure 9.2. Tensile stress-strain data from MAPT peel test specimens with overlaid power-law hardening fit with constants *E* = 126 GPa, *K* = 1490 MPa, *n* = 0.3.

In an ideal tensile test, the base of the film strips would have good adhesion and therefore have a constant initial length. Since the MAPT strips in this work experienced some incremental delamination, it is additionally assumed that the newly peeled portions of the strip had the same uniform tension as the full released strip. Also due to the weak interface, the strips delaminated before undergoing large strain (> 0.3%). Thus, additional data is needed to determine the hardening behavior over the full plastic range.

9.4 Residual Stress

Residual stress in the copper films was deduced from the change in the substrate curvature before and after film deposition. For an elastic system, and uniform film thickness much less than the substrate thickness, the stress in the film can be calculated using Stoney's equation:

$$\sigma_f = \frac{1}{6}\left(\frac{1}{R_0} - \frac{1}{R_1}\right)\frac{E_s t_s^2}{(1-\nu_s)t_f}, \tag{9.9}$$

where the subscripts *f* and *s* refer to film and substrate, respectively, *t* is thickness, *v* is Poisson's ration, and R_0 and R_1 are the radii of curvature of the plate before and after film

deposition, respectively. Curvature was measured using a BowOptic 208 along three different planar axes 120° apart, with the average curvature used for stress measurement.

Four test wafers (about 550 μm thick) were processed for copper film stress measurement purposes in parallel with the MAPT specimens using the same fabrication parameters. Curvature measurements before and after sputtering 500 nm of copper resulted in stress of 197 ± 9 MPa in the sputtered copper film. The stress in the subsequently electroplated 1-1.2 μm copper was 24 ± 8 MPa, based on the incremental change in curvature after electrodeposition and assuming the elastic modulus of the substrate remained unchanged after it was sputter-coated.

Wafer curvature measurements confirm that the majority of the peeling film is low-stress electroplated copper. Analytical and finite element models in this work therefore assume no residual stress in the copper film. Still, the effect of residual stress and film non-uniformity due to multilayer deposition is of interest; however quantifying these effects on interfacial fracture characterization is beyond the scope of this work.

9.5 Microstructure

A cursory investigation of the copper film microstructure was conducted by taking high resolution images of the patterned strip with an SEM. Shown in Figure 9.3 are images of the copper strip, where the sidewall has been exposed to etchant during patterning. A relative difference in the microstructure is apparent between the bottom portion of the film which was sputtered-deposited and the greater top portion which was electroplated. The sputtered copper appears pitted and amorphous, while the electroplated copper appears faceted. This suggests that the electroplating process produced much larger grain size than sputtering, as has been commonly been observed elsewhere (e.g. [91]).

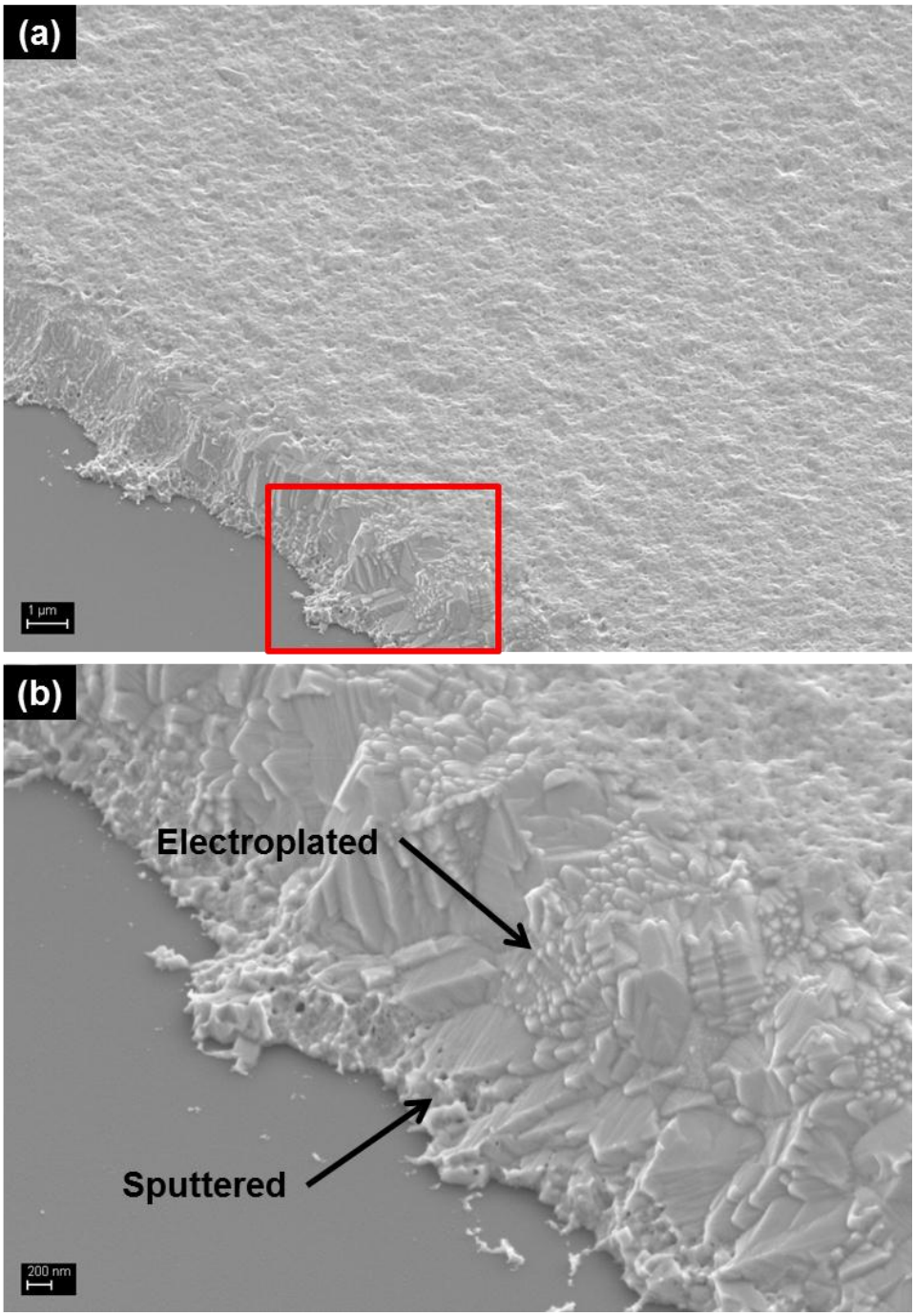

Figure 9.3. SEM images of patterned Cu film at various magnifications. The red box in (a) indicates the location zoomed to create the image in (b).

Additional work is required in order to quantify the texture and grain composition of these copper films, perhaps through the use of a focused ion beam (FIB) or atomic force microscopy (AFM). Furthermore, grain sizes can change over time as a function of the storage time, film thickness, and heat treatment. Thus, the ability to relate the

microstructure to the resulting interfacial fracture parameters would be a valuable contribution, but is beyond the scope of this research.

CHAPTER 10

FINITE ELEMENT PEEL MODEL

The finite element method is a powerful numerical tool for modeling fracture processes, as it has the ability to model the mechanics of cracked bodies for which closed form solutions are not obtainable or are too complex for practical use. Described in the following sections are details of the finite element model developed to simulate peeling of the MAPT specimen, as well as some of the numerical schemes that can be used to characterize the interfacial fracture parameters.

10.1 Established Fracture Characterization Methods

10.1.1 Two-Step Crack Extension

The two-step crack extension (CE) method involves comparing two independent models: one with crack length a, and the other with crack length $a+\delta a$. The FER can then be computed using

$$\Gamma = -\frac{(U_{a+\delta a} - U_a) - P(\Delta_{a+\delta a} - \Delta_a)}{b\delta a}, \tag{10.1}$$

where U is the combined elastic and plastic strain energy, P is the applied load, and Δ is the displacement in the direction of the load at the point it is applied. Similarly, the ERR can be calculated by only considering the elastic strain energy. Although the CE method is appropriate for elastic systems, it fails to capture the accumulation of plastic work as the crack grows over the length δa, and therefore can result in an overestimate of the FER.

10.1.2 Virtual Crack Closure

The virtual crack closure technique (VCCT) [92] involves calculating the work required to close a crack by one element length δa. The FER is calculated using

$$\Gamma_I = \frac{1}{2} F_{y1} \frac{(v_2 - v_3)}{b\delta a}, \tag{10.2}$$

$$\Gamma_{II} = \frac{1}{2} F_{x1} \frac{(u_2 - u_3)}{b\delta a}, \tag{10.3}$$

$$\Gamma = \Gamma_I + \Gamma_{II}, \tag{10.4}$$

where F is the nodal force, b is the width, u and v are the nodal displacements in X and Y, respectively, and the subscripts correspond to the node numbers as shown in Figure 10.1. This method requires only one model and can potentially determine the mode mix directly from the separate mode I and II contributions to Γ. However, for interfacial cracks, the Γ_I/Γ_{II} ratio as determined through VCCT has been shown to be a function of element size and thus may not be a reliable method to calculate the mode mix [93]. Moreover, crack tip plasticity can potentially distort the calculated FER since the work of closure is assumed to be a linear elastic process.

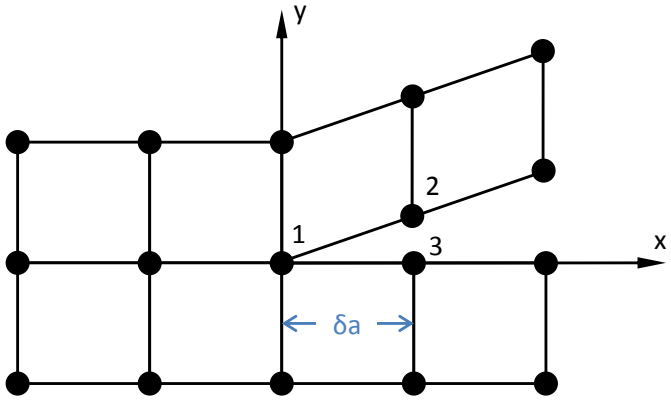

Figure 10.1. Schematic for VCCT.

10.2 Sequential Crack Extension

A new finite element approach was pursued for calculating fracture parameters for a dynamic ductile fracture process. The proposed method is similar to the CE method except that instead of comparing two separate models with different crack lengths, only one model is used in which the crack is systematically propagated. Thus, the new method is referred here as Sequential Crack Extension (SCE), and involves sequentially decoupling the nodes ahead of the crack tip, one pair of nodes at a time, and computing the change in external and internal energy terms for every increment of crack growth.

For analysis of thin film interfacial delamination, the interface between the film and substrate is represented as a set of coupled nodes as shown in Figure 10.2. Under remotely applied loading, the crack is manually advanced by one element every load step by decoupling the nodes at the crack tip. The change in external work, elastic strain energy, and plastic work are then calculated until the incrementally calculated energy terms reach a steady-state value. Unlike conventional CE, this method preserves the plastic work accumulated along the debonding surfaces as the crack propagates.

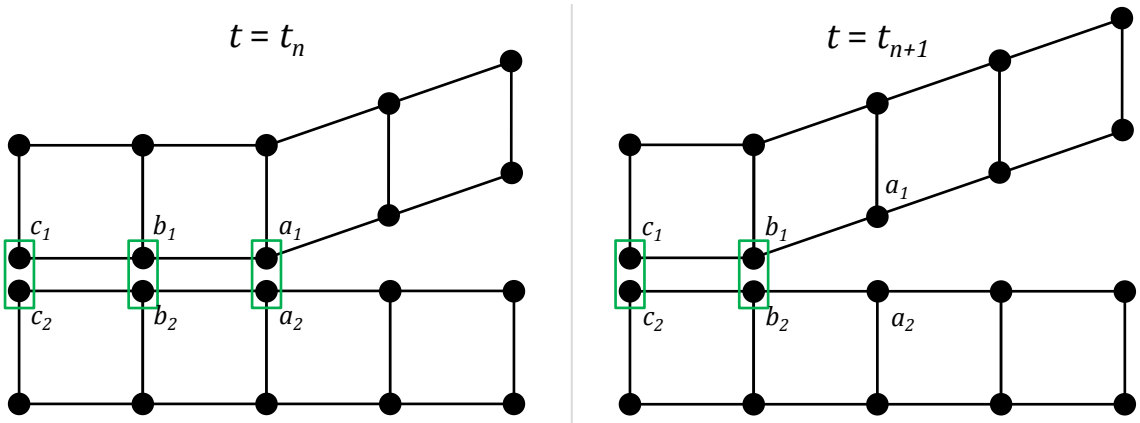

Figure 10.2. Schematic for sequential crack extension. Nodes within green box are coupled.

10.3 Geometric Model

10.3.1 Analysis Domain and Boundary Conditions

A base 2D finite element model of one example MAPT peel strip was developed using ANSYS® 13, from which the CE, VCCT, J-Integral, and SCE methods were applied and compared. As shown in Figure 10.3, a thin ductile film strip with nominal thickness h_{nom} = 1 μm is modeled over an elastic substrate. A vertical force of $P/3bh$ (one-third of the total vertical force) is applied at the free end of the film, which is also constrained to only vertical translation ($u_x = 0$) as this is where it would normally be joined to the permanent magnet. The initially released strip length has a nominal length α_{nom} = 250 μm. The peel strip dimensions are such that b>>h, and so plane strain conditions were imposed.

In later analysis, it was found that the substrate had a negligible impact on the calculated fracture parameters. Thus, in an effort to reduce computation time, the film strip was also modeled alone, with fixed displacement constraints at the interface in lieu of coupling with a substrate below. These boundary conditions are more analogous to the analytically derived fracture parameters, which assume a flexible film on a rigid substrate.

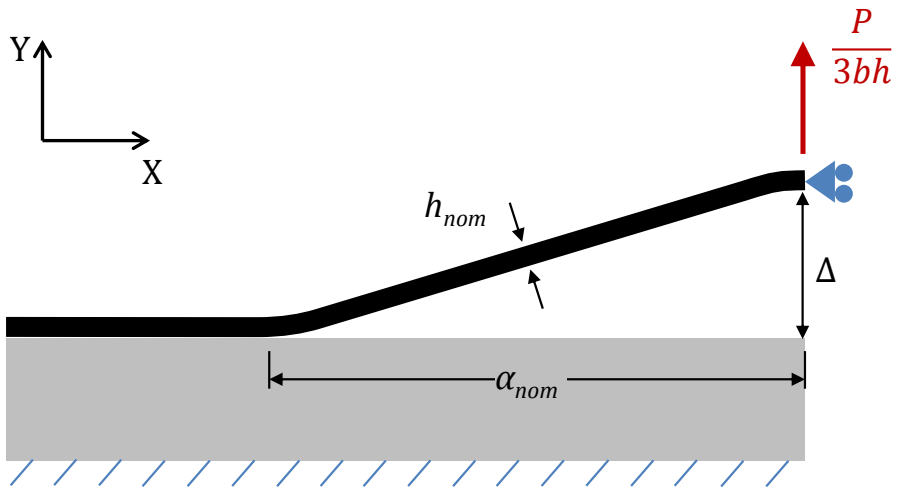

Figure 10.3. Domain for 2D plane-strain analysis of MAPT film strip peeling under constant applied load.

10.3.2 Material Models

A nonlinear film material was used which was based on the experimental characterization of Cu films by Henning [61]. Here, a multi-linear isotropic hardening constitutive model was used which was defined by E = 110 GPa, v = 0.34, K = 1490 MPa, and n = 0.24, where E is the elastic modulus, v is the Poisson's ratio, K is the hardening modulus, and n is the hardening exponent, respectively. For instances where it was used, the substrate was modeled as linear elastic Si with E = 190 GPa and v = 0.25.

10.3.3 Finite Element Mesh

The finite element mesh consisted of 2D linear quadrilateral elements (PLANE182). A mapped meshing scheme was employed in which the mesh density was significantly increased in the region around the crack tip as shown in Figure 10.4. In order to perform a mesh convergence study, several meshes were generated where the element size near the interface was reduced from 50 to 5 nm. Initially, the entire interface along which the crack propagates was refined to the same element size. However, as the crack propagates only one element increment at a time, this strategy

resulted in a very time intensive solution for a highly refined mesh, especially for crack propagation > 10 µm.

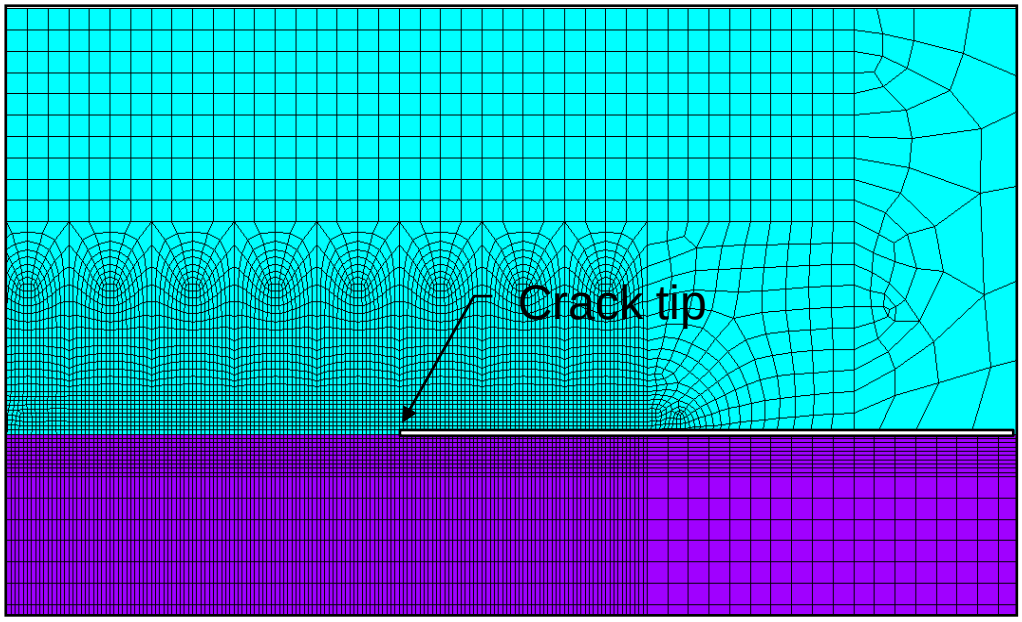

Figure 10.4. Analysis domain and example finite element mesh.

A revised meshing strategy was therefore pursued for a more efficient finite element simulation. As shown in Figure 10.5, the element density at the interface is progressively increased ahead of the initial crack tip. This allows the crack to initially grow at a reasonable rate through a relatively course mesh until reaching steady state behavior, and then transition into a series of locally refined regions to assess convergence. For this model, the element size at the interface ahead of the initial crack tip is 50 nm for a distance of 20 µm, then is progressively reduced to 25 nm, 10 nm, and 5 nm for a distance of 1 µm each, respectively.

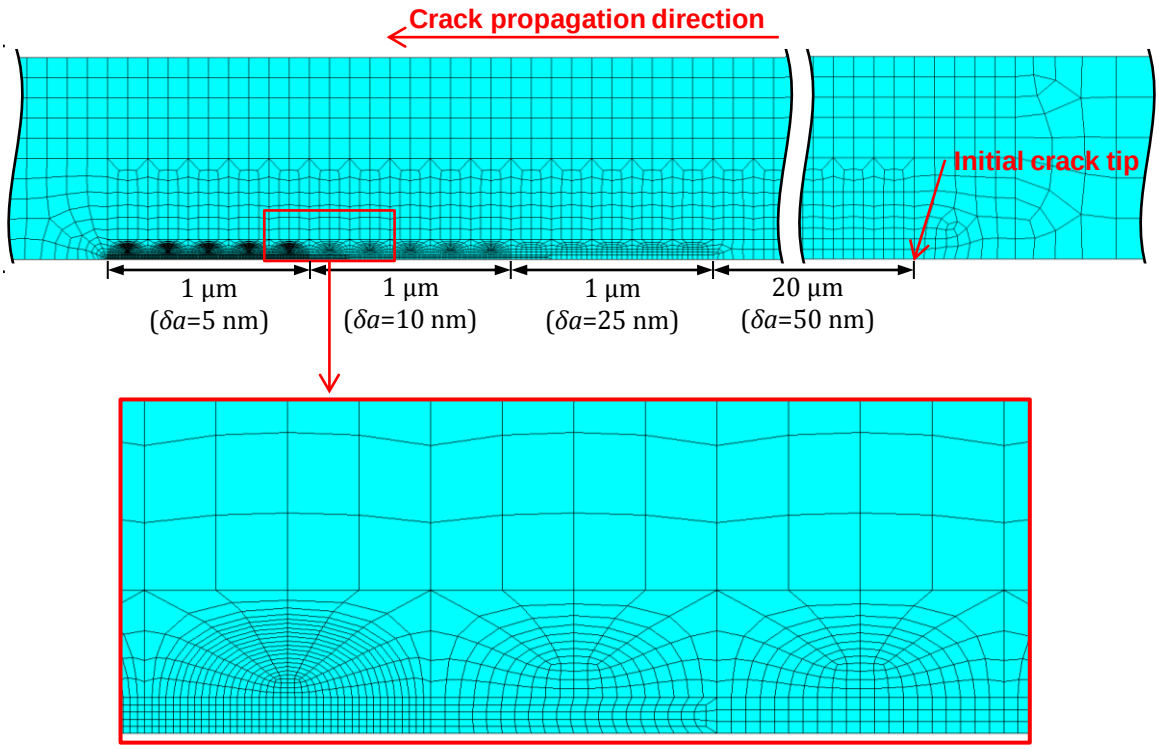

Figure 10.5. Finite element mesh of peeling film strip. Crack first propagates 20 μm through 50 nm size elements, then transitions into refined mesh for convergence analysis. Zoomed picture shows transition where mesh is refined from 10 to 5 nm elements at the interface.

10.4 Solution Procedure

The finite element model is used to simulate monotonic peeling of the film strip under a constant applied load. Starting with the initially flat and stress-free film, the load is first ramped to the desired amount, at which point the crack is then manually propagated over a long distance until the fracture parameters reach a steady-state value. The general solution procedure used in this work is as follows:

1. Ramp the vertical load P over several load steps and solve until reaching the designated value P_f.
2. While maintaining $P = P_f$, decouple the pair of nodes (if both film and substrate are modeled) or remove fixed displacement constraint on the node (if film alone is modeled) at the crack tip, and solve.
3. Evaluate G and Γ at the current crack tip using VCCT and energy based methods.

4. Repeat steps 2-3 until the ERR and FER fracture parameters reach steady-state values G_{ss} and Γ_{ss}, respectively.

10.5 Results

The typical plastic strain distribution in the film strip is shown near the advancing crack tip in Figure 10.6. During the load ramp, the elements around the initial crack tip become highly distorted, and as a result a relatively large and intense plastically strained region develops due to the stress concentration and the local bending of the adherend. However, as the crack propagates away from its starting position under constant load, the intensity of the plastic region lessens around the growing crack tip until finally reaching a steady state condition after several microns of crack growth. A consistent residual plastic wake remains along the debonded interface.

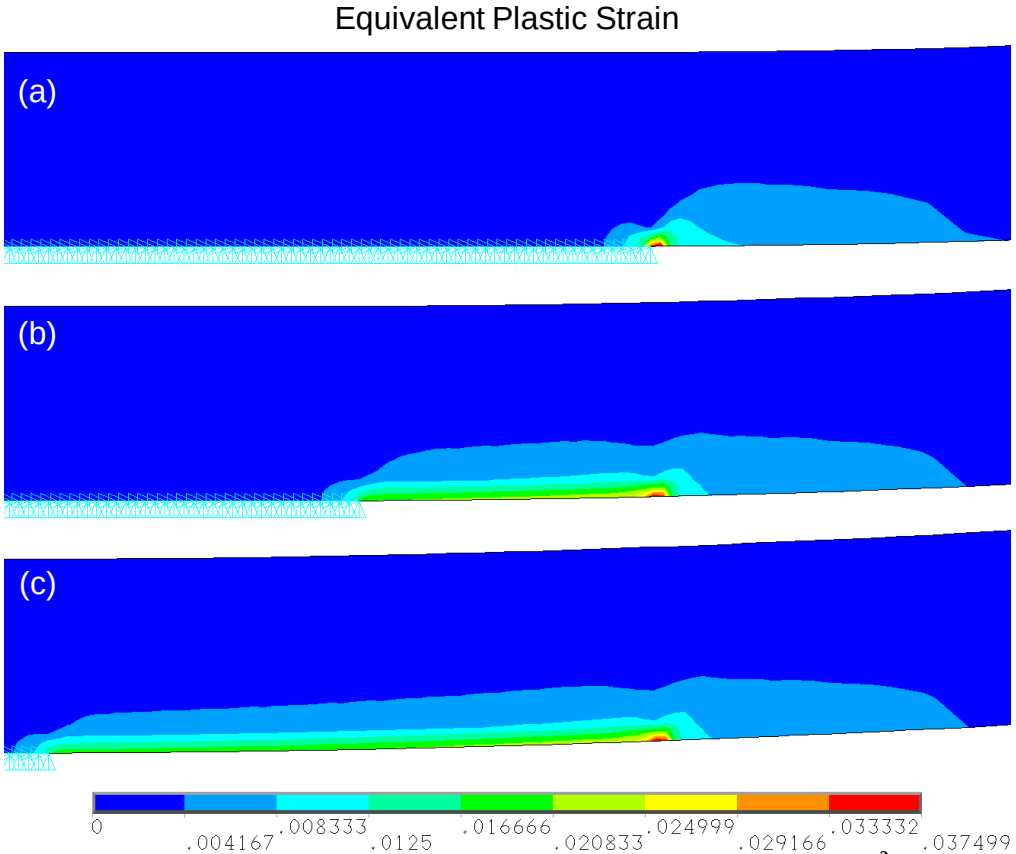

Figure 10.6. Residual plastic wake left behind advancing crack for P/bh = 50 J/m^2. Large residual strain region develops around the initial crack tip during the load ramp (a), which persists as the crack propagates 1 μm to (b) and 2 μm to (c).

The stress fields in the film near the crack tip are shown in Figure 10.7 after the delamination has propagated for over 20 μm. The highest stresses occur at the crack tip as expected from the stress concentration, where the tangential stress is about twice that of the normal and shear stress, respectively. These results suggest a strong Mode-II component of the fracture process. However, an exact measure of the mode mix is not well defined when the plastic zone is on the order of the film thickness.

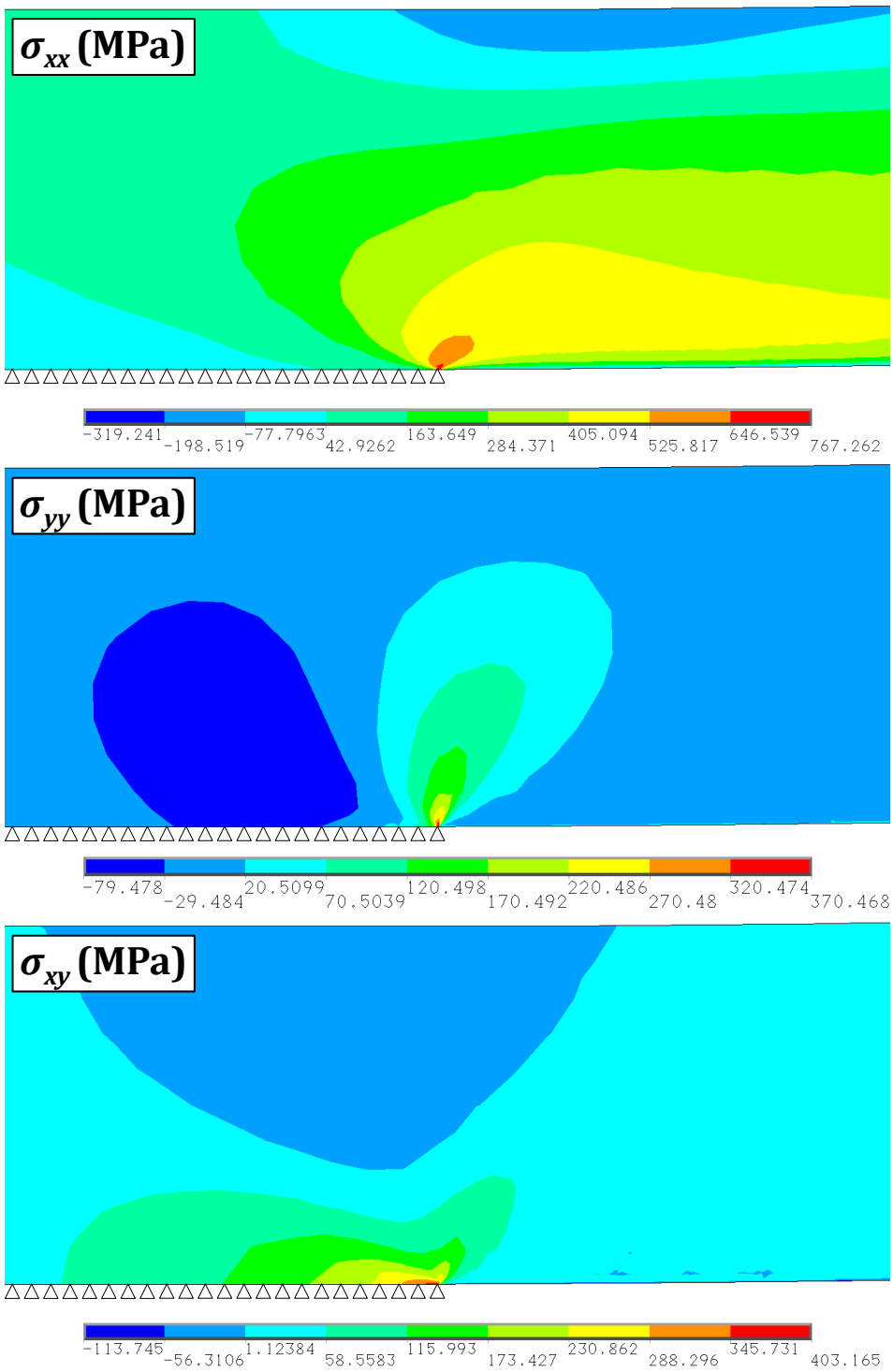

Figure 10.7. (a) Tangential, (b) normal, and (c) shear stress fields around crack tip relative to the interface after ~20 μm of delamination propagation for P/bh = 50 J/m^2.

The change in external work, elastic strain energy, and plastic work per increment of crack growth is shown in Figure 10.8 for P/bh = 50 J/m^2, with similar trends observed

for peeling under P/bh = 20-80 J/m^2. As soon as the crack begins to grow, the external work and plastic dissipation rates both rapidly drop whereas the elastic strain energy rate slowly increases, until all three energy terms reach a steady-state condition after about 15 μm of delamination propagation.

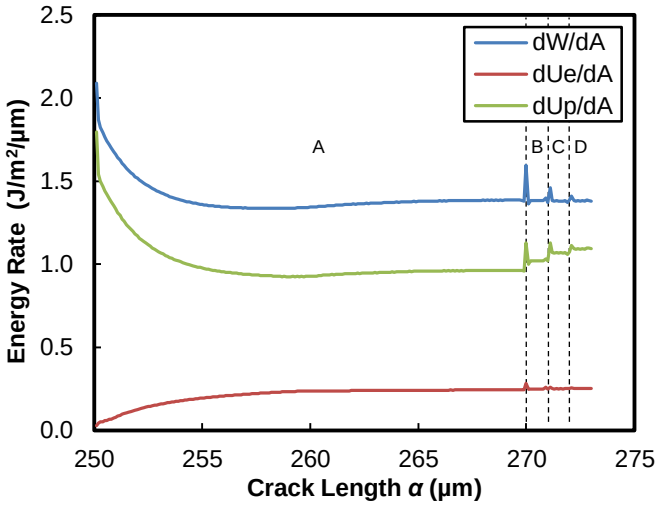

Figure 10.8. External work, elastic strain, and plastic strain energy rates as crack propagates from initial position at P/bh = 50 J/m^2 for 1 μm thick film. Crack growth through regions A, B, C, D correspond to element size (δa) = 50, 25, 10, 5 nm, respectively.

After 20 μm of growth, the crack is then propagated through a series of progressively refined mesh densities in order to assess the effect of element size on the calculated fracture parameters. Brief spikes in the energy rates can be seen as the crack grows through the abrupt transition regions from course to fine mesh density, but these do not affect the following trends and are thus disregarded. The external work and elastic strain energy rates are shown to be insensitive to the element size reduction from 50 to 5 nm, and thus G_{ss} has achieved mesh convergence as shown in Figure 10.9.

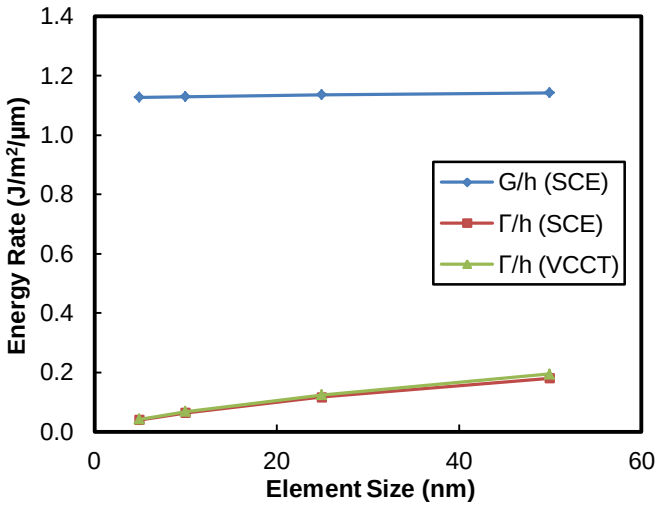

Figure 10.9. Dependence of steady-state fracture parameters on the mesh density along debonding interface using both VCCT and energy based methods for *P*/*bh* = 50 J/m^2.

The resulting G_{ss} is shown as a function of *P*/*bh* in Figure 10.10 and shows good agreement with the analytical model developed in Chapter 5 for the range of applied loads reported in the MAPT experiments. The finite element model incorporates local deformation effects, delamination propagation, and is clearly more sophisticated than the analytical model; however, the uniform tension assumption is shown to sufficiently capture the ERR of the MAPT test strips within the load range of interest. Thus, the analytical model can be used to calculate slightly conservative values of the critical ERR.

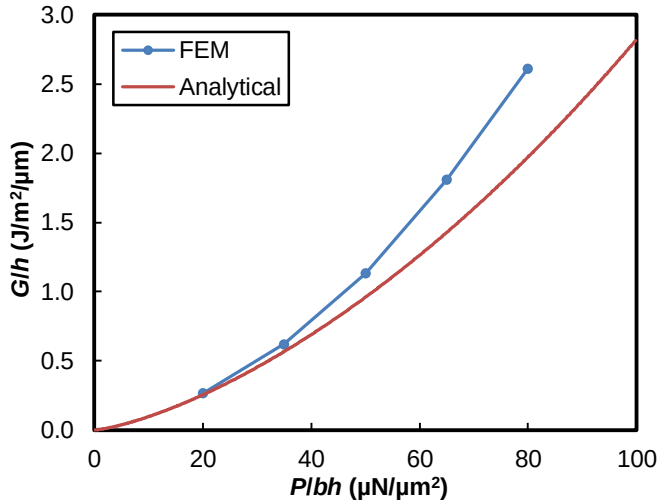

Figure 10.10. Steady-state ERR calculated using analytical peel model and finite element method.

The plastic dissipation rate, on the other hand, steadily increases for finer mesh densities and does not reach a converged value. Consequently, Γ_{ss} calculated from the energy rate terms is an order of magnitude lower than what is predicted by the analytical model and appears to approach zero as the mesh is continuously refined at the peeling interface as shown in Figure 10.9 and Figure 10.11. For comparison, the FER calculated via the VCCT method is also shown with very good agreement between these two numerical techniques over the entire range of crack propagation.

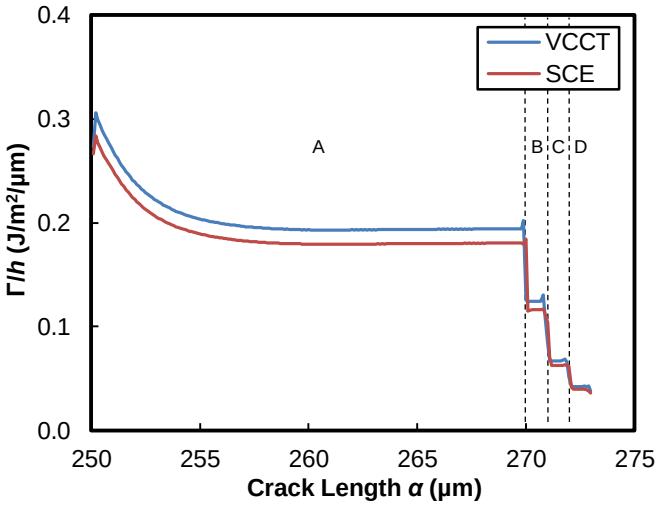

Figure 10.11. Fracture energy rate calculated for peeling film using the VCCT and SCE methods for P/bh = 50 J/m^2. Crack growth through regions A, B, C, D correspond to element size (δa) = 50, 25, 10, 5 nm, respectively.

10.6 Discussion

The SCE approach was pursued in this work in order to more closely simulate the dynamic peeling process for ductile films. In this model, every node along the debonding interface experiences the full brunt of the crack tip stress at some point in its history, and its results show a significant contrast with conventional one- or two-step numerical techniques. Significantly, the SCE simulation reveals that after the initial load ramp, the calculated fracture parameters decrease suddenly following delamination initiation, and do not stabilize until the delamination has propagated a distance that is an order of magnitude greater than the thickness of the film. This is the effect of the starting crack

tip, which becomes heavily distorted and accumulates an intense and widespread stress-strain field by the end of the load ramp. As the delamination grows, the advancing crack tip experiences less distortion and a more local stress field, while behind the crack tip the strip undergoes reverse bending as it becomes part of the stretched adherend. Therefore, the crack must propagate a relatively long distance before the additional bending at the crack tip and the reverse bending process behind the crack reach a steady-state condition. Once the delamination has progressed to steady-state, the ERR calculated from the finite element model matches the results of the analytical uniform tension model.

A consequence of modeling the film with conventional plasticity is that the FER continues to decrease for finer mesh density due to the increase in plastic deformation at the interface for smaller elements. The plastic strain profile through the thickness of the film just behind the advancing crack tip is shown in Figure 10.12 for varying mesh density. This indicates that mesh refinement only affects the strain in the portion of film within 50 nm of the peeling interface, with the most strained elements at the interface. It is questionable for the 6% equivalent plastic strain resulting from the refined finite element model to be observed in the actual case, as this is well beyond the fracture strain typically reported for Cu films [61, 94, 95]. Moreover, the apparently severe strain gradient may be unrealistically supported by a material based on dislocation theory [96]. Therefore, additional hardening of the Cu film based on strain gradient plasticity theory is discussed in Chapter 11, which addresses the excessive plastic dissipation resulting from modeling the film behavior based on classical plasticity theory.

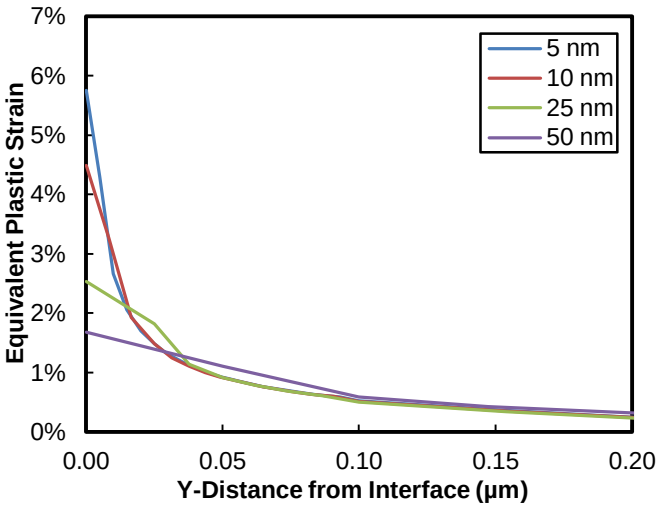

Figure 10.12. Equivalent plastic strain through the film thickness, 100 nm behind crack tip, for varying mesh density at the interface.

CHAPTER 11

STRAIN GRADIENT PLASTICITY EFFECTS

11.1 Background

For thin film delamination processes, there is a strong case that conventional plasticity theory can significantly underestimate the hardening and stresses near the crack tip due to the large local strain gradients, and thus overestimate the plastic dissipation energy [84, 97]. This observation stems from experiments in which scale effects are observed where a material locally hardens in regions of high strain gradient, such as thin wires in torsion [98] (see Figure 11.1), indentation of films [99] (see Figure 11.2), and bending of thin films [100].

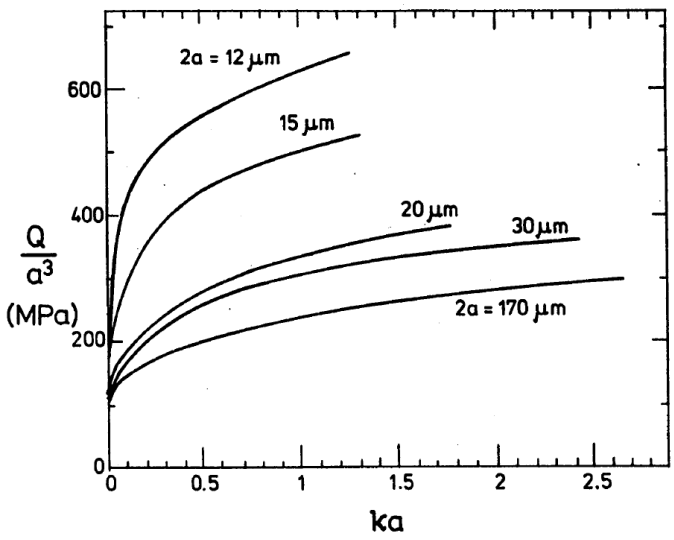

Figure 11.1. Torsional response of copper wires with diameter 2*a*, where *Q* is the torque and *κ* is the twist per unit length. Conventional plasticity predicts no dependence of the response on the wire diameter [98].

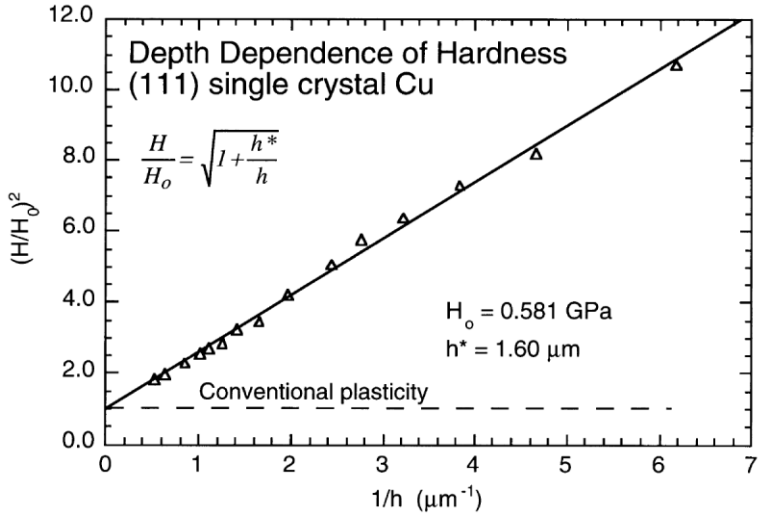

Figure 11.2. Indentation depth dependence of hardness of single crystal copper [99].

A theory of strain gradient plasticity based on dislocation mechanisms was thus proposed by Fleck et al. [98] following the work of others [101-103]. This concept is centered on the idea that homogeneous hardening results from the accumulation of statistically stored dislocations (SSDs) whereas strain gradients mandate the formation of additional geometrically necessary dislocations (GNDs). An internal material length scale parameter was thus introduced to reflect material's ability to accommodate the strain gradient [96], which can be expressed as a function of the shear modulus, the yield stress, and Burgers vector [99]. In practice, however, the material length scale is often used as a fitting parameter to match simulations with experiments, and its true physical interpretation is not yet well understood [104].

Many extensions of the dislocation-based strain gradient plasticity model have been advanced in the literature. Some of these works rely on higher order stresses which complicate the constitutive equations and require additional boundary conditions [96, 97]. However, alternative theories without incorporating higher order stress have been pursued which can work within the framework of conventional plasticity for easier implementation into standard finite element models [105, 106].

An overview of mechanism-based strain gradient plasticity (MSGP) is presented in the following sections, along with an implementation algorithm for finite element simulations. Preliminary results are obtained for the developed MAPT finite element model, and implications on the derived fracture parameters are discussed.

11.2 Mechanism-based Strain Gradient Plasticity

A dislocation model based on the Taylor relation was developed by Nix and Gao [99] which assumes a simple sum of dislocations, and links the shear flow stress τ and the dislocation density as

$$\tau = \alpha\mu b\sqrt{\rho_S + \rho_G}, \tag{11.1}$$

and the tensile flow stress σ is

$$\sigma = M\tau, \tag{11.2}$$

where α is an empirical coefficient of around 0.2-0.5, μ is the shear modulus, b is the Burgers vector, ρ_S is the density of SSDs, ρ_G is the density of GNDs, and M is the Taylor factor. Conventional uniaxial hardening is based on the statistically stored dislocations, whereas ρ_G is affected by the gradient in the strain field and is related to the effective plastic strain gradient η^{p} through

$$\rho_G = \bar{r}\frac{\eta^{\mathrm{p}}}{b}, \tag{11.3}$$

where $\bar{r}$ is the Nye-factor introduced as a measure of the dislocation inefficiency, and is estimated to have a value of about 2 for fcc metals such as copper [107, 108]. Following Gao et al. [109], Huang et al. [108] used the Taylor relation to state the flow stress as

$$\sigma = \sigma_{\mathrm{ref}}\sqrt{f^2(\varepsilon^{\mathrm{p}}) + l\eta^{\mathrm{p}}} \tag{11.4}$$

where σ_{ref} is a reference stress, $f(\varepsilon^p)$ is the material uniaxial hardening function such that $\sigma=\sigma_{ref} f(\varepsilon^p)$, and l is a characteristic material length scale parameter which incorporates the elastic, plastic, and atomic nature of the material. The length scale l derived for FCC metals approximates that derived by Fleck and Hutchinson [97] for general isotropic solids such that

$$l = 18\alpha^2 \left(\frac{\mu}{\sigma_{ref}}\right) b \approx 3\alpha^2 \left(\frac{\mu}{\sigma_y}\right) b, \tag{11.5}$$

where α is an empirical constant assumed to be unity and σ_y is the uniaxial yield stress, for the case when σ_{ref} ~$6\sigma_y$. The parameter l is generally on the order of one micron, and has been reported to have a value of 2.82 μm for polycrystalline copper [110].

A conventional power-law plasticity model can be used for the uniaxial flow stress such that

$$\sigma = K(\varepsilon^p)^n, \tag{11.6}$$

where K is a strain hardening modulus, ε^p is the equivalent plastic strain, and n is the hardening exponent. Incorporating the strain gradient effect, the modified flow stress can thus be expressed as

$$\sigma = K\sqrt{(\varepsilon^p)^{2n} + l\eta^p}. \tag{11.7}$$

The increase in the flow stress due to strain gradient effect has been defined as the flow stress ratio (FSR) [111], and results in

$$\text{FSR} = \frac{\sqrt{(\varepsilon^p)^{2n} + l\eta^p}}{(\varepsilon^p)^n}. \tag{11.8}$$

The strain hardening exponent is assumed to be independent of the strain gradient [109]. Therefore, Equation (11.7) can be expressed as

$$\sigma = K^*(\varepsilon^p)^n, \tag{11.9}$$

where

$$K^* = K \times \mathrm{FSR}. \tag{11.10}$$

Expressing the flow stress relation using Equation (11.9) is convenient since it has the same structure as conventional plasticity behavior typically utilized in finite element modeling. An algorithm for implementing this approach for capturing the strain gradient hardening was developed by Pucha et al. [111] and is presented in the following sections.

11.2.1 Calculation of strain gradients

The equations presented here are reproduced from detailed presentations published elsewhere [97, 109]. For simplicity, the effective total strain gradient, η', is calculated in this section. The effective plastic strain gradient, η^{p}, which is implemented into MSGP theory, can be similarly calculated from the plastic component of the strain tensor.

The strain gradient is defined as the second derivative of the displacement and first derivative of the strain through

$$\eta_{ijk} \equiv u_{k,ij} = \varepsilon_{ki,j} + \varepsilon_{kj,i} - \varepsilon_{ij,k}, \tag{11.11}$$

where η is a third-order tensor. It is assumed that only the deviatoric component of the strain gradient tensor contributes to the hardening, which can be calculated using

$$\eta'_{ijk} = \eta_{ijk} - \eta^{\mathrm{H}}_{ijk}, \tag{11.12}$$

where η^{H} is the hydrostatic strain gradient tensor,

$$\eta^{\mathrm{H}}_{ijk} = \frac{1}{4}\left(\delta_{ik}\eta_{jpp} + \delta_{jk}\eta_{ipp}\right), \tag{11.13}$$

and where δ is the Kronecker delta. The effective strain gradient is then computed as one-half the magnitude of the deviatoric strain gradient tensor,

$$\eta' = \sqrt{\frac{1}{4}\eta'_{ijk}\eta'_{ijk'}} \tag{11.14}$$

where the ¼ factor results from the appropriate scaling of the three quadratic invariants of the strain gradient tensor by considering the dislocation models for bending, torsion, and void growth.

11.3 Implementation of MSGP

An iterative algorithm was developed for implementing strain gradient hardening into the finite element model of thin film peeling following Pucha et al. [111]. The concept involves iteratively updating the constitutive behavior of each individual element with respect to the resulting local strain and strain gradient field. The load step is then repeated with the new element-specific material properties until convergence with respect to the defined hardening behavior and the resulting element distortion.

11.3.1 Calculation of Strain and Strain Gradient Field

The MSGP hardening behavior of the element is based on the scalar value of the effective strain and effective strain gradient evaluated at the element centroid. Pucha et al. [111] accomplishes this by fitting a bilinear strain surface to the nodal strains of a linear quadrilateral element. However, the potential disadvantage of using this approach is that the resulting surface may occasionally be saddle-shaped, where the value at the centroid is significantly different than at the defining nodes as shown in Figure 11.3. To remedy this issue, a quadratic term can be added to the surface fit, with the additional constraint that the centroid is assigned an average strain value amongst the four corner nodes. Additional details of the strain surface calculation can be found in Appendix A. The strain gradient tensor is then evaluated at the element centroid by taking the appropriate derivatives of the strain surface, and the effective strain gradient is computed as in Equation (11.14).

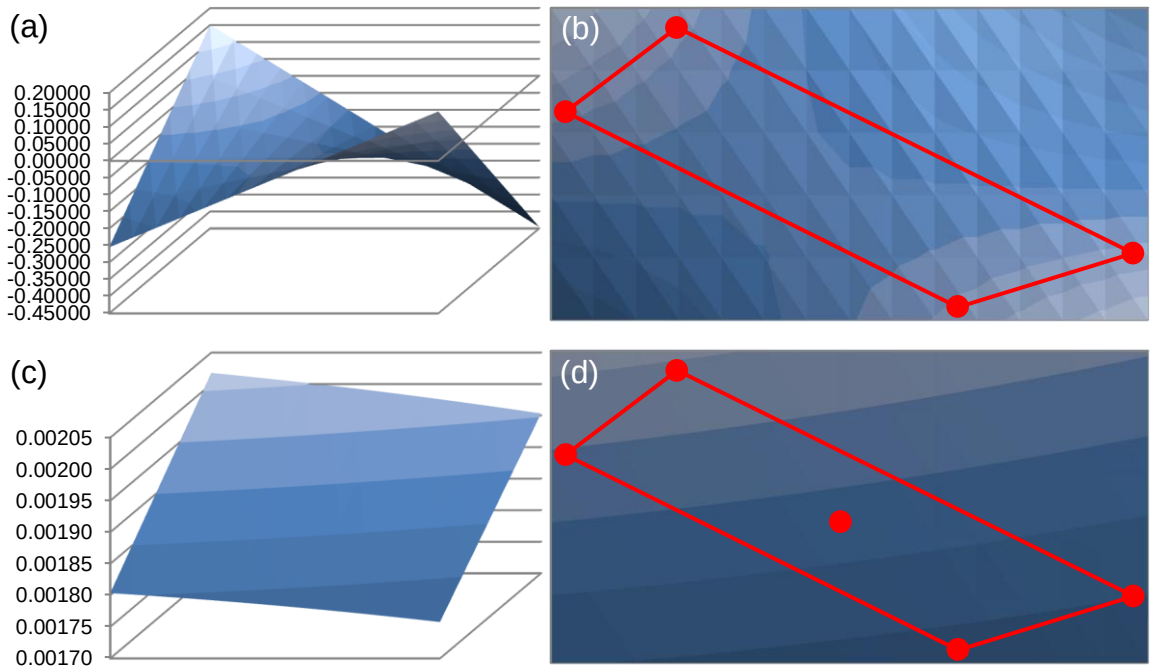

Figure 11.3. Isometric (a,c) and top-down (b,d) view of example strain surfaces computed from element with nodal strains ε_{xx} = 0.0018-0.0020. The element boundary is overlaid in the top-down view, with red dots representing points with defined strain for surface fit calculations. (a,b) Bilinear surface has saddle-shape where the strain at the centroid is ~2 orders of magnitude larger than at the nodes. (c,d) Quadratic surface with assigned nodal strain average at centroid produces flat strain distribution.

11.3.2 Algorithm for Strain Gradient Effect

An algorithm for implementing MSGP effects is detailed as follows, which utilizes conventional finite elements with no additional functionality beyond standard structural behavior:

1. Assign all elements within the peeling film the same nonlinear material property such that $\varepsilon = \sigma/E + (\sigma/K_0)^{1/n}$, where K_0 is the initial hardening modulus in the absence of strain gradients.

2. Apply boundary conditions and solve.

3. For each individual element, calculate the effective plastic strain and strain gradient

    i. Assign nodes in counterclockwise (CCW) order for

ii. Get displaced location of nodes

iii. Evaluate displaced location of centroid

iv. Get nodal plastic strain components: $\varepsilon_{xx}, \varepsilon_{yy}, \varepsilon_{xy}$

v. Assign average of nodal strains to centroid

vi. Evaluate equivalent plastic strain at centroid

vii. Fit strain surfaces across element from component nodal and centroid strains

viii. Evaluate effective plastic strain gradient at centroid

4. For each individual element, reassign the material property with the adjusted hardening modulus K^*.
   i. Evaluate FSR and new $K^* = K_{previous} \times \text{FSR}$
   ii. Reassign element material property with $K_{new} = K^*$
5. Repeat steps 2-4 until there is convergence with respect to the assigned hardening behavior and the resulting strain and strain gradient field (i.e. $K_{new} = K_{old}$)

11.3.3 Application of MSGP to Peel Model

This work represents an attempt to account for the effect of strain gradient hardening on thin film peeling. Due to some of the issues and technological challenges explained in the following sections, the MSGP algorithm was only executed for the case of the peel strip undergoing an applied load at the released end, and not for a delamination propagation process. However, various insights can be drawn from the preliminary results. These insights were then subsequently applied to the case of steady-state delamination, and suggest that the MSGP algorithm has the potential to incorporate strain hardening mechanisms during a crack growth process.

The algorithm for implementing MSGP must proceed for ~5 iterations for every load step until reaching convergence based on preliminary results and the results of Pucha et al [111]. Applied to the MAPT finite element model, each iteration can take

several minutes as each element's material properties must be updated serially. However, the MAPT model undergoing SCE analysis already requires a few thousand load steps as the interfacial crack is manually propagated a distance of over 20 μm. Implementation of MSGP over the full range of simulated delamination would therefore potentially increase the computation time by several orders of magnitude, and is beyond the scope of this work.

Alternatively, the MSGP algorithm is executed only for the first load step (the initial applied load ramp) in order to demonstrate that the plastic deformation is in fact reduced by incorporating the strain gradient effects. First, 1/3 of the total load $P/bh = 50$ $\mu N/\mu m^2$ was applied at the end of the strip, where the film is modeled with conventional plasticity as discussed in Chapter 10. Then, the element specific material properties were modified based upon the strain and strain gradient result at the end of the load ramp. The load ramp simulation is then repeated using the newly calculated material properties, and the process is repeated for a total of ten iterations as specified in the MSGP procedure above.

In addition, the potential implication of strain gradient hardening on the plastic deformation during steady-state peeling can be determined by examining the plastic deformation around a fully formed crack tip. Hence, the strain and strain gradient fields were evaluated for a steady-state crack advancing through a highly refined mesh, where the resulting FSR field indicates the regions most affected by strain gradient hardening.

11.4 Results and Discussion

For the MAPT film strip model undergoing MSGP hardening during the initial load ramp, the resulting effective plastic strain and strain gradient fields are shown in Figure 11.4 and Figure 11.5. Iteration #1 represents the result from using conventional plasticity, whereas subsequent iterations incorporate the strain gradient effects. The overall shapes of the strain and strain gradient fields are maintained from one iteration to

the next; however, the intensities of the fields near the initial crack tip are significantly reduced.

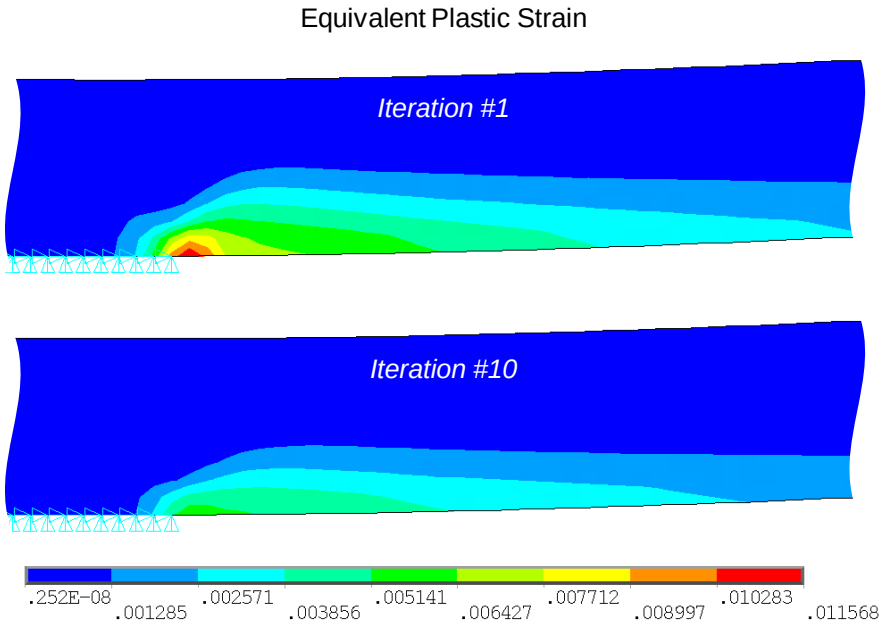

Figure 11.4. Equivalent plastic strain near initial crack tip after load ramp. Iteration #1 is result from conventional plasticity, whereas Iteration #10 is converged result of MSGP algorithm.

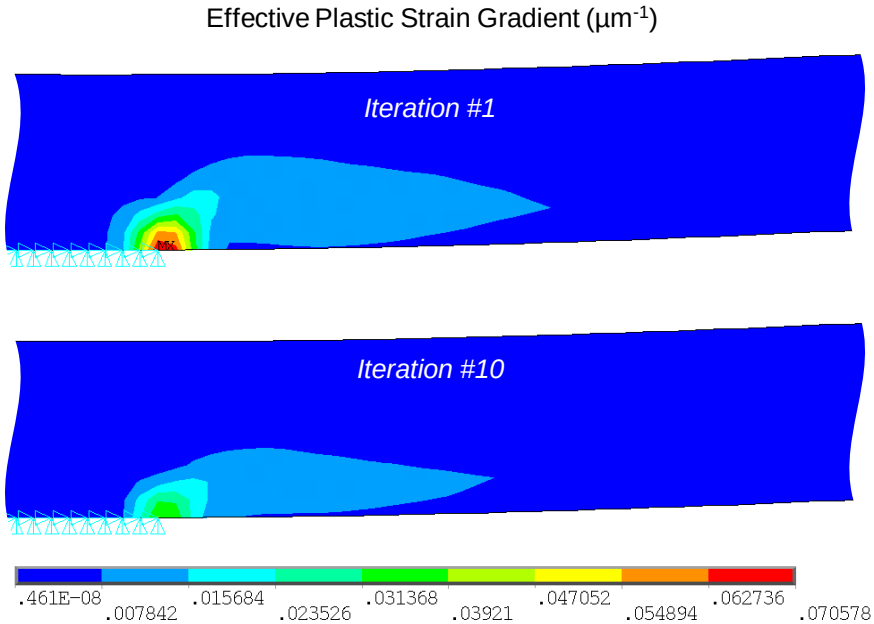

Figure 11.5.Effective plastic strain gradient near the initial crack tip after load ramp. Iteration #1 is result from conventional plasticity, whereas Iteration #10 is converged result of MSGP algorithm.

The maximum FSR, equivalent plastic strain, and effective plastic strain gradient is shown in Figure 11.6 for each iteration of the MSGP algorithm over the load ramp simulation. These values are shown normalized with respect to their initial result after iteration #1, respectively, in order to clearly show the trends. After just the second iteration, the resulting maximum plastic strain and strain gradient drop to almost half their initial value, and then remain fairly flat until converging around the fifth iteration. Conversely, the maximum FSR remains relatively unchanged after the first iteration.

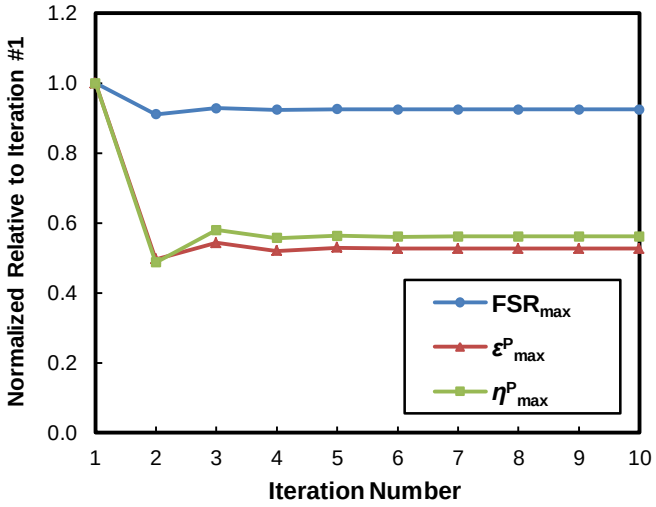

Figure 11.6. Convergence of maximum FSR, equivalent plastic strain, and effective strain gradient for one load step after ten iterations of MSGP.

These results suggest that although ~5 iterations of the MSGP algorithm are required to reach convergence, the most significant change is from the first to second iteration. Thus, the FSR field calculated after the first iteration (i.e. using conventional plasticity without strain gradient effects) is a good approximation of what the final converged FSR field would be after several iterations. Considering this observation, the FSR field was then calculated for the homogeneous film strip undergoing steady-state delamination as an indication of the required element specific hardening in order to satisfy the strain gradient constraints.

The following results pertain to further analysis of the MAPT peel model discussed in Chapter 10, where the crack has propagated a long distance and is in the

steady-state condition. Although the film is modeled with conventional plasticity, calculation of the FSR field from this result is a good predictor of the additional hardening behavior that should be expected due to the strain gradient. Thus, the effective plastic strain and strain gradient fields around the fully developed crack tip are shown in Figure 11.7 and Figure 11.8. As observed in Figure 10.12, the strain and strain gradient is the most intense for elements along the debonded interface, and exponentially decay away from the interface through the thickness of the film. The plastic strain gradient has a uniform profile behind the crack tip with a maximum value of almost 3 μm^{-1} for a refined element size of 5 nm.

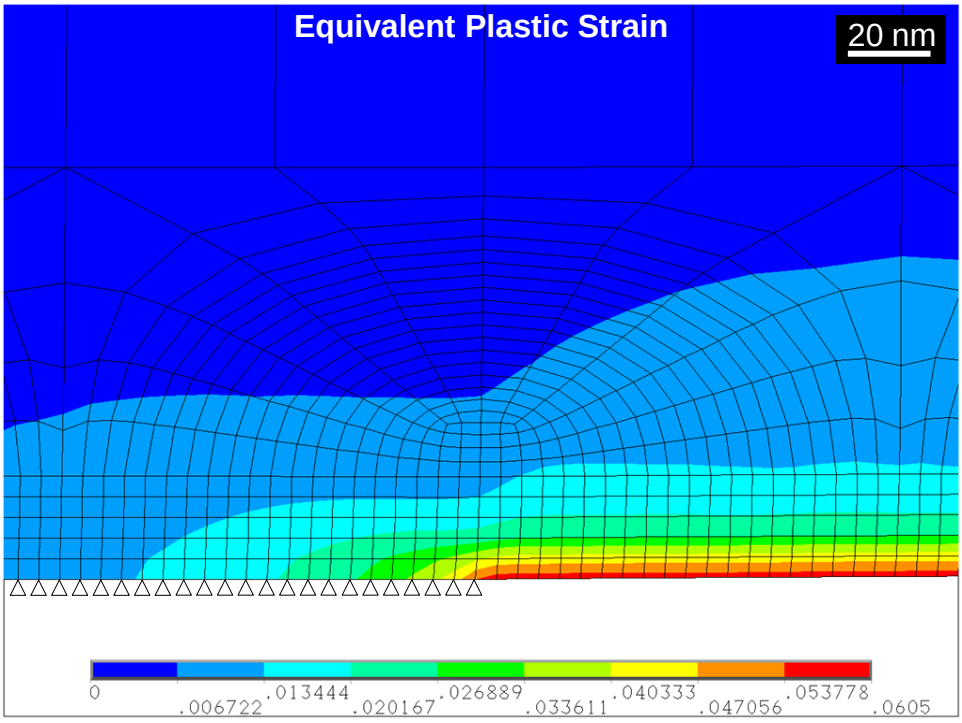

Figure 11.7. Equivalent plastic strain field near crack tip.

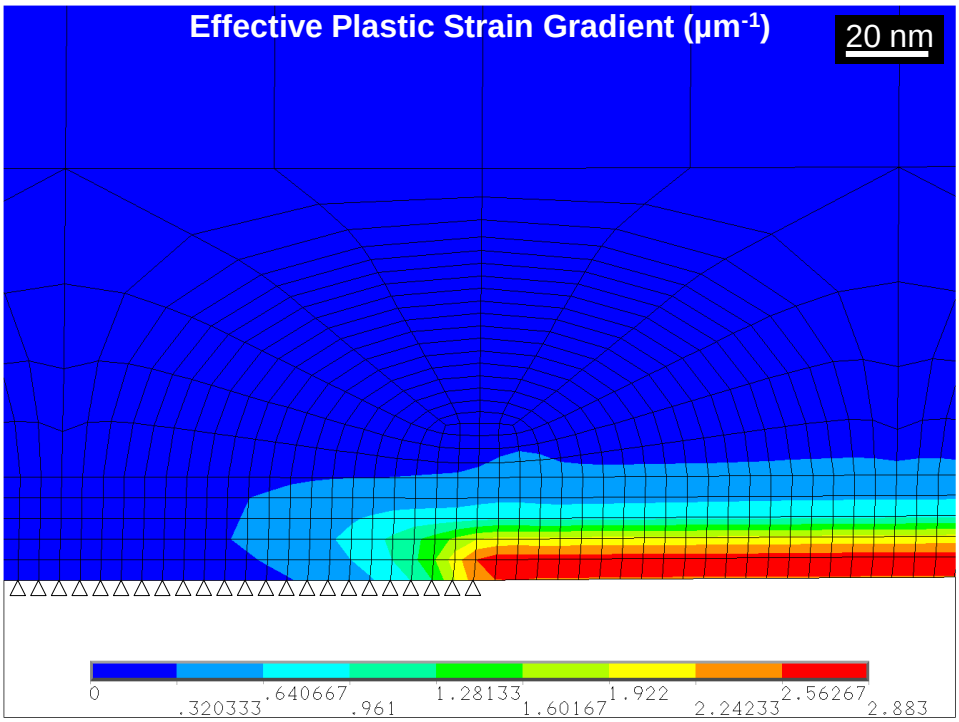

Figure 11.8. Effective plastic strain gradient field near crack tip.

The cumulative effect of the plasticity on the element hardening is shown in Figure 11.9, which results in the highest FSR (equal to about 6) for elements along the debonded interface as expected. The strongest FSR effect is concentrated within ~50 nm of the interface, and is greatly diminished through the remainder of the film thickness and ahead of the crack tip. This result correlates well with the previous observation that mesh refinement of the model under conventional plasticity causes escalating plastic strain within the elements nearest to the interface.

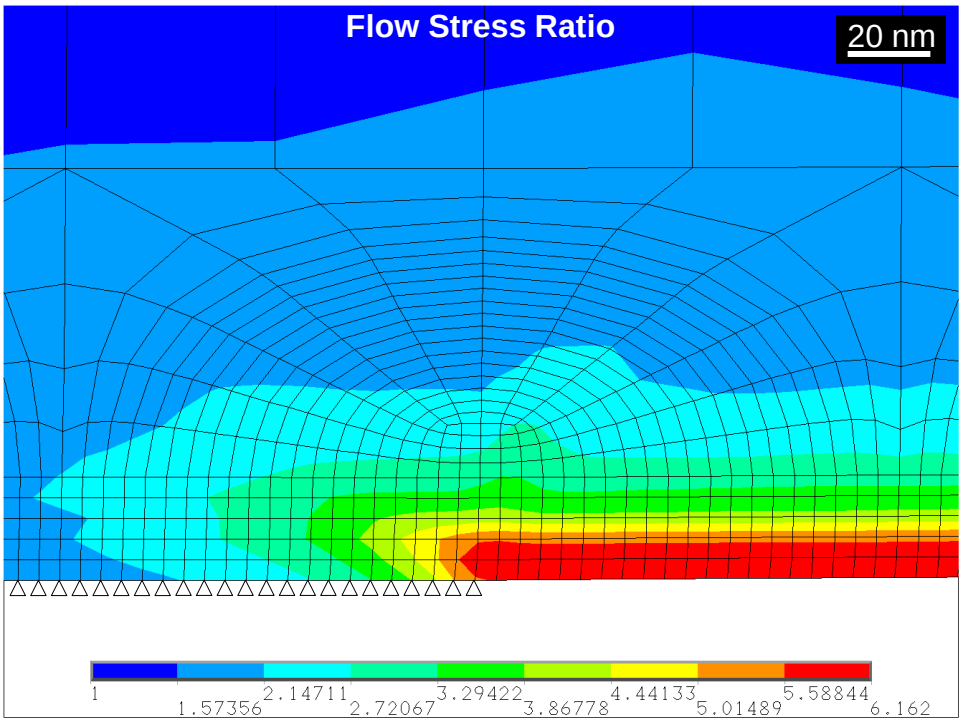

Figure 11.9. FSR field for elements near the crack tip after one iteration.

The final hardening behavior of each element is determined upon several iterations of implementing the MSGP algorithm. However, analysis of the strain and strain gradient field after only one iteration is a good indication of the degree of additional hardening that should be expected in the final converged result. Shown in Figure 11.10 are the resulting stress-strain responses for varying values of FSR, where FSR = 1 represents no additional hardening. The corresponding stress at a particular strain is nearly proportional to the FSR.

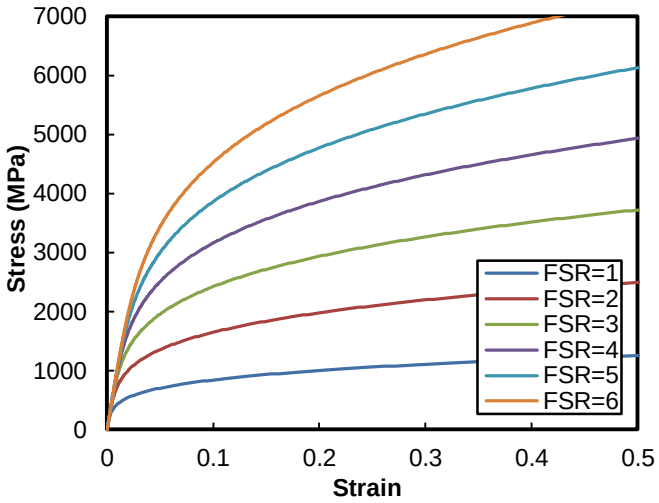

Figure 11.10. Effect of FSR on total stress-strain material response.

The dramatic increase in hardening for elements at the interface due to strain gradient effects should heavily restrict the amount of plastic strain that results in simulating the peeling process with conventional plasticity. Thus, full implementation of MSGP into the SCE analysis has the potential to resolve the problem of escalating plastic dissipation resulting from element refinement, and result in fracture parameters that are independent of mesh size at the cracked surface. Additionally, the overall plastic dissipation should be markedly reduced with MSGP, and result in an FER that more closely matches the ERR as predicted with the analytical model.

CHAPTER 12

CONTRIBUTIONS AND FUTURE WORK

12.1 Contributions

This work encompasses the whole range of matters involved with the development of a new material characterization technique, from the initial test concept to experimental execution and critical analysis. Some of the significant contributions of this work are highlighted below:

- Designed and developed a novel experimental test technique for the characterization of thin film interfaces under both monotonic and fatigue loading. Key features of this test include a fixtureless setup, utilization of magnetic forces for non-contact actuation, and the potential to conduct delamination experiments under various environmental conditions.
- Developed a batch fabrication and assembly process for micro-scale test specimens featuring electroplated Cu thin films on Si wafer substrates. Films and interfaces are representative of the as-deposited condition by using conventional cleanroom fabrication and surface-mount assembly techniques.
- Generated monotonic interfacial fracture data using the developed test technique.
- Generated cyclic fatigue interfacial fracture data. This work contains the first reported results of thin film fatigue delamination under constant stress-amplitude loading using a peel-type test configuration.
- Generated tensile test data using the developed test technique for characterization of the constitutive behavior of Cu thin films.

- Applied analytical models for the calculation of interface parameters under elastic-plastic peeling.
- Applied numerical finite element models for the calculation of interface parameters under elastic-plastic peeling. A new finite element approach was developed for simulating dynamic peeling under constant load by using a sequential nodal release technique.
- Implemented strain gradient plasticity theory into the finite element model in order to estimate the local film material hardening during peeling.

12.2 Future Work

There are multiple potential extensions of this work in the general areas of generating more experimental data, modifying the technique design for added functionality, and improving the analytical methods to extract the appropriate fracture parameters from the experimental results. The following is a list of some pertinent example projects:

Experimental Extensions

- Examine the effect of film thickness on the delamination behavior. The real challenge here is the ability to test nanoscale films, for which appropriate fabrication and assembly processes need to be developed.
- Relate the microstructural properties of the copper film to the interface parameters.
- Use the MAPT approach to characterize the interfaces of other material systems.

- Develop an environmental enclosure system for conducting interfacial characterization experiments where the MAPT specimen is subjected to varying temperature and humidity conditions.

Specimen Design

- Further simplify the MAPT fabrication process, perhaps through utilizing an inert sacrificial layer which requires minimal processing to pattern and remove.
- Develop a modified MAPT specimen for interfacial testing of multilayer stacks.
- Examine the effect of varying mode mixity by modifying the MAPT geometry to achieve higher peel angles. This can be accomplished by increasing the slack of the released film strips, perhaps through a polymer reflow process that results in a wavy sacrificial layer profile akin to that of uncoated PPC.
- Redesign the peel strips with variable width rather than constant width. An R-curve can possibly be determined for a strip with increasing width under monotonic loading.
- Further develop the thin film tensile test function using a modified MAPT specimen designed explicitly for material characterization.

Analysis

- Pursue more sophisticated analytical models of peeling which incorporate the bending and local plasticity effects of thin film peeling.
- Model the effects of residual stress and/or multilayered (nonhomogeneous) peeling films.
- Fully implement the iterative strain gradient hardening algorithm for the full range of elastic-plastic thin film peeling.

- Develop a cohesive zone formulation of the Cu/Si interface and compare with the results of the developed simulations.
- Development of a 3D finite element model of the MAPT peeling process.

APPENDIX A

12.3 Algorithm for calculation of strain and strain gradient

Finite element code was written in order to calculated the equivalent strains and strain gradients within any arbitrary linear quadrilateral element in an automated fashion.

12.3.1 Ordering of corner nodes

For calculation of the strain surface map, the corner nodes of the element must first be identified in counter-clockwise (CCW) order. This ordering method is based on the polar angle of direction from a reference node with respect to each of the element's other three nodes. As shown in Figure A.1, the bottom (or bottom-left) node is chosen as the reference node *q* so that all angles measured with respect to the local X′-axis are positive. The remaining nodes *r*, *s*, and *t* can then be identified by the ordering of polar angles ($\theta_{qr} < \theta_{qs} < \theta_{qt}$).

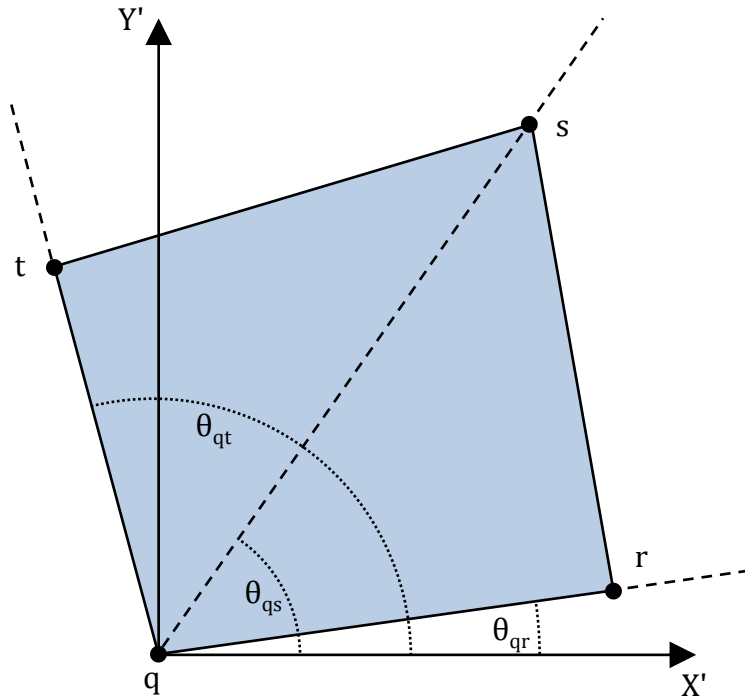

Figure A.1 Schematic for ordering corner nodes CCW.

12.3.2 Element strain distribution

A quadratic surface is fit to the nodal strains to determine the strain distribution for the linear quadrilateral element shown in Figure A.2. From the FEA solution, the displacement (u, v) and component strains (ε_x, ε_y, ε_{xy}) are first determined for each node. The strain distribution within the element is then calculated by fitting a surface for each of the component nodal strains. First, the coordinate position of each displaced node m is determined using

$$x^m = x_0^m + u^m \tag{A.1}$$

$$y^m = y_0^m + v^m \tag{A.2}$$

where $m = q, r, s, t$, respectively, and (x_o, y_o) is the initial coordinate location. Then the location of the centroid (x^c, y^c) is determined from the displaced location of the nodes. The centroid is then assigned an average of the nodal strains such that

$$\varepsilon_{ij}^c = \frac{1}{4}\sum \varepsilon_{ij}^m, \tag{A.3}$$

where $m = q, r, s, t$.

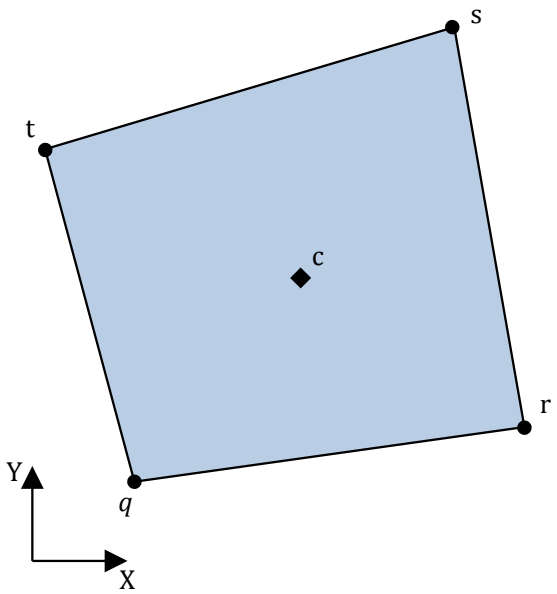

Figure A.2. Linear quadrilateral with nodes *q*, *r*, *s*, *t* and centroid *c*.

A quadratic strain surface fit can then be expressed as

$$\begin{bmatrix} \varepsilon_{xx} \\ \varepsilon_{yy} \\ \varepsilon_{xy} \end{bmatrix}^m = \begin{bmatrix} A_1 & A_2 & A_3 & A_4 & A_5 \\ B_1 & B_2 & B_3 & B_4 & B_5 \\ C_1 & C_2 & C_3 & C_4 & C_5 \end{bmatrix} \begin{bmatrix} 1 \\ x \\ y \\ xy \\ (xy)^2 \end{bmatrix}^m \tag{A.4}$$

where A_i, B_i, and C_i are constants and $m = q, r, s, t, c$. The coefficients can be evaluated as

$$[A_i] = [M]^{-1}[\varepsilon_{xx}^m], \tag{A.5}$$

$$[B_i] = [M]^{-1}[\varepsilon_{yy}^m],$$

$$[C_i] = [M]^{-1}[\varepsilon_{xy}^m],$$

where $i = 1$ to 5, $m = q, r, s, t, c$, and

$$[M] = \begin{bmatrix} 1 & x^q & y^q & x^q y^q & (x^q y^q)^2 \\ 1 & x^r & y^r & x^r y^r & (x^r y^r)^2 \\ 1 & x^s & y^s & x^s y^s & (x^s y^s)^2 \\ 1 & x^t & y^t & x^t y^t & (x^t y^t)^2 \\ 1 & x^c & y^c & x^c y^c & (x^c y^c)^2 \end{bmatrix}. \quad \text{(A.6)}$$

Once solving for the component strain surfaces, the strain gradient tensor is then computed by evaluating the appropriate derivative $\varepsilon_{ij,k}$ at the element centroid (x^c, y^c).

It should also be noted that there are multiple strain values at a node for each attached element. Therefore, the nodal strains used in the calculations are obtained by averaging the strain amongst all the elements which share the node as shown in Figure A.3.

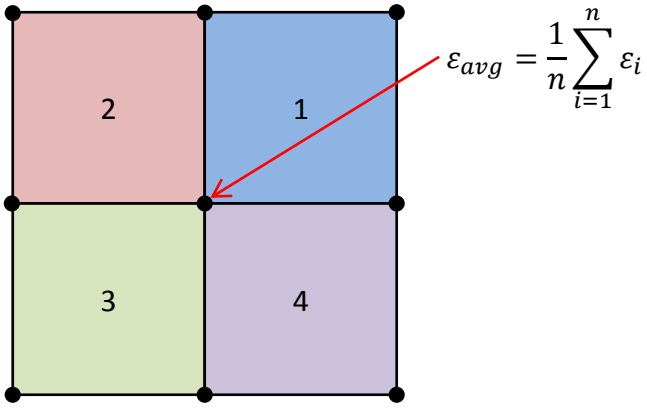

Figure A.3. The average nodal strain is an average of the individual strain values for all *n* elements which share the node.

12.3.3 Location of element centroid

The effective strain and strain gradient are evaluated at the element centroid. The location of the centroid (x^c, y^c) is calculated from the displaced locations of the nodes (x^m, y^m) with the following geometric relations

$$x^c = \frac{1}{6A}\sum_{m=1}^{4}(x^m + x^{m+1})(x^m y^{m+1} - x^{m+1} y^m), \quad \text{(A.7)}$$

$$y^c = \frac{1}{6A}\sum_{m=1}^{4}(y^m + y^{m+1})(x^m y^{m+1} - x^{m+1}y^m), \tag{A.8}$$

where A is the polygon's signed area,

$$A = \frac{1}{2}\sum_{m=1}^{4}(x^m y^{m+1} - x^{m+1}y^m). \tag{A.9}$$

12.3.4 Equivalent plastic strain at centroid

The von Mises equation for effective strain is

$$\varepsilon_{eq} = \frac{1}{\sqrt{2}(1+\nu')}\left[(\varepsilon_x - \varepsilon_y)^2 + (\varepsilon_y - \varepsilon_z)^2 + (\varepsilon_z - \varepsilon_x)^2 + \frac{3}{2}(\gamma_{xy}^2 + \gamma_{yz}^2 + \gamma_{xz}^2)\right]^{1/2}, \tag{A.10}$$

where ν' is the effective Poisson's ratio. Under plane-strain and plastic ($\nu' = 0.5$) conditions, Equation A.10 reduces to

$$\varepsilon_{eq} = \frac{2}{3}\sqrt{\varepsilon_x^2 - \varepsilon_y^2 + \varepsilon_x\varepsilon_y + \frac{3}{4}\gamma_{xy}^2}. \tag{A.11}$$

Equation A.11 can also be used to calculate the equivalent plastic strain as long as the plastic strain components are used.

REFERENES

[1] A. A. Griffith, "The phenomena of rupture and flow in solids," *Philosophical Transactions of the Royal Society of London. Series A, Containing Papers of a Mathematical or Physical Character,* vol. 221, pp. 163-198, 1920.

[2] G. R. Irwin, "Onset of fast fracture propagation in high strength steel and aluminum alloys," in *Sagamore Research Conference Proceedings,* 1956, pp. 289-305.

[3] T. L. Anderson, *Fracture Mechanics Fundamentals and Applications,* 3 ed. Boca Raton, FL: CRC Press, 2005.

[4] S. D. Antolovich and B. F. Antolovich, "An introduction to fracture mechanics," in *ASM Handbook: Fatigue and Fracture* vol. 19, ed: ASM Handbook Committee, 1996, pp. 371-380.

[5] G. R. Irwin, "Analysis of stresses and strains near the end of a crack traversing a plate," *Journal of Applied Mechanics,* vol. 24, pp. 361-364, 1957.

[6] J. Dundurs and D. B. Bogy, "Edge-bonded dissimilar orthogonal elastic wedges under normal and shear loading," *Journal of Applied Mechanics,* vol. 36, pp. 650-&, 1969.

[7] M. L. Williams, "The stresses around a fault or crack in dissimilar media," *Bulletin of the Seismological Society of America,* vol. 49, pp. 199-204, April 1959.

[8] F. Erdogan, "Stress distribution in a nonhomogeneous elastic plane with cracks," *Journal of Applied Mechanics,* vol. 30, pp. 232-236, 1963.

[9] A. H. England, "A crack between dissimilar media," *Journal of Applied Mechanics,* vol. 32, pp. 400-402, 1965.

[10] J. R. Rice and G. C. Sih, "Plane problems of cracks in dissimilar media," *Journal of Applied Mechanics,* vol. 32, pp. 418-&, 1965.

[11] M. Comninou and J. D. Achenbach, "Asymptotic fields at the transition zone of a propagating interface crack," *Mechanics Research Communications,* vol. 5, pp. 285-290, 1978.

[12] M. Comninou, "The interface crack," *Journal of Applied Mechanics-Transactions of the ASME,* vol. 44, pp. 631-636, 1977.

[13] M. Comninou, "Interface crack with friction in contact zone," *Journal of Applied Mechanics-Transactions of the ASME,* vol. 44, pp. 780-781, 1977.

[14] F. Erdogan, "Stress distribution in bonded dissimilar materials with cracks," *Journal of Applied Mechanics,* vol. 32, pp. 403-410, 1965.

[15] J. R. Rice, "Elastic fracture mechanics concepts for interfacial cracks," *Journal of Applied Mechanics-Transactions of the ASME,* vol. 55, pp. 98-103, Mar 1988.

[16] J. R. Rice, D. E. Hawk, and R. J. Asaro, "Crack tip fields in ductile crystals," *International Journal of Fracture,* vol. 42, pp. 301-321, Apr 1990.

[17] C. F. Shih, "Cracks on bimaterial interfaces: elasticity and plasticity aspects," *Materials Science and Engineering a-Structural Materials Properties Microstructure and Processing,* vol. 143, pp. 77-90, Sep 15 1991.

[18] B. M. Malyshev and R. L. Salganik, "The strength of adhesive joints using the theory of cracks," *International Journal of Fracture,* vol. 26, pp. 261-275, 1984.

[19] M. Charalambides, A. J. Kinloch, Y. Wang, and J. G. Williams, "On the analysis of mixed-mode failure," *International Journal of Fracture,* vol. 54, pp. 269-291, Apr 1 1992.
[20] J. W. Hutchinson and Z. Suo, "Mixed mode cracking in layered materials," *Advances in Applied Mechanics,* vol. 29, pp. 63-191, 1992.
[21] M. A. Sutton, X. M. Deng, F. S. Ma, J. C. Newman, and M. James, "Development and application of a crack tip opening displacement-based mixed mode fracture criterion," *International Journal of Solids and Structures,* vol. 37, pp. 3591-3618, Jun 2000.
[22] Y. G. Wei, "Modeling nonlinear peeling of ductile thin films - Critical assessment of analytical bending models using FE simulations," *International Journal of Solids and Structures,* vol. 41, pp. 5087-5104, Sep 2004.
[23] J. M. Krafft, A. M. Sullivan, and R. W. Boyle, "Effect of dimensions on fast fracture instability of notched sheets," in *Proceedings of the Crack Propagation Symposium*, Cranfield College of Aeronautics, 1961, pp. 8-28.
[24] J. R. Rice, "A path independent integral and approximate analysis of strain concentration by notches and cracks," *Journal of Applied Mechanics,* vol. 35, pp. 379-&, 1968.
[25] F. Erdogan, "Fracture mechanics," *International Journal of Solids and Structures,* vol. 37, pp. 171-183, Jan 2000.
[26] D. S. Dugdale, "Yielding of steel sheets containing slits," *Journal of the Mechanics and Physics of Solids,* vol. 8, pp. 100-104, 1960.
[27] G. I. Barenblatt, "The mathematical theory of equilibrium cracks in brittle fracture," *Advances in Applied Mechanics,* vol. Volume 7, pp. 55-129, 1962.
[28] R. M. Cannon, B. J. Dalgleish, R. H. Dauskardt, T. S. Oh, and R. O. Ritchie, "Cyclic fatigue-crack propagation along ceramic/metal interfaces," *Acta Metallurgica et Materialia,* vol. 39, p. 2145, 1991.
[29] P. C. Paris, M. P. Gomex, and W. E. Anderson, "A rational analytic theory of fatigue," *The Trend in Engineering,* vol. 13, pp. 9-14, 1961.
[30] P. G. Charalambides, J. Lund, A. G. Evans, and R. M. McMeeking, "A test specimen for determining the fracture resistarim of bimaterial interfaces," *Journal of Applied Mechanics-Transactions of the ASME,* vol. 56, pp. 77-82, Mar 1989.
[31] R. Dauskardt, M. Lane, Q. Ma, and N. Krishna, "Adhesion and debonding of multi-layer thin film structures," *Engineering Fracture Mechanics,* vol. 61, pp. 141-162, Aug 1998.
[32] Q. Ma, "A four-point bending technique for studying subcritical crack growth in thin films and at interfaces," *Journal of Materials Research,* vol. 12, pp. 840-845, Mar 1997.
[33] D. B. Marshall and A. G. Evans, "Measurement of adherence of residually stressed thin films by indentation. I. Mechanics of interface delamination," *Journal of Applied Physics,* vol. 56, pp. 2632-2638, 1984.
[34] A. A. Volinsky, N. R. Moody, and W. W. Gerberich, "Interfacial toughness measurements for thin films on substrates," *Acta Materialia,* vol. 50, pp. 441-466, Feb 8 2002.

[35] M. D. Kriese, N. R. Moody, and W. W. Gerberich, "Quantitative measurement of the effect of annealing on the adhesion of thin copper films using superlayers," in *Materials Research Society Symposium Proceedings*, 1998, pp. 363-368.
[36] S. Venkataraman, D. L. Kohlstedt, and W. W. Gerberich, "Microscratch analysis of the work of adhesion for Pt thin films on NiO," *Journal of Materials Research*, vol. 7, pp. 1126-1132, May 1992.
[37] M. P. deBoer, M. Kriese, and W. W. Gerberich, "Investigation of a new fracture mechanics specimen for thin film adhesion measurement," *Journal of Materials Research*, vol. 12, pp. 2673-2685, Oct 1997.
[38] R. Jacobsson, "Measurement of the adhesion of thin films," *Thin Solid Films*, vol. 34, pp. 191-199, 1976.
[39] A. F. Jankowski, "Adhesion of physically vapor-deposited titanium coatings to beryllium substrates," *Thin Solid Films*, vol. 154, pp. 183-198, Nov 12 1987.
[40] D. S. Rickerby, "A review of the methods for the measurement of coating-substrate adhesion," *Surface and Coatings Technology*, vol. 36, pp. 541-557, 1988.
[41] K. Kendall, "Thin-film peeling-the elastic term," *Journal of Physics D-Applied Physics*, vol. 8, pp. 1449-1452, 1975.
[42] R. J. Farris and J. L. Goldfarb, "An experimental partitioning of the mechanical energy expended during peel testing," *Journal of Adhesion Science and Technology*, vol. 7, pp. 853-868, 1993.
[43] Y. H. Lai and D. A. Dillard, "Using the fracture efficiency to compare adhesion tests," *International Journal of Solids and Structures*, vol. 34, pp. 509-525, Feb 1997.
[44] A. N. Gent and S. Kaang, "Pull-off forces for adhesive tapes," *Journal of Applied Polymer Science*, vol. 32, pp. 4689-4700, Sep 1986.
[45] H. Dannenberg, "Measurement of adhesion by a blister method," *Journal of Polymer Science*, vol. 33, pp. 509-510, 1958.
[46] M. G. Allen and S. D. Senturia, "Microfabricated structures for the measurement of adhesion and mechanical properties of polymer films," *Abstracts of Papers of the American Chemical Society*, vol. 193, pp. 166-PMSE, Apr 5 1987.
[47] A. S. Argon, V. Gupta, H. S. Landis, and J. A. Cornie, "Intrinsic toughness of interfaces," *Materials Science and Engineering a-Structural Materials Properties Microstructure and Processing*, vol. 107, pp. 41-47, Jan 1989.
[48] D. A. Dillard and Y. Bao, "The peninsula blister test: a high and constant strain energy release rate fracture specimen for adhesives," *Journal of Adhesion*, vol. 33, pp. 253-271, 1991.
[49] A. Bagchi, G. E. Lucas, Z. Suo, and A. G. Evans, "A new procedure for measuring the decohesion energy for thin ductile films on substrates," *Journal of Materials Research*, vol. 9, pp. 1734-1741, Jul 1994.
[50] M. B. Modi and S. K. Sitaraman, "Interfacial fracture toughness measurement for thin film interfaces," *Engineering Fracture Mechanics*, vol. 71, pp. 1219-1234, Jun-Jul 2004.
[51] J. T. Zheng and S. K. Sitaraman, "Fixtureless superlayer-driven delamination test for nanoscale thin-film interfaces," *Thin Solid Films*, vol. 515, pp. 4709-4716, Apr 9 2007.

[52] Y. Su, H. Wang, and W. Chen, "Microactuator based on electroplated permanent magnets and flexible polydimethyl siloxane diaphragm," *Proceedings of the Institution of Mechanical Engineers Part C-Journal of Mechanical Engineering Science,* vol. 222, pp. 517-524, Mar 2008.
[53] J. S. Bintoro, P. J. Hesketh, and Y. H. Berthelot, "CMOS compatible bistable electromagnetic microvalve on a single wafer," in *Microelectronics Journal*, 2005, pp. 667-672.
[54] H. J. Cho and C. H. Ahn, "Microscale resin-bonded permanent magnets for magnetic micro-electro-mechanical systems applications," *Journal of Applied Physics,* vol. 93, pp. 8674-8676, May 2003.
[55] Y. W. Yi and C. Liu, "Magnetic actuation of hinged microstructures," *Journal of Microelectromechanical Systems,* vol. 8, pp. 10-17, Mar 1999.
[56] C. Liu, T. Tsao, G. B. Lee, J. T. S. Leu, Y. W. Yi, Y. C. Tai, *et al.*, "Out-of-plane magnetic actuators with electroplated permalloy for fluid dynamics control," *Sensors and Actuators a-Physical,* vol. 78, pp. 190-197, Dec 14 1999.
[57] J. T. Zheng, G. Ostrowicki, and S. K. Sitaraman, "Non-contact magnetic actuation test technique to characterize interfacial fatigue fracture of thin films," *IEEE 59th Electronic Components and Technology Conference,* vol. 1-4, pp. 1368-1373, 2009.
[58] D. Vokoun, M. Beleggia, L. Heller, and P. Sittner, "Magnetostatic interactions and forces between cylindrical permanent magnets," *Journal of Magnetism and Magnetic Materials,* vol. 321, pp. 3758-3763, Nov 2009.
[59] J. Horkans, D. J. Seagle, and I. C. H. Chang, "Electroplated magnetic media with vertical anisotropy," *Journal of the Electrochemical Society,* vol. 137, pp. 2056-2061, Jul 1990.
[60] J. G. Williams, "Energy release rates for the peeling of flexible membranes and the analysis of blister tests," *International Journal of Fracture,* vol. 87, pp. 265-288, 1997.
[61] C. A. O. Henning, F. W. Boswell, and J. M. Corbett, "Mechanical properties of vacuum-deposited metal films - I. Copper films," *Acta Metallurgica,* vol. 23, pp. 177-185, 1975.
[62] K. S. Kim and N. Aravas, "Elastoplastic analysis of the peel test," *International Journal of Solids and Structures,* vol. 24, pp. 417-435, 1988.
[63] K. S. Kim and J. Kim, "Elasto-plastic analysis of the peel test for thin-film adhesion," *Journal of Engineering Materials and Technology,* vol. 110, pp. 266-273, Jul 1988.
[64] Y. G. Wei and H. F. Zhao, "Peeling experiments of ductile thin films along ceramic substrates - Critical assessment of analytical models," *International Journal of Solids and Structures,* vol. 45, pp. 3779-3792, Jun 30 2008.
[65] M. S. Bakir, H. A. Reed, H. D. Thacker, C. S. Patel, P. A. Kohl, K. P. Martin, *et al.*, "Sea of leads (SoL) ultrahigh density wafer-level chip input/output interconnections for gigascale integration (GSI)," *IEEE Transactions on Electron Devices,* vol. 50, pp. 2039-2048, Oct 2003.
[66] T. J. Spencer, P. J. Joseph, T. H. Kim, M. Swaminathan, and P. A. Kohl, "Air-gap transmission lines on organic substrates for low-loss interconnects," *IEEE*

Transactions on Microwave Theory and Techniques, vol. 55, pp. 1919-1925, Sep 2007.

[67] P. J. Joseph, P. Monajemi, F. Ayazi, and P. A. Kohl, "Wafer-level packaging of micromechanical resonators," *IEEE Transactions on Advanced Packaging,* vol. 30, pp. 19-26, Feb 2007.

[68] J. P. Jayachandran, H. A. Reed, H. S. Zhen, L. F. Rhodes, C. L. Henderson, S. A. B. Allen, *et al.*, "Air-channel fabrication for microelectromechanical systems via sacrificial photosensitive polycarbonates," *Journal of Microelectromechanical Systems,* vol. 12, pp. 147-159, Apr 2003.

[69] P. J. Joseph, H. A. Kelleher, S. A. B. Allen, and P. A. Kohl, "Improved fabrication of micro air-channels by incorporation of a structural barrier," *Journal of Micromechanics and Microengineering,* vol. 15, pp. 35-42, Jan 2005.

[70] M. Schlesinger and M. Paunovic, *Modern Electroplating*, 5th ed. Hoboken: John Wiley and Sons, 2010.

[71] Y. P. Zhao, L. S. Wang, and T. X. Yu, "Mechanics of adhesion in MEMS - a review," *Journal of Adhesion Science and Technology,* vol. 17, pp. 519-546, 2003.

[72] A. A. Volinsky, N. I. Tymiak, M. D. Kriese, W. W. Gerberich, and J. W. Hutchinson, "Quantitative modeling and measurement of copper thin film adhesion," *Material Research Society Symposium,* vol. 539, pp. 277-290, 1999.

[73] A. Bagchi and A. G. Evans, "Measurements of the debond energy for thin metallization lines on dielectrics," *Thin Solid Films,* vol. 286, pp. 203-212, Sep 30 1996.

[74] M. C. Shaw, D. B. Marshall, B. J. Dalgleish, M. S. Dadkhah, M. Y. He, and A. G. Evans, "Fatigue crack growth and stress redistribution at interfaces," *Acta Metallurgica et Materialia,* vol. 42, p. 4091, 1994.

[75] J. M. McNaney, R. M. Cannon, and R. O. Ritchie, "Fracture and fatigue-crack growth along aluminum-alumina interfaces," *Acta Materialia,* vol. 44, p. 4713, 1996.

[76] J. J. Kruzic, R. A. Marks, M. Yoshiya, A. M. Glaeser, R. M. Cannon, and R. O. Ritchie, "Fracture and fatigue behavior at ambient and elevated temperatures of alumina bonded with copper/niobium/copper interlayers," *Journal of the American Ceramic Society,* vol. 85, pp. 2531-2541, Oct 2002.

[77] J. J. Kruzic, J. M. McNaney, R. M. Cannon, and R. O. Ritchie, "Effects of plastic constraint on the cyclic and static fatigue behavior of metal/ceramic layered structures," *Mechanics of Materials,* vol. 36, pp. 57-72, Jan-Feb 2004.

[78] M. Hasegawa and Y. Kagawa, "Decohesion behavior in copper-sapphire interface under mode I cyclic loading," *Materials Science and Engineering a-Structural Materials Properties Microstructure and Processing,* vol. 417, pp. 158-165, Feb 15 2006.

[79] H. Hirakata, M. Kitazawa, and T. Kitamura, "Fatigue crack growth along interface between metal and ceramics submicron-thick films in inert environment," *Acta Materialia,* vol. 54, pp. 89-97, Jan 2006.

[80] J. Guzek, H. Azimi, and S. Suresh, "Fatigue crack propagation along polymer-metal interfaces in microelectronic packages," *IEEE Transactions on*

Components, Packaging, and Manufacturing Technology Part A, vol. 20, p. 496, 1997.

[81] W. Xie and S. K. Sitaraman, "Investigation of interfacial delamination of a copper-epoxy interface under monotonic and cyclic loading: Experimental characterization," *IEEE Transactions on Advanced Packaging,* vol. 26, pp. 447-452, 2003.

[82] M. Dessureault and J. K. Spelt, "Observations of fatigue crack initiation and propagation in an epoxy adhesive," *International Journal of Adhesion and Adhesives,* vol. 17, p. 183, 1997.

[83] J. E. Ritter, W. Grayeski, and T. J. Lardner, "Cyclic fatigue - Crack growth along polymer/glass interfaces," *Polymer Engineering and Science,* vol. 36, pp. 2382-2388, Sep 1996.

[84] H. F. Zhao and Y. G. Wei, "Determination of interface properties between micron-thick metal film and ceramic substrate using peel test," *International Journal of Fracture,* vol. 144, pp. 103-112, Mar 2007.

[85] S. Sohn, "A new method based on application of cyclic strain to evaluate the durability of pressure sensitive adhesives," *Journal of Adhesion Science and Technology,* vol. 17, pp. 1039-1053, 2003.

[86] K. Liao and K. T. Wan, "Delamination behavior of film-substrate systems under cyclic loading," *Journal of Materials Science Letters,* vol. 19, pp. 57-59, Jan 2000.

[87] Y. Hwangbo and J. H. Song, "Fatigue life and plastic deformation behavior of electrodeposited copper thin films," *Materials Science and Engineering a-Structural Materials Properties Microstructure and Processing,* vol. 527, pp. 2222-2232, Apr 15 2010.

[88] J. H. Park, J. H. An, Y. J. Kim, Y. H. Huh, and H. J. Lee, "Tensile and high cycle fatigue test of copper thin film," *Materialwissenschaft Und Werkstofftechnik,* vol. 39, pp. 187-192, Feb 2008.

[89] S. Zhang, M. Sakane, T. Nagasawa, and K. Kobayashi, "Mechanical properties of copper thin films used in electronic devices," *Procedia Engineering,* vol. 10, pp. 1497-1502, 2011.

[90] D. Y. W. Yu and F. Spaepen, "The yield strength of thin copper films on Kapton," *Journal of Applied Physics,* vol. 95, pp. 2991-2997, Mar 2004.

[91] K. Vanstreels, S. H. Brongersma, Z. Tokei, L. Carbonell, W. De Ceuninck, J. D'Haen, *et al.*, "Increasing the mean grain size in copper films and features," *Journal of Materials Research,* vol. 23, pp. 642-662, Mar 2008.

[92] E. F. Rybicki and M. F. Kanninen, "A finite element calculation of stress intensity factors by a modified crack closure integral," *Engineering Fracture Mechanics,* vol. 9, pp. 931-938, 1977.

[93] B. Dattaguru, K. S. Venkatesha, T. S. Ramamurthy, and F. G. Buchholz, "Finite-element estimates of strain-energy release rate components at the tip of an interface crack under mode-I loading," *Engineering Fracture Mechanics,* vol. 49, pp. 451-463, Oct 1994.

[94] H. B. Huang and F. Spaepen, "Tensile testing of free-standing Cu, Ag and Al thin films and Ag/Cu multilayers," *Acta Materialia,* vol. 48, pp. 3261-3269, Jul 2000.

[95] D. T. Read, "Tension-tension fatigue of copper thin films," *International Journal of Fatigue,* vol. 20, pp. 203-209, Mar 1998.
[96] N. A. Fleck and J. W. Hutchinson, "A phenomenological theory for strain gradient effects in plasticity," *Journal of the Mechanics and Physics of Solids,* vol. 41, pp. 1825-1857, Dec 1993.
[97] N. A. Fleck and J. W. Hutchinson, "Strain gradient plasticity," *Advances in Applied Mechanics,* vol. 33, pp. 295-361, 1997.
[98] N. A. Fleck, G. M. Muller, M. F. Ashby, and J. W. Hutchinson, "Strain gradient plasticity: theory and experiment," *Acta Metallurgica Et Materialia,* vol. 42, pp. 475-487, Feb 1994.
[99] W. D. Nix and H. J. Gao, "Indentation size effects in crystalline materials: A law for strain gradient plasticity," *Journal of the Mechanics and Physics of Solids,* vol. 46, pp. 411-425, Mar 1998.
[100] J. S. Stolken and A. G. Evans, "A microbend test method for measuring the plasticity length scale," *Acta Materialia,* vol. 46, pp. 5109-5115, Sep 1998.
[101] J. F. Nye, "Some geometrical relations in dislocated crystals," *Acta Metallurgica,* vol. 1, pp. 153-162, 1953.
[102] A. H. Cottrell, *The Mechanical Properties of Matter*. New York: Wiley, 1964.
[103] M. F. Ashby, "The deformation of plastically non-homogeneous materials," *Philosophical Magazine,* vol. 21, p. 399, 1970.
[104] B. Backes, Y. Y. Huang, M. Goken, and K. Durst, "The correlation between the internal material length scale and the microstructure in nanoindentation experiments and simulations using the conventional mechanism-based strain gradient plasticity theory," *Journal of Materials Research,* vol. 24, pp. 1197-1207, Mar 2009.
[105] A. Acharya and J. L. Bassani, "Lattice incompatibility and a gradient theory of crystal plasticity," *Journal of the Mechanics and Physics of Solids,* vol. 48, pp. 1565-1595, Aug 2000.
[106] Y. Huang, S. Qu, K. C. Hwang, M. Li, and H. Gao, "A conventional theory of mechanism-based strain gradient plasticity," *International Journal of Plasticity,* vol. 20, pp. 753-782, 2004.
[107] A. Arsenlis and D. M. Parks, "Crystallographic aspects of geometrically-necessary and statistically-stored dislocation density," *Acta Materialia,* vol. 47, pp. 1597-1611, Mar 1999.
[108] Y. Huang, Z. Xue, H. Gao, W. D. Nix, and Z. C. Xia, "A study of microindentation hardness tests by mechanism-based strain gradient plasticity," *Journal of Materials Research,* vol. 15, pp. 1786-1796, Aug 2000.
[109] H. Gao, Y. Huang, W. D. Nix, and J. W. Hutchinson, "Mechanism-based strain gradient plasticity - I. Theory," *Journal of the Mechanics and Physics of Solids,* vol. 47, pp. 1239-1263, Jun 1999.
[110] S. H. Chen and T. C. Wang, "A new hardening law for strain gradient plasticity," *Acta Materialia,* vol. 48, pp. 3997-4005, Oct 24 2000.
[111] R. V. Pucha, G. Ramakrishna, S. Mahalingam, and S. K. Sitaraman, "Modeling spatial strain gradient effects in thermo-mechanical fatigue of copper microstructures," *International Journal of Fatigue,* vol. 26, pp. 947-957, Sep 2004.

VITA

GREGORY T. OSTROWICKI

OSTROWICKI was born in Lakewood, New Jersey. He attended public schools in Howell, New Jersey, and received a B.S. in Mechanical Engineering from Rutgers University, New Brunswick, New Jersey in 2005 before coming to Georgia Institute of Technology, Atlanta, to pursue both a masters and doctorate in Mechanical Engineering. In his time at Georgia Tech, he served for two years as Chair of the Mechanical Engineering Graduate Student Association (MEGA).